

HADRONIC SPECTRUM OF  $\tau^- \rightarrow \pi^-\pi^0\nu_\tau$  DECAYS

by

RAHMAT RAHMAT

A DISSERTATION

Presented to the Department of Physics  
and the Graduate School of the University of Oregon  
in partial fulfillment of the requirements  
for the degree of  
Doctor of Philosophy

September 2008

**University of Oregon Graduate School**

**Confirmation of Approval and Acceptance of Dissertation prepared by:**

Rahmat Rahmat

Title:

"Hadronic Spectrum of tau  $\rightarrow$  pi- pi0 nu\_tau Decays"

This dissertation has been accepted and approved in partial fulfillment of the requirements for the degree in the Department of Physics by:

James Brau, Chairperson, Physics

Eric Torrence, Member, Physics

Stephen Kevan, Member, Physics

Nilendra Deshpande, Member, Physics

James Isenberg, Outside Member, Mathematics

and Richard Linton, Vice President for Research and Graduate Studies/Dean of the Graduate School for the University of Oregon.

September 6, 2008

Original approval signatures are on file with the Graduate School and the University of Oregon Libraries.

## An Abstract of the Dissertation of

Rahmat Rahmat                                  for the degree of                                  Doctor of Philosophy  
in the Department of Physics                                  to be taken                                  September 2008

Title: HADRONIC SPECTRUM OF  $\tau^- \rightarrow \pi^-\pi^0\nu_\tau$  DECAYS

Approved: \_\_\_\_\_  
Dr. Eric Torrence, Advisor

We report on a study of the invariant mass spectrum of the hadronic system in  $\tau^- \rightarrow \pi^-\pi^0\nu_\tau$  decays. This study was performed using data obtained with the BABAR detector operating at the PEP-II  $e^+e^-$  collider. We present fits to phenomenological models in which resonance parameters associated with the  $\rho(770)$ ,  $\rho'(1450)$  and  $\rho''(1700)$  mesons are determined. We also discuss the implications of our data with regard to estimates of the hadronic contribution to the muon anomalous magnetic moment.

## CURRICULUM VITAE

NAME OF AUTHOR: Rahmat Rahmat

PLACE OF BIRTH: Jakarta, Indonesia

DATE OF BIRTH: September 18, 1974

### GRADUATE AND UNDERGRADUATE SCHOOLS ATTENDED:

University of Oregon, Eugene

University of Indonesia, Indonesia

### DEGREES

Doctor of Philosophy in Physics, 2008, University of Oregon, Eugene.

Master of Science in Physics, 2004, University of Oregon, Eugene.

Bachelor of Science in Physics, 1998, University of Indonesia, Jakarta.

### ACADEMIC INTERESTS

Tau decays

Muon g-2

Trigger and Data Acquisition

### PROFESSIONAL EXPERIENCE

Research Assistant, Department of Physics, University of Oregon, Eugene,  
2004-2008

Teaching Assistant, Department of Physics, University of Oregon, Eugene,  
2002-2004

### GRANTS, AWARDS AND HONORS

Ghent Fellowship, University of Oregon

## ACKNOWLEDGMENTS

Thanks to Prof. James Brau, who has accept me to join Oregon High Energy Physics and guided me to see the beauty of High Energy Physics.

Thanks to Prof. Eric Torrence, who has worked very hard to guide me in this thesis. He has written comments and suggestions which are longer than than this thesis itself. For more than 4 years, he has dedicated tremendous efforts in this thesis.

Thanks to Dr. Olga Igonkina and Dr. Minghui Lu, who has helped me a lot when I started this analysis.

Thanks to Prof. Stephen Kevan, who accepted me to be an Oregon Graduate student.

Thanks to Prof. Nilendra G. Deshpande, who has guided me to see the beauty of Quantum Mechanics. In addition, Prof. Nilendra G. Deshpande had sponsored me to win one of the prestigious fellowships in University of Oregon, Ghent Fellowship.

Thanks to Prof. James Isenberg for his advice and suggestions in this thesis.

I would like to thanks to Prof. David Strom, Prof. Ray Frey, Jan Strube, Jeff Kolb and Nick Blount for important discussions, advice and comments.

Very special thanks to my wife Yam Sau Kuen, who has sacrificed her study in Ph.D. Accounting at University of Oregon to come with me to SLAC, California. She has given the best support to me to finish this thesis. Thanks to my daughters, Jasmine Jong and Jane Jong, who have given me joy and happiness while working on this thesis.

## TABLE OF CONTENTS

Chapter	Page
I     INTRODUCTION . . . . .	1
1     Hadronic Tau Decay . . . . .	2
2     Spectral Function of $\tau^- \rightarrow \pi^-\pi^0\nu_\tau$ Decays . . . . .	3
3     Comparison to $e^+e^-$ Data . . . . .	4
4     Analysis Overview . . . . .	7
II    OVERVIEW OF MUON MAGNETIC ANOMALY . . . . .	10
III   PHENOMENOLOGICAL MODELS . . . . .	15
1     The Model of Kuhn and Santamaria . . . . .	16
2     The Model of Gounaris and Sakurai . . . . .	16
IV    THE BABAR EXPERIMENT . . . . .	18
1     The PEP-II Collider . . . . .	18
2     The BABAR Detector . . . . .	21
2.1   Silicon Vertex Tracker . . . . .	24
2.2   Drift Chamber . . . . .	24
2.3   Cherenkov Detector . . . . .	27
2.4   Magnet Coil . . . . .	29
2.5   Electromagnetic Calorimeter . . . . .	29
2.6   Instrumented Flux Return . . . . .	39
2.7   Trigger . . . . .	41
3     Offline Data Processing . . . . .	44
3.1   Prompt Data Reconstruction . . . . .	44
3.2   Data Skimming . . . . .	46

Chapter		Page
V	DATA AND MONTE CARLO(MC) . . . . .	48
1	Data . . . . .	48
2	Monte Carlo(MC) . . . . .	50
VI	EVENT PRESELECTION . . . . .	52
1	$\pi^0$ Candidate Preselection . . . . .	52
2	Charged Candidate Preselection . . . . .	53
VII	EVENT SELECTION . . . . .	59
1	Event Reconstruction . . . . .	59
2	Selection Process . . . . .	59
3	Final Event Sample . . . . .	67
VIII	UNFOLDING . . . . .	70
1	Singular Value Decomposition . . . . .	71
2	Unfolding Procedure . . . . .	72
IX	FITTING RESULTS . . . . .	77
1	Form Factor . . . . .	79
2	Integration Procedure . . . . .	81
X	UNCERTAINTIES . . . . .	82
1	Method . . . . .	82
2	Efficiency . . . . .	83
3	2.1 Tracking . . . . .	83
3	2.2 $\pi^0$ Efficiency . . . . .	83
3	2.3 $\pi^0$ Reconstruction . . . . .	86
3	Resolution . . . . .	94
3	3.1 Tracking Resolution . . . . .	94
3	3.2 Photon Resolution . . . . .	94
4	Backgrounds . . . . .	99
4	4.1 $q\bar{q}$ Background . . . . .	99
4	4.2 $\tau$ Background . . . . .	101
5	Other Systematic . . . . .	110

Chapter		Page
	5.1 Bin Size of $\pi^-\pi^0$ Invariant Mass . . . . .	110
	5.2 Unfolding . . . . .	110
	5.3 Stability Over Runs Period . . . . .	113
6	Comparison between GS and KS Fitting . . . . .	115
7	Statistical Uncertainty . . . . .	115
XI	CONCLUSION . . . . .	118
1	Theoretical Correction . . . . .	119
2	Summary . . . . .	121
3	Comparison with Other Experiments . . . . .	122
3.1	$M_\rho$ . . . . .	122
3.2	$\Gamma_\rho$ . . . . .	122
3.3	$M_{\rho'}$ . . . . .	122
3.4	$\Gamma_{\rho'}$ . . . . .	123
3.5	$M_{\rho''}$ . . . . .	123
3.6	$\Gamma_{\rho''}$ . . . . .	123
3.7	$\beta$ . . . . .	124
3.8	$\phi_\beta$ . . . . .	124
3.9	$\gamma$ . . . . .	124
3.10	$\phi_\gamma$ . . . . .	125
3.11	$\hat{a}_\mu^{\pi\pi}$ . . . . .	125
3.12	Comments on $\rho''$ . . . . .	125
	APPENDICES . . . . .	128
A	PHOTON RESOLUTION PLOTS . . . . .	128
1	Energy Resolution Plots . . . . .	128
2	Neutral Theta( $\theta$ ) Resolution Plots . . . . .	130
3	Neutral Phi( $\phi$ ) Resolution Plots . . . . .	132
B	GTVL . . . . .	143
	REFERENCES . . . . .	144

## LIST OF FIGURES

Figure	Page
I.1 Comparison between $\pi\pi$ spectral function from $\tau$ experiments of CLEO, OPAL and ALEPH, taken from [7]. The two most precise results from ALEPH and CLEO are in agreement. The statistics are comparable in both cases, however due to flat acceptance in ALEPH and an increasing one in CLEO, ALEPH result has better precision below $\rho$ peak, while CLEO's has better precision above $\rho$ peak. . . . .	5
I.2 Comparison between $\pi\pi$ spectral function from $\tau$ and $e^+e^-$ experiments, taken from [7]. The green bar shows the average $\tau^- \rightarrow \pi^-\pi^0\nu_\tau$ from ALEPH, CLEO and OPAL. The $e^+e^-$ data are taken from CMD-2 [8], DM1 [9], DM2 [10], OLYA [11] OLYA-CMD [12], TOF [13]. All error bars shown contain statistical and systematic errors. Visually, the agreement appears to be satisfactory, however the large dynamical range involved does not permit an accurate test. To do so, the $e^+e^-$ data are plotted as a point-by-point ratio to the $\tau$ spectral function. . . . .	8
I.3 Relative comparison of the $\tau$ data(average) and $\pi^+\pi^-$ spectral functions from $e^+e^-$ data taken from [7]. The shaded band is the uncertainty on the $\tau$ spectral function. There are small discrepancies between $e^+e^-$ and $\tau$ data, particularly in $\rho$ peak region. . . . .	9

Figure	Page
II.1 Representative diagrams contributing to $a_\mu$ . First column: lowest-order diagram (upper) and first order QED correction (lower); second column: lowest-order hadronic contribution (upper) and hadronic light-by-light scattering (lower); third column: weak interaction diagrams; last column: possible contributions from lowest-order Supersymmetry. . . . .	12
IV.1 PEP-II . . . . .	19
IV.2 BABAR Detector. The detector is designed according to the boosted CM system. The interaction point is not at the geometrical center of the detector. It is shifted towards the backward direction which is defined by the outgoing low energy beam. . . . .	22
IV.3 BABAR detector end view. . . . .	23
IV.4 Transverse section of Silicon Vertex Tracker(SVT). . . . .	25
IV.5 The plot of longitudinal section of Drift Chamber(DCH). The chamber is offset by 370 mm from the interaction point(IP) . . . . .	26
IV.6 The detector for internally reflected Cherenkov light(DIRC). The Cherenkov light is internally reflected until it gets detected in the water-filled readout reservoir. . . . .	28
IV.7 The longitudinal view of the Electromagnetic Calorimeter(only the top half is shown) indicating arrangement of the 56 crystal rings. The detector is axially symmetric around $z$ -axis. All number are given in milimeter . . .	30
IV.8 The Electromagnetic Calorimeter(EMC) barrel support structure, with great details on the modules and electronic crates . . . . .	32
IV.9 The plot of one wrapped CsI(Tl) Crystal and the front-end readout package mounted on the rear face. . . . .	33

Figure	Page
IV.10 Overview of the IFR: Barrel sectors and forward (FW) and backward (BW) end doors; the shape of the RPC modules and their dimensions are indicated. . . . .	40
V.1 Integrated Luminosity of BABAR Detector . . . . .	49
VI.1 Thrust Magnitude of MC and Data, all preselection cuts have been applied, except thrust magnitude cut. All MC samples are normalized to Data Luminosity. . . . .	57
VI.2 The number of photon in signal hemisphere of MC and Data Distribution, all selection cuts have been applied, except number of cluster cut. All MC are normalized to Data Luminosity. . . . .	58
VII.1 Simplified picture of event reconstruction in this analysis. . . . .	60
VII.2 The $\pi^-$ Momentum (in GeV/c) of the signal $\pi^-\pi^0$ , in the LAB frame. All Monte Carlo samples are generated using SP8 and normalized to collected Data Luminosity. DATA and Monte Carlo show good agreement, All cuts have been applied, except $\pi^-$ Momentum cut. . . . .	61
VII.3 The $\gamma$ Candidate Energy (in GeV) on the signal side, in the LAB frame. All MC samples are normalized to the collected Data Luminosity. DATA and MC show good agreement, all cuts have been applied, except $\gamma$ energy cut. . . . .	62
VII.4 The $\pi^0$ Momentum (in GeV/c) of the signal $\pi^-\pi^0$ , in the LAB frame. All MC samples are normalized to the collected Data Luminosity. DATA and MC show good agreement, all cuts have been applied, except $\pi^-$ Momentum cut. . . . .	63

Figure	Page
VII.5 The $\pi^0$ invariant mass (in GeV) of the signal $\pi^-\pi^0$ . All MC samples are normalized to the collected Data Luminosity. DATA and MC show good agreement, all cuts have been applied, except $\pi^0$ Mass cut. . . . .	63
VII.6 Polar Angle of Missing Momentum $\theta_{miss}$ (rad) of the event in the LAB frame. All MC samples are normalized to the collected Data Luminosity. DATA and MC show good agreement, All cuts have been applied, except polar angle of missing momentum $\theta_{miss}$ cut. The lower plot is the zoom for high polar angle region, where cut is applied to reduce the contributions from non-signal events. . . . .	64
VII.7 The Polar Angle of $\pi^-$ (rad) in the LAB frame. All MC samples are normalized to the collected Data Luminosity. DATA and MC show good agreement, all cuts have been applied, except the polar angle of $\pi^-$ cut. The lower plot is the zoom for high polar angle region, cuts are applied to non-signal events. . . . .	65
VII.8 The plot of the $\pi^-\pi^0$ invariant mass of Data(black dots) and MC samples, all Monte Carlo samples are normalized to data luminosity. The major backgrounds are the contributions from non signal $\tau$ and continuum $q\bar{q}$ backgrounds . . . . .	68
VII.9 The plot of $\pi^-\pi^0$ invariant mass after MC backgrounds are subtracted from Data. The dip about 1.5 GeV shows a destructive interference between $\rho'$ and $\rho''$ . . . . .	69
VII.10 The efficiency plot, as defined by the number of selected $\pi^-\pi^0$ events divided by the number of generated $\pi^-\pi^0$ events, plotted as a function of $\pi^-\pi^0$ invariant mass. . . . .	69

Figure	Page
VIII.1 Unfolding Matrix in 2D. The upper plot is the unfolding matrix for full MC with $0.3 \text{ GeV} < M_{\pi^-\pi^0} < 2.8 \text{ GeV}$ . The lower plot is the unfolding matrix for lower mass region MC with $0.3 \text{ GeV} < M_{\pi^-\pi^0} < 1.8 \text{ GeV}$ . Efficiency is not included. . . . .	73
VIII.2 Unfolding Matrix in 3D. The upper plot is the unfolding matrix in box style for full MC with $0.3 \text{ GeV} < M_{\pi^-\pi^0} < 2.8 \text{ GeV}$ . The lower plot is the unfolding matrix in box style for lower mass region MC with $0.3 \text{ GeV} < M_{\pi^-\pi^0} < 1.8 \text{ GeV}$ . Efficiency is not included. . . . .	74
VIII.3 The Reconstruction Mass - The True Mass and fit it using Gaussian. The 0s are the mean value of invariant mass of the specific truth bins . . .	75
VIII.4 Comparison between background-subtracted DATA(black) and Unfolded DATA(red) . . . . .	76
IX.1 Fitting to Unfolded Background Subtracted Data using Gounaris Sakurai Function . . . . .	78
IX.2 The pion Form factor $ F ^2$ as derived from the spectral function of selected Data after background subtraction . . . . .	80
X.1 The upper left plot is the comparison between Reconstructed(black) and Detected(red) $E_\gamma^{MC}$ . The upper right plot is the comparison between Reconstructed(black) and Detected(red) $E_\gamma^{Data}$ . The lower right plot is the comparison between efficiency of Data(black) and MC(red). The lower left plot is the ratio between efficiency Data and MC. . . . .	87
X.2 Comparison of Muon Momentum between Data(circle) and MC(square) from $e^+e^- \rightarrow \mu^+\mu^-\gamma$ samples. MC is normalized to Data Luminosity . . .	88

Figure	Page
X.3 Comparison of Cosine Theta(LAB) of Muon between Data(circle) and MC(square) from $e^+e^- \rightarrow \mu^+\mu^-\gamma$ samples. MC is normalized to Data Luminosity . . . . .	88
X.4 Comparison between selected photon energy Data, MC and Corrected-MC. Corrected MC is MC after photon efficiency correction applied which calculated using $\mu\mu\gamma$ sample. Both MCs are normalized to Data Luminosity. . . . .	89
X.5 Comparison between selected $M_{\gamma\gamma}$ of Data, MC and Corrected-MC. Both MCs are normalized to Data Luminosity. Corrected MC is MC after photon efficiency correction which calculated using $\mu\mu\gamma$ sample. . . . .	90
X.6 The Cosine of Opening Angle between 2 photons of $\pi^0$ in LAB frame after all selection cuts applied. From top to bottom, the plots are zoomed. Top plot ranges from 0.5-1, Mid plot ranges from 0.95-1 and Bottom plot ranges from 0.995-1. MC is normalized to Data Luminosity. . . . .	91
X.7 The opening angle of selected 2 photons of $\pi^0$ decay(LAB frame) after all selection cuts applied. Corrected MC is MC after photon efficiency correction which calculated using $\mu\mu\gamma$ sample. . . . .	92
X.8 The total mass on the 3 Prong side(tag side), assuming the 3 tracks are pions after all cuts applied, x axis is in GeV. MC is normalized to Data Luminosity. . . . .	99
X.9 The total mass on the 3 Prong side above tau Mass, assuming the 3 tracks are pions after all cuts applied, x axis is in GeV . . . . .	100
X.10 The Signal $\pi^-\pi^0$ invariant mass of some events which have total mass on 3 prong side bigger than 1.8 GeV (Log Scale). . . . .	101

Figure	Page
X.11 The invariant $\pi^-\pi^0$ Mass from major contributors to $\tau$ background, after all cuts applied. The horizontal line is in GeV . . . . .	103
X.12 The invariant $\pi^-\pi^0\pi^0$ mass, all MCs all normalized to Data Luminosity. We see that there is no significance difference between Data and MC in simulating $\tau^- \rightarrow \pi^-\pi^0\pi^0\nu_\tau$ . . . . .	109
A.1 Energy Resolution Data All Runs. . . . .	128
A.2 Energy Resolution MC All Runs. . . . .	128
A.3 Energy Resolution Data(black line) and MC(red line) All Runs. . . . .	129
A.4 After Energy smearing: MC after smearing(blue line), initial MC(red line) and Data(black line) All Runs. . . . .	129
A.5 Theta Resolution Data All Runs. . . . .	130
A.6 Theta Resolution MC All Runs. . . . .	130
A.7 Theta( $\theta$ ) Resolution Data(black line) and MC(red line) All Runs. . . . .	131
A.8 Neutral Theta( $\theta$ ) smearing result. After $\theta$ smearing: MC after smearing(blue line), initial MC(red line) and Data(black line) All Runs. . . . .	131
A.9 Phi Resolution Data All Runs. . . . .	132
A.10 Phi Resolution MC All Runs. . . . .	132
A.11 Phi( $\phi$ ) Resolution Data(black line) and MC(red line) All Runs. . . . .	133
A.12 After $\phi$ smearing: MC after smearing(blue line), initial MC(red line) and Data(black line) All Runs. . . . .	133
A.13 Linear fit ( $y = a + bx$ ) to scale and resolution (smearing) parameters. . .	134

## LIST OF TABLES

Table	Page
I.1 Standard Model . . . . .	2
V.1 DATA and MC . . . . .	48
V.2 Generated Monte Carlo events for this analysis . . . . .	51
VI.1 Event PreSelection Table After Tau1N. Preselection efficiencies in percent for Data and Monte Carlo background samples. Cuts are applied sequentially and the marginal efficiencies are quoted . . .	56
VII.1 Event Selection Table in sequential percentage(%) of efficiency after each cut. MC is normalized to data luminosity . . . . .	66
IX.1 Fitting Result with Gounaris Sakurai Function. The statistical errors are shown in the table . . . . .	78
IX.2 Correlation Matrix between fit parameters . . . . .	79
X.1 Parameters after Track Efficiency correction. The number in parentheses are only statistical errors. . . . .	84
X.2 Fitting parameters before and after linear $\pi^0$ efficiency correction. We also include the uncertainties of $a(\sigma_a)$ and $b(\sigma_b)$ , by varying their $1\sigma$ up and down. The number in parentheses are only statistical errors. . . . .	93

Table	Page
X.3 GS Fitting Parameters after $\theta_{track}$ resolution correction. The number in parentheses are only the statistical errors. . . . .	95
X.4 GS Fitting Parameters after $P_{track}$ resolution correction. The number in parentheses are only statistical errors. . . . .	96
X.5 Photon Resolution Uncertainties. The numbers in parentheses are only statistical errors. . . . .	98
X.6 We estimate the contribution of uds background uncertainty using the ratio of Data and MC above tau mass ( 1.8 GeV). After varying the uds background contribution by its uncertainty $\pm\sigma$ , we refit the spectrum using GS function. This table shows the parameters before(default values) and after uds background variation. The numbers in parentheses are only statistical errors. . . . .	100
X.7 After cuts applied, the $\tau$ backgrounds are reduced significantly. This table shows the main $\tau$ decays that contributes to $\tau$ Backgrounds after all cuts applied. . . . .	102
X.8 Parameters after $\tau^- \rightarrow e^-\nu_e\nu_\tau$ background variation. The number in parentheses are only statistical errors. . . . .	104
X.9 Parameters after $\tau^- \rightarrow \pi^-\nu_\tau$ background variation(MC Mode 3). The number in parentheses are only statistical errors. . . . .	105
X.10 Parameters after $\tau^- \rightarrow a_1 \rightarrow \pi^-\pi^0\pi^0\nu_\tau$ background variation. The number in parentheses are only statistical errors. . . . .	105
X.11 We vary the contribution of $\tau^- \rightarrow a_1 \rightarrow \pi^-\pi^0\pi^0\nu_\tau$ due to possibility that 1 missing $\pi^0$ of a1 can be mis-identified as signal. The number in parentheses are only statistical errors. . . . .	106

Table	Page
X.12 Parameters after $\tau^- \rightarrow K^- K^0 \pi^0 \nu_\tau$ background variation. The number in parentheses are only statistical errors. . . . .	106
X.13 Parameters after $\tau^- \rightarrow \pi^- K^0 \pi^0 \nu_\tau$ background variation. The number in parentheses are only statistical errors. . . . .	107
X.14 Parameters after $\tau^- \rightarrow K^{*-} \rightarrow K^- \pi^0 \nu_\tau$ background variation. The number in parentheses are only statistical errors. . . . .	107
X.15 We also vary the track efficiency correction to $\tau^- \rightarrow K^{*-} \rightarrow K^- \pi^0 \nu_\tau$ background. The number in parentheses are only statistical errors. . . . .	108
X.16 GS Fitting Parameters with 5, 10 and 50 MeV Bins. The number in parentheses are only statistical errors. . . . .	111
X.17 Fitting parameters with and without unfolding. We also compare it with unbinned fitting. The number in parentheses are statistical errors. . . . .	112
X.18 The Branching Fraction $\tau^- \rightarrow \pi^- \pi^0 \nu_\tau$ for 5 different Runs. . . . .	113
X.19 Fitting parameters for 5 different runs. The number in parentheses are only statistical errors. . . . .	114
X.20 The errors are only statistical and we find that the fitting parameters for both KS and GS models are consistent within the statistical errors. . . . .	115
X.21 Summary of fitting parameters and their experimental uncertainties . . . . .	116
X.22 Final fitting parameters and their experimental uncertainties . . . . .	117
XI.1 External Parameters and their uncertainties . . . . .	121
XI.2 The results of fitting to the $M_{\pi\pi^0}$ distribution using Gounaris-Sakurai function from some experiments . . . . .	126
XI.3 The results of $\hat{a}_\mu^{\pi\pi}$ from some experiments . . . . .	127

Table	Page
A.1 Energy Resolution Data Run 1-5 . . . . .	135
A.2 Energy Resolution Run MC 1-5 . . . . .	136
A.3 Energy Resolution Run MC 1-5 After Smearing . . . . .	137
A.4 Energy Smearing . . . . .	138
A.5 Theta( $\theta$ ) Resolution Run 1-5 . . . . .	139
A.6 Theta( $\theta$ ) Smearing . . . . .	140
A.7 Theta( $\theta$ ) After Smearing . . . . .	140
A.8 Phi( $\phi$ ) Resolution Run 1-5 . . . . .	141
A.9 Phi( $\phi$ ) Smearing . . . . .	142
A.10 Phi( $\theta$ ) After Smearing . . . . .	142
A.11 Fit to photon scale and resolution parameters . . . . .	142
B.1 Good Track Candidate . . . . .	143

## CHAPTER I

### INTRODUCTION

The Standard Model(SM) of particle physics predicts all matter is made of six leptons and six quarks. In addition, for every matter particle there is an antiparticle with exactly the same mass but opposite-signed additive quantum numbers (e.g. electric charge). Leptons are divided into three families: the first family consists of electron(e) and electron neutrino( $\nu_e$ ), the second family consists of muon( $\mu$ ) and muon neutrino( $\nu_\mu$ ), the third family consists of tau( $\tau$ ) and tau neutrino( $\nu_\tau$ ). The electron(e), muon( $\mu$ ) and tau( $\tau$ ) have a negative charge, while the neutrinos( $\nu$ ) are electrically neutral. Each of the leptons carries its own family lepton number. In the Standard Model, lepton number is always conserved. For instance, the lepton decay is always accompanied with a neutrino to conserve the lepton number.

There are six quarks with six different “flavors”(see Table I.1). The up(u), charm(c) and top(t) quarks have a positive charge  $+2/3e$ (in units of electron charge), while the down(d), strange(s) and bottom(b) quarks have a negative charge  $-1/3e$ . Both leptons and quarks are spin-1/2 particles, or fermions. Unlike leptons, quarks are never found alone. They are confined to groups with other quarks, forming baryons (bound state of three quarks) and mesons (bound state of a quark-antiquark pair).

There are four known forces responsible for interactions between the fundamental particles: strong, electromagnetic, weak and gravitational. Each force is mediated

Quark		Lepton	
up(u)	down(d)	electron(e)	neutrino electron( $\nu_e$ )
charm(c)	strange(s)	muon( $\mu$ )	neutrino muon( $\nu_\mu$ )
top(t)	bottom(b)	tau( $\tau$ )	neutrino tau( $\nu_\tau$ )

Tab. I.1: Standard Model

by one or more interaction-specific particle(s), gauge boson(s) (integer-spin particle). Particles interact by exchanging gauge bosons. These force-carrier particles are fundamental, but are not considered as matter particles.

## 1 Hadronic Tau Decay

Martin Perl et. al. discovered the  $\tau$  lepton in 1975 using MARK I detector at the Stanford Linear Accelerator Center [1]. The mass of  $\tau$  lepton is  $1776.90 \pm 0.20$  MeV[2] and its lifetime is  $(290.6 \pm 1.0) \times 10^{-15}$  s[2]. The  $\tau$  lepton is the only lepton heavy enough to decay into hadrons, and as this decay involves a pure charged-current interaction it makes an excellent system for studying the coupling of hadrons to weak current. This analysis will measure the hadronic decay spectrum of  $\tau^- \rightarrow \pi^-\pi^0\nu_\tau$  decays <sup>1</sup>.

The invariant amplitude for semileptonic(hadronic)  $\tau$  decays can be written in the form

$$M(\tau \rightarrow X^-\nu_\tau) = \frac{G_F}{\sqrt{2}} |V_{CKM}| L_\mu H^\mu, \quad (\text{I.1})$$

where  $H^\mu$  represents a specific hadronic system,  $V_{CKM}$  is the corresponding element of the Cabibbo-Kobayashi-Maskawa matrix ( $V_{ud}$  for non-strange and  $V_{us}$  for strange) and  $G_F$  denotes the Fermi coupling constant. The leptonic current is given by

---

<sup>1</sup>Charge conjugation is implied throughout this analysis

$$L_\mu = \bar{\nu}_\tau \gamma_\mu (1 - \gamma_5) \tau, \quad (\text{I.2})$$

which can be called charged weak current.

The hadronic final states in tau decays can be classified as either vector or axial vector based on the isotopic parity ( $G$ -parity); the operation of isospin rotation followed by charge conjugation. The conservation of  $G$ -parity implies that, in the case of the decay of a  $\tau$  lepton to pions, decay modes with an even number of pions will proceed via the vector current, while those with an odd number of pions will proceed via the axial-vector current. The measurement of non-strange  $\tau$  vector current properties requires the measurement of  $\tau$  decay modes with a parity  $G=+1$ . Similarly, the measurement of  $\tau$  axial-vector current properties requires decay modes with  $G=-1$ .

## 2 Spectral Function of $\tau^- \rightarrow \pi^- \pi^0 \nu_\tau$ Decays

The differential decay rate of  $\tau^- \rightarrow \pi^- \pi^0 \nu_\tau$  decays normalized to the total decay width is related to the spectral function  $v_-(s)$  as [3]:

$$\frac{1}{\Gamma} \frac{d\Gamma}{ds} (\tau^- \rightarrow \pi^- \pi^0 \nu_\tau) = \frac{6\pi |V_{ud}| S_{EW}^{\pi\pi}}{M_\tau^2} \frac{B_e}{B_{\pi\pi}} \left(1 - \frac{s}{M_\tau^2}\right)^2 \left(1 + \frac{2s}{M_\tau^2}\right)^2 v_-(s), \quad (\text{I.3})$$

where  $s = q^2$  is the invariant mass squared of the  $\pi^- \pi^0$  system,  $V_{ud}$  is the Cabibbo-Kobayashi-Maskawa matrix element,  $B_e$  is the branching fraction of  $\tau^- \rightarrow e^- \bar{\nu}_e \nu_\tau$ ,  $B_{\pi\pi}$  is the branching fraction of  $\tau^- \rightarrow \pi^- \pi^0 \nu_\tau$ ,  $M_\tau$  is the  $\tau$  lepton mass, and  $S_{EW}^{\pi\pi}$  denotes electroweak radiative corrections. The data from  $\tau^- \rightarrow \pi^- \pi^0 \nu_\tau$  decays is expected to be dominated by production of the lowest lying vector meson, the  $\rho(770)$ , while radial excitations, such as the  $\rho(1450)$  and  $\rho(1700)$ , may also contribute. The interference of these mesons in  $\tau$  decays are of significant interest and new data are important.

The  $\tau$  spectral function is related to the charged pion form factor(see Chapter III for phenomenological models of form factor) as

$$v_-(s) = \frac{\beta_-^3(s)}{12\pi} |F_\pi^-(s)|^2, \quad (\text{I.4})$$

The threshold functions  $\beta_{0,-}$  are defined by

$$\beta_{0,-} = \beta(s, m_{\pi^-}, m_{\pi^{+,0}}), \quad (\text{I.5})$$

where

$$\beta(s, m_1, m_2) = \left[ \left( 1 - \frac{(m_1 + m_2)^2}{s} \right) \left( 1 - \frac{(m_1 - m_2)^2}{s} \right) \right]^{1/2}. \quad (\text{I.6})$$

Spectral function measurements for the two pion final state  $\tau^- \rightarrow \pi^-\pi^0\nu_\tau$  are available from ALEPH [4], CLEO [5] and OPAL [6]. They are compared in Figure I.1 and the two most precise results from ALEPH and CLEO are in agreement. The statistics are comparable in both cases, however due to flat acceptance in ALEPH and an increasing one in CLEO, the ALEPH result has better precision below  $\rho$  peak, while the CLEO result has better precision above  $\rho$  peak.

### 3 Comparison to $e^+e^-$ Data

The Conserved Vector Current (CVC) relates the spectral function from the  $\tau$  decay to the  $\pi^+\pi^-$  spectral function produced in the reaction  $e^+e^- \rightarrow \pi^+\pi^-$  in the limit of exact isospin symmetry. The  $e^+e^- \rightarrow \pi^+\pi^-$  data is used to determine the hadronic vacuum polarization correction to the photon propagator, which is needed to understand many precision electroweak measurements. In particular, this data is needed to understand the SM prediction for the anomalous magnetic moment of muon  $a_\mu = (g_\mu - 2)/2$ , where  $g_\mu$  is the gyromagnetic ratio of muon(see Chapter II for

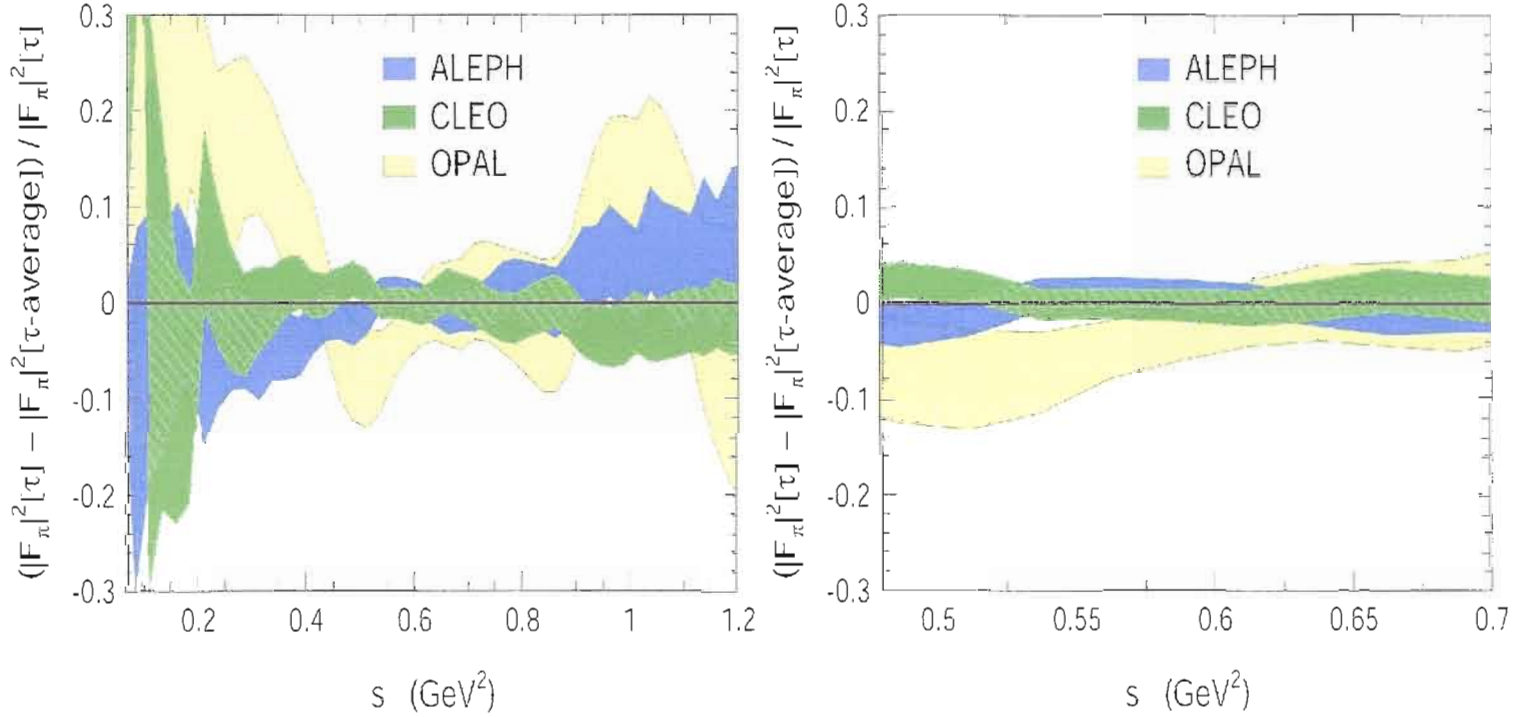


Fig. I.1: Comparison between  $\pi\pi$  spectral function from  $\tau$  experiments of CLEO, OPAL and ALEPH, taken from [7]. The two most precise results from ALEPH and CLEO are in agreement. The statistics are comparable in both cases, however due to flat acceptance in ALEPH and an increasing one in CLEO, ALEPH result has better precision below  $\rho$  peak, while CLEO's has better precision above  $\rho$  peak.

more detail). The theoretical calculation of the hadronic vacuum polarization involves QCD, which is a non-Abelian theory with massless gauge bosons, calculation using its perturbative expansion at low energies is not well behaved, so that experimental data are needed to complete the theory. Using CVC, the  $\tau$  data can be used to augment the  $e^+e^-$  data, leading to a more precise theoretical calculation of the hadronic vacuum polarization contribution to  $a_\mu$ [7].

The  $\pi\pi$  spectral function is related to the  $e^+e^-$  data as

$$\sigma(e^+e^- \rightarrow \pi^+\pi^-) = \frac{4\pi\alpha^2}{s} v_0(s), \quad (\text{I.7})$$

where the spectral function  $v_0(s)$  is related to the pion form factor  $F_\pi^0(s)$  by

$$v_0(s) = \frac{\beta_0^3(s)}{12\pi} |F_\pi^0(s)|^2, \quad (\text{I.8})$$

where  $\beta_0(s)$ (see Equation I.5) is the threshold kinematic factor.

Isospin symmetry implies

$$v_-(s) = v_0(s), \quad (\text{I.9})$$

which mean that in the limit exact isospin symmetry the spectral function from  $e^+e^- \rightarrow \pi^+\pi^-$  and  $\tau \rightarrow \pi^-\pi^0\nu_\tau$  are equal. But there are corrections need to applied due the fact that isospin symmetry is not exact. The most important is the inclusion of  $\rho - \omega$  interference which is only present in neutral system, but other small corrections are also needed(see Chapter XI Section 1).

The  $2\pi$  vector spectral functions extracted from  $e^+e^-$  and  $\tau$  data are compared in Figure I.2. The  $e^+e^-$  data are taken from CMD-2 [8], DM1 [9], DM2 [10], OLYA [11] OLYA-CMD [12], TOF [13]. The green bar shows the average  $\tau^- \rightarrow \pi^-\pi^0\nu_\tau$  spectral function from ALEPH, CLEO and OPAL. All error bars shown contain statistical and systematic errors. The  $\tau$  data in this plot has been corrected for some

SU(2)-breaking(notably  $\rho - \omega$  interference). Visually, the agreement appears to be satisfactory, however if the data are compared in detail the  $e^+e^-$  and  $\tau$  do not agree, particularly in  $\rho$  peak region(see Figure I.3). These small differences have significant implications for the SM prediction of  $a_\mu$ (see Chapter II) and should be better understood. With the large BABAR data sample, a more precise determination can be made which may help to clarify the situation.

## 4 Analysis Overview

We use the data recorded by the BABAR Detector, which is described in Chapter IV. Description about our Data and Simulation(named as Monte Carlo or MC) can be found in Chapter V. The event selection used to improve the ratio of signal to background in our data is described in Chapters VI and VII.

The measurement of the hadronic  $\tau$  spectral function requires the determination of the physical invariant  $\pi^-\pi^0$  mass from the selected events. To extract it from the measured invariant  $\pi^-\pi^0$  mass, we subtract all background(non  $\tau^- \rightarrow \pi^-\pi^0\nu_\tau$  events) from Data using MC. The invariant  $\pi^-\pi^0$  mass after background subtraction is **unfolded** using Singular Value Decomposition(SVD) method. Some plots and more infomation about Unfolding and SVD can be seen in Chapter VIII.

Gounaris-Sakurai function(default fitting function) is used to fit the unfolded-background subtracted Data to extract the values of resonance parameters and  $a_\mu^{\pi\pi}$ (see Chapter IX). Systematic uncertainties are discussed in Chapter X.

The results of this analysis are presented and compared to some results from previous  $e^+e^-$  and  $\tau$  experiments(see Chapter XI).

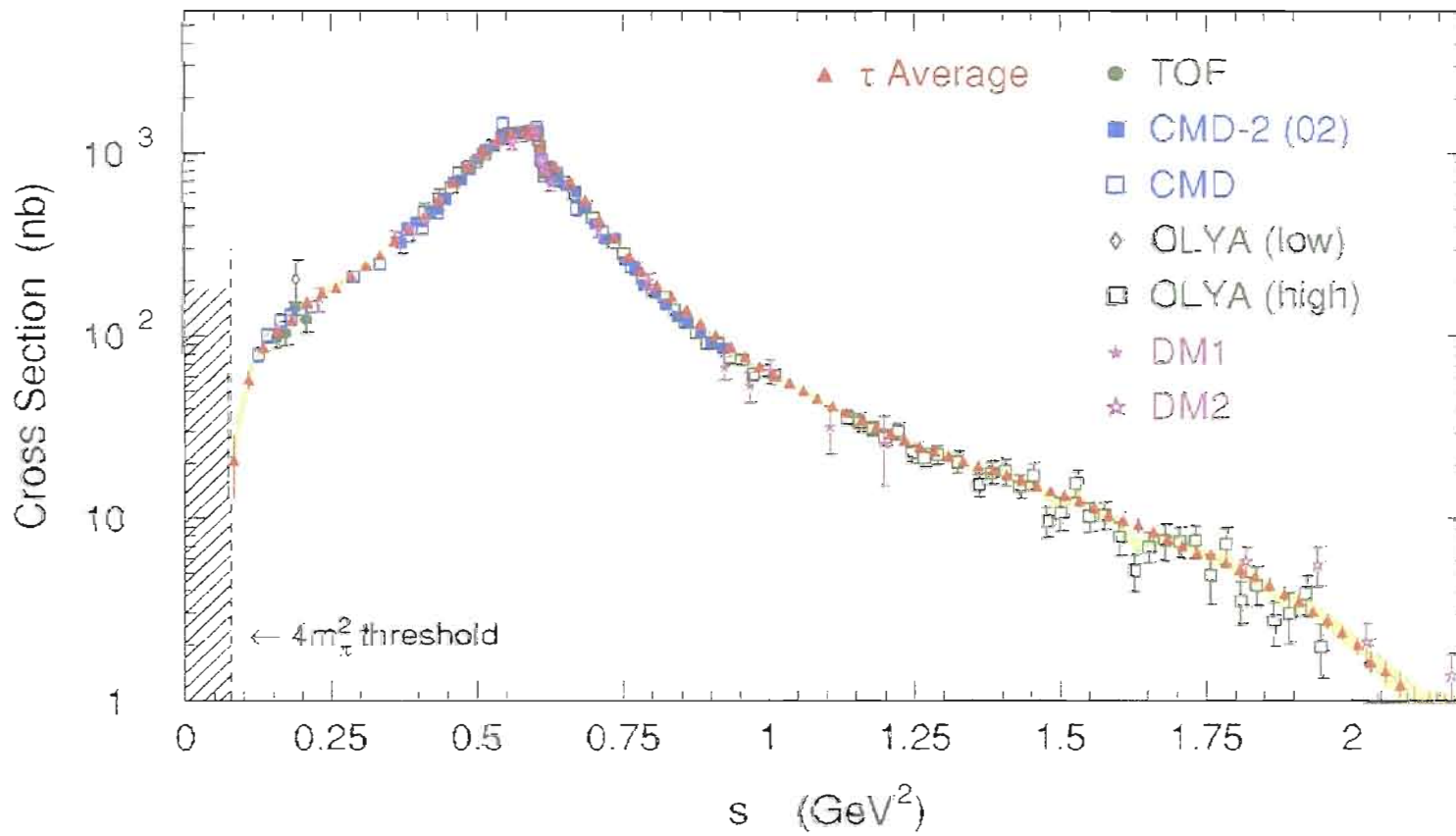


Fig. I.2: Comparison between  $\pi\pi$  spectral function from  $\tau$  and  $e^+e^-$  experiments, taken from [7]. The green bar shows the average  $\tau^- \rightarrow \pi^- \pi^0 \nu_\tau$  from ALEPH, CLEO and OPAL. The  $e^+e^-$  data are taken from CMD-2 [8], DM1 [9], DM2 [10], OLYA [11] OLYA-CMD [12], TOF [13]. All error bars shown contain statistical and systematic errors. Visually, the agreement appears to be satisfactory, however the large dynamical range involved does not permit an accurate test. To do so, the  $e^+e^-$  data are plotted as a point-by-point ratio to the  $\tau$  spectral function.

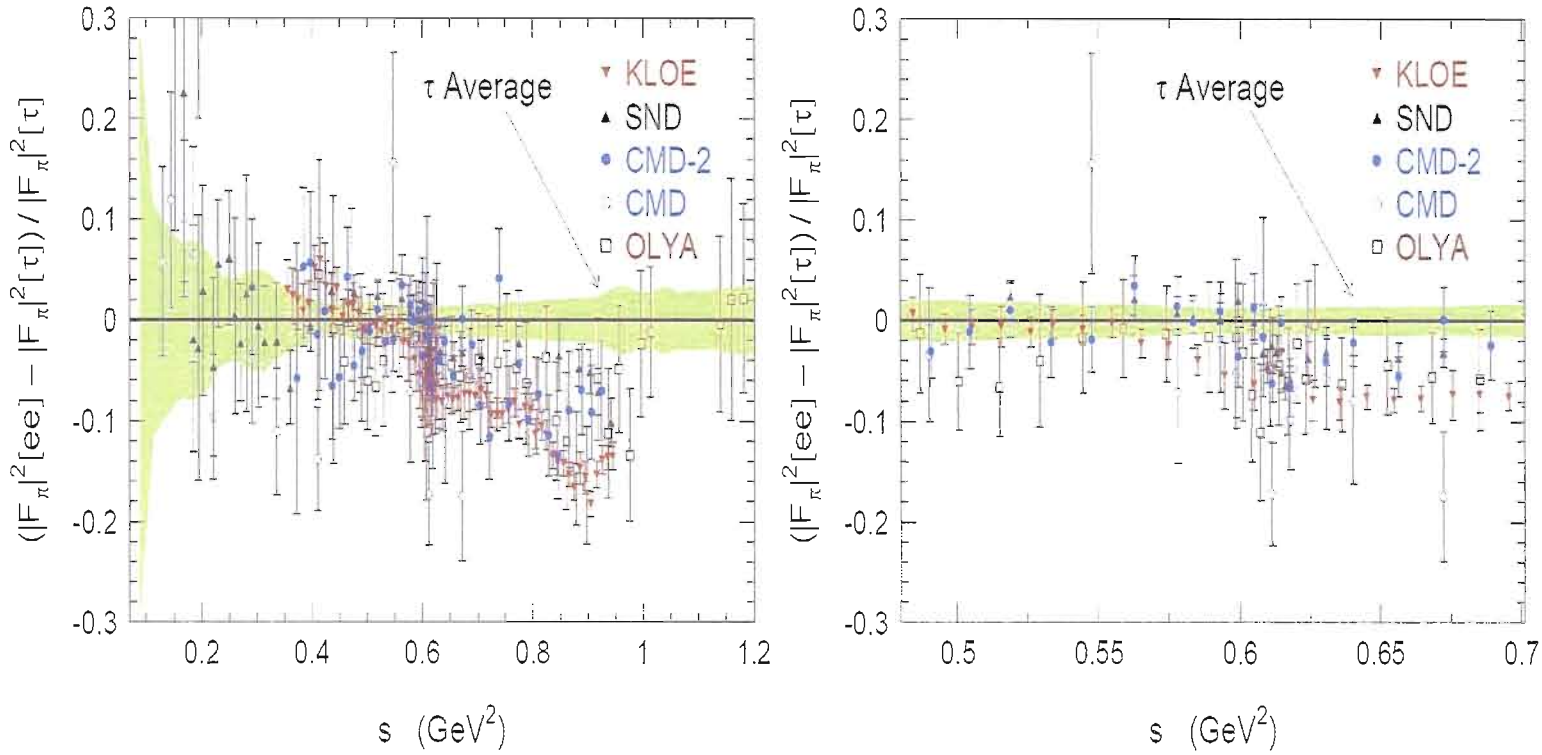


Fig. I.3: Relative comparison of the  $\tau$  data(average) and  $\pi^+\pi^-$  spectral functions from  $e^+e^-$  data taken from [7]. The shaded band is the uncertainty on the  $\tau$  spectral function. There are small discrepancies between  $e^+e^-$  and  $\tau$  data, particularly in  $\rho$  peak region.

## CHAPTER II

### OVERVIEW OF MUON MAGNETIC ANOMALY

One of the great successes of the Dirac equation [14] was its prediction that the magnetic dipole moment,  $\vec{\mu}_l$ , of a spin  $|\vec{s}| = \frac{1}{2}$  particle such as the electron (or muon) is given by

$$\vec{\mu}_l = g_l \frac{e}{2m_l} \vec{s} \quad (\text{II.1})$$

with gyromagnetic ratio  $g_l = 2$ , a value already implied by early atomic spectroscopy. Later it was realized that a relativistic quantum field theory such as QED can give rise via quantum fluctuations to a shift in  $g_l$

$$a_l = \frac{g_l - 2}{2}, \quad (\text{II.2})$$

called the magnetic anomaly. In classic QED calculation, Schwinger [15] found the leading (one loop) effect (Figure II.1, lower-left)  $a_l = \frac{\alpha}{2\pi} \simeq 0.00116$ , with  $\alpha = \frac{e^2}{4\pi} \simeq 1/137.036$ , which agreed beautifully with experiment [16],[17], thereby providing strong confidence in the validity of perturbative QED. Today, the tradition of testing QED and its  $SU(3)_C \times SU(2)_L \times U(1)_Y$  SM extension is continued (which includes strong and electroweak interactions) by measuring  $a_l^{exp}$  for the electron and muon even more precisely and comparing with  $a_l^{SM}$  expectations, calculated to much

higher order in perturbation theory. Such comparisons test the validity of the SM and probe for new physics effects, which if present in quantum loop fluctuations should cause disagreement at some level. An experiment underway at Harvard [18] aims to improve the best present measurement [19] of  $a_e$  by about a factor of 15. Combined with a much improved independent determination of  $\alpha$ , it would significantly test the validity of perturbative QED. It should be noted, however, that  $a_e$  is in general not very sensitive to new physics at a high mass scale  $\Lambda$  because its effect on  $a_e$  is expected to be quadratic in  $\frac{1}{\Lambda}$  (see [20])

$$\Delta a_e(\Lambda) \sim O\left(\frac{m_e^2}{\Lambda^2}\right) \quad (\text{II.3})$$

and, hence, highly suppressed by the smallness of the electron mass. It would be much more sensitive if  $\Delta a_e$  were linear in  $\frac{1}{\Lambda}$ ; but that is unlikely if chiral symmetry is present in the  $m_e \rightarrow 0$  limit.

The muon magnetic anomaly has been measured with a relative precision of  $5 \times 10^{-7}$  by the E821 collaboration at Brookhaven National Laboratory (see [21],[22],[23] and [24]). Combined with the older, less precise results from CERN [25], and averaging over charges, gives

$$a_\mu^{exp} = (11,659,208.0 \pm 5.8) \times 10^{-10}. \quad (\text{II.4})$$

Although the accuracy is 200 times worse than  $a_e^{exp}$ ,  $a_\mu$  is about  $\frac{m_\mu^2}{m_e^2} \simeq 40000$  times more sensitive to new physics and hence a better place (by about a factor of 200) to search for a deviation from the SM expectation. Of course, strong and electroweak contributions to  $a_\mu$  are also enhanced by  $\frac{m_\mu^2}{m_e^2}$  relative to  $a_e$ ; so, they must be evaluated much more precisely in any meaningful comparison of  $a_\mu^{SM}$  with Equation II.5. Fortunately, the recent experimental progress in  $a_\mu^{exp}$  has stimulated much theoretical

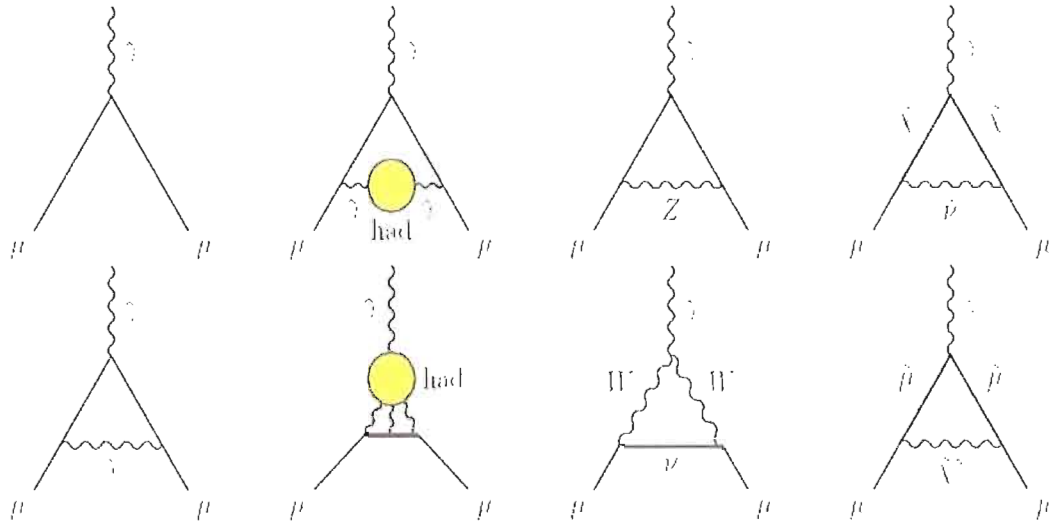


Fig. II.1: Representative diagrams contributing to  $a_\mu$ . First column: lowest-order diagram (upper) and first order QED correction (lower); second column: lowest-order hadronic contribution (upper) and hadronic light-by-light scattering (lower); third column: weak interaction diagrams; last column: possible contributions from lowest-order Supersymmetry.

improvement of  $a_\mu^{SM}$ , uncovering errors and inspiring new computational approaches along the way, among these the use of hadronic  $\tau$  decays.

It is convenient to separate the SM prediction for the anomalous magnetic moment of the muon into its different contributions,

$$a_\mu^{SM} = a_\mu^{QED} + a_\mu^{weak} + a_\mu^{had}, \quad (\text{II.5})$$

where  $a_\mu^{QED} = (11,658,472.0 \pm 0.2) \times 10^{-10}$  is the pure electromagnetic contribution (see [26] and [27] and references therein),  $a_\mu^{weak} = (15.4 \pm 0.1 \pm 0.2) \times 10^{-10}$ , with the first error being the hadronic uncertainty and the second due to the Higgs mass range, accounts for corrections due to exchange of the weakly interacting bosons up to two loops.

The term  $a_\mu^{had}$  can be further decomposed into its different contributions

$$a_\mu^{had} = a_\mu^{had,LO} + a_\mu^{had,HO} + a_\mu^{had,LBL}, \quad (\text{II.6})$$

where  $a_\mu^{had,LO}$  is the lowest-order contribution from hadronic vacuum polarization, which involves one-loop terms. The next term,  $a_\mu^{had,HO}$  is the corresponding higher-order part. At the 3-loop level in  $\alpha$ , the so-called hadronic light-by-light (LBL) scattering contributions,  $a_\mu^{had,LBL}$ , must be estimated in a model-dependent approach. Those estimates have been plagued by errors, which now seem to be sorted out[7].

The dominant uncertainty in theoretical calculation of  $a_\mu$  comes from the lowest-order contribution of hadronic vacuum polarization, which is dominated by  $2\pi$  part. Because the loop integration involves low energy scales near the muon mass, the contributions cannot be calculated from perturbative QCD alone and must be measured from experimental  $e^+e^-$  and/or  $\tau$  data.

The hadronic contribution can be improved through hadronic  $\tau$  decays to vector final states, where the weak charged current can be related to the isovector part of the electromagnetic current through the conserved vector current (CVC) hypothesis plus the additional requirements of isospin conservation and the absence of second-class currents (which is the case for the Standard Model).

The leading order hadronic contribution to the muon anomalous magnetic moment ( $a_\mu^{had,LO}$ ) is related to the  $e^+e^-$  annihilation cross section via the dispersion integral.

$$a_\mu^{had,LO} = \left(\frac{\alpha m_\mu}{3\pi}\right)^2 \int_{4m_\pi^2}^\infty \frac{R(s)}{s^2} K(s) ds, \quad (\text{II.7})$$

where  $s$  is the invariant mass squared of the two pion system, and

$$R(s) = \frac{\sigma(e^+e^- \rightarrow \text{hadrons})}{\frac{4\pi\alpha^2}{3s}}, \quad (\text{II.8})$$

where  $K(s)$  is the QED kernel [28],

$$K(s) = x^2(1 - \frac{x^2}{2}) + (1+x)^2(1 + \frac{1}{x^2}) \left[ \ln(1+x) - x + \frac{x^2}{2} \right] + \frac{1+x}{1-x}, x^2 \ln x \quad (\text{II.9})$$

where

$$x = \frac{1 - \beta_\mu}{1 + \beta_\mu}, \quad (\text{II.10})$$

with

$$\beta_\mu = (1 - 4M_\mu^2/s)^{1/2}. \quad (\text{II.11})$$

Using equations, [II.7], [II.8], [I.7] and [I.8](the equation that relates  $\tau$  and  $e^+e^-$  spectral function), we get:

$$a_\mu^{\pi\pi} = \left( \frac{\alpha m_\mu}{3\pi} \right)^2 \int_{4m_\pi^2}^{m_\tau^2} \frac{3v_-(s)}{s^2} K(s) ds + \dots . \quad (\text{II.12})$$

The tau decay only covers a range up to  $s = M_\tau^2$ . Since the kernel  $K(s)$  is a smooth function with  $1/s^2$  dependence, hadronic final states at low energy dominate the contribution to  $(a_\mu^{\text{had},LO})$  and “...” represents the integral above  $\tau$  mass.

The dominant uncertainty on the evaluation of  $a_\mu^{\pi\pi}$  comes from the low energy range above 0.5 GeV, below which improved  $e^+e^-$  data are available from CMD-2[8] and SND[29] have a better precision than the  $\tau$  data. The range of integration used in this analysis is from  $\sqrt{s} = 0.5$  to 1.8 GeV of invariant  $\pi^-\pi^0$  mass, where the  $\tau$  data is more useful than  $e^+e^-$  data. The  $a_\mu^{\pi\pi}$  calculation in this range(0.5-1.8 GeV) from  $\tau$  data has (about 2 times) better precision than  $e^+e^-$  data.

## CHAPTER III

### PHENOMENOLOGICAL MODELS

There are 2 phenomenological models commonly used to parameterize the spectrum in  $\tau^- \rightarrow \pi^-\pi^0\nu_\tau$ , Kuhn & SantaMaria(KS, see [30]) and Gounaris & Sakurai(GS, see [31]). The main difference between these models is a more sophisticated treatment of the Breit-Wigner(BW) function in GS. Both models are expanded to include not only the dominant  $\rho$  resonance, but also incorporates the contribution from  $\rho'$  and  $\rho''$ . The form factor is written as a sum of BW terms:

$$F_\pi^{I=1}(q^2) = \frac{1}{1+\beta+\gamma} (BW_\rho + \beta e^{i\phi_\beta} BW_{\rho'} + \gamma e^{i\phi_\gamma} BW_{\rho''}), \quad (\text{III.1})$$

The real parameters  $\beta$  and  $\gamma$  specify the relative coupling to  $\rho'$  and  $\rho''$ , while the parameters  $\phi^\beta$  and  $\phi^\gamma$  specify the complex phase of each resonance with respect to  $\rho$ . The factor  $1/(1+\beta+\gamma)$  ensures the proper normalization of F.

One can perform  $\chi^2$  fits to the measured  $\pi^-\pi^0$  mass spectrum to extract resonance parameters using these models. In addition, having analytic function for the form factor allows a straightforward numerical integration procedure to be used to evaluate  $a_\mu^{\pi\pi}$ . The  $\chi^2$  minimization and parameter error determination is carried out using the MINUIT program[32] via RooFit[33]. We present results from both GS and KS, and the systematic errors on  $a_\mu^{\pi\pi}$  include the difference between either.

## 1 The Model of Kuhn and Santamaria

One model of pion form factor was proposed by Kuhn and SantaMaria[30], where:

$$BW_\rho = \frac{M_\rho^2}{(M_\rho^2 - q^2) - i\sqrt{q^2}\Gamma_\rho(q^2)}, \quad (\text{III.2})$$

represents the Breit-wigner function associated with the  $\rho$  resonance lineshape, with  $M_\rho$  and  $\Gamma_\rho(q^2)$  denoting the  $\rho$  meson mass and  $q^2$  dependent total decay width. The assumed form for the latter is described below,

$$\Gamma_\rho(q^2) = \Gamma_\rho \frac{M_\rho^2 p_\pi^3}{q^2 p_0^3}, \quad (\text{III.3})$$

where

$$p_\pi = \frac{1}{2} \sqrt{q^2 - 4m_\pi^2}, \quad (\text{III.4})$$

with

$$p_0 = \frac{1}{2} \sqrt{M_\rho^2 - 4m_\pi^2}. \quad (\text{III.5})$$

## 2 The Model of Gounaris and Sakurai

Many authors and analysis have been using Gounaris and Sakurai[31] to parameterize  $e^+e^- \rightarrow \pi^+\pi^-$  spectrum. This model is using the form for  $F_\pi$  which is derived from an effective range formula for the P-wave  $\pi - \pi$  scattering phase shift, assuming  $\rho(770)$  meson dominance

$$F_\pi^{I=1}(q^2) = \frac{M_\rho^2 + M_\rho\Gamma_\rho d}{(M_\rho^2 - q^2) + f(q^2) - i\sqrt{q^2}\Gamma_\rho(q^2)}, \quad (\text{III.6})$$

$d$  is defined as

$$d = \frac{3m_\pi^2}{\pi p_0^2} \ln \frac{M_\rho + 2p_0}{2m_\pi} + \frac{M_\rho}{2\pi p_0} - \frac{m_\pi^2 M_\rho}{\pi p_0^3}, \quad (\text{III.7})$$

$f(q^2)$  is defined as

$$f(q^2) = \frac{\Gamma_\rho M_\rho^2}{p_0^3} \left[ p_\pi^2(q^2)[h(q^2) - h(M_\rho^2)] - p_0^2(q^2 - M_\rho^2), \frac{dh}{dq^2} \Big|_{q^2=M_\rho^2} \right], \quad (\text{III.8})$$

with  $h(q^2)$  is defined as

$$h(q^2) = \frac{2p_\pi(q^2)}{\pi\sqrt{q^2}} \ln \frac{\sqrt{q^2} + 2p_\pi(q^2)}{2m_\pi}, \quad (\text{III.9})$$

and

$$\frac{dh}{dq^2} \Big|_{q^2=M_\rho^2} = h(M_\rho^2) \left[ \frac{1}{8p_0} - \frac{1}{2M_\rho^2} \right] + \frac{1}{2\pi M_\rho^2}. \quad (\text{III.10})$$

## CHAPTER IV

### THE BABAR EXPERIMENT

The PEP-II used to collide high energy electron( $e^-$ ) and positron( $e^+$ ), described in the first section of this chapter, is an asymmetric  $e^+e^-$  collider operating at the  $\Upsilon(4S)$  resonance. Together with the BABAR detector, described in the second part of this chapter, it is also called a *B-meson factory* since the  $\Upsilon(4S)$  decays to more than 96% into B-mesons. But the multi functional design of the detector allows a large number of measurement in  $\tau$  physics.

The experimental facilities are located within the Stanford Linear Accelerator Center (SLAC) at Menlo Park near San Francisco, CA, USA.

#### 1 The PEP-II Collider

The PEP-II collider operates at energies about 10.58 GeV in the center-of-momentum (CM) frame. The main feature of PEP-II compared to other  $e^+e^-$  colliders is the asymmetry. Electrons are accelerated in the *High Energy Ring* (HER) to energies of  $\sim 9$  GeV, positrons in the *Low Energy Ring* (LER) to energies of  $\sim 3.1$  GeV. This results in a CM system with a boost of  $\beta\gamma=0.56$ .

Fig. IV.1 shows a schematic view of the facility. The typical branching ratios are of the order of  $10^{-4}$  to  $10^{-6}$ . Thus, the collider needs to provide a very high luminosity.

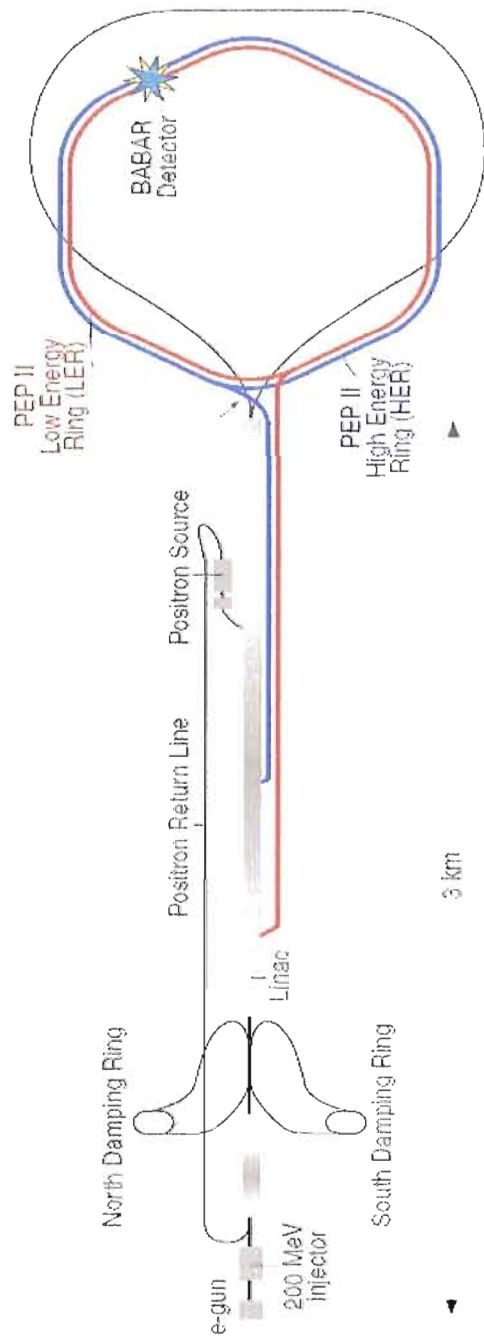


Fig. IV.1: PEP-II

The bunches collide head-on at the interaction point(IP). For each machine run, the event vertices are averaged to determine the averaged beam position, the *beam spot*. The uncertainties in the *beam spot* are of the order of a few  $\mu\text{m}$  in the transverse plane and 100  $\mu\text{m}$  along the collision axis.

The high beam currents and the large number of closely-spaced bunches required to produce the high luminosity of PEP-II tightly couple the issues of detector design(see Figure IV.2), interaction region layout, and remediation of machine-induced background. The bunches collide head-on and are separated magnetically in the horizontal plane by a pair of dipole magnets (B1), located at  $\pm 21$  on either side of the IP, followed by a series of offset quadrupoles. separate the beams to avoid parasitic collisions.

The low energy beam (LEB) is further deflected horizontally by passing off-axis through the first quadrupole pair (Q1). Beyond Q1 the beams have separate beam pipes and focussing magnets with a field-free slots for the other beam. The Q2 quadrupoles focus the LER horizontally, while Q4/Q5 focus the high energy beam (HER). The tapered B1 dipoles, located at  $\pm 21$  cm on either side of the IP, and the Q1 quadrupoles are permanent magnets made of samarium-cobalt placed inside the field of the BABAR solenoid, while the Q2, Q4, and Q5 quadrupoles, located outside or in the fringe field of the solenoid, are standard iron magnets. The collision axis is off-set from the  $z$ -axis of the BABAR detector by about 20 mrad in the horizontal plane to minimize the perturbation of the beams by the solenoid field.

The interaction region is enclosed by a water-cooled beam pipe of 27.9 mm outer radius, composed of two layers of beryllium (0.83 mm and 0.53 mm thick) with a 1.48 mm water channel between them. To attenuate synchrotron radiation, the inner surface of the pipe is coated with a 4  $\mu\text{m}$  thin layer of gold. In addition, the beam pipe is wrapped with 150  $\mu\text{m}$  of tantalum foil on either side of the IP, beyond  $z =$

+10.1 cm and  $z = -7.9$  cm. The total thickness of the central beam pipe section at normal incidence corresponds to 1.06 % of a radiation length.

The beam pipe, the permanent magnets, and the SVT(see subsection 2.1 in this Chapter) were assembled and aligned, and then enclosed in a 4.5 m-long support tube which spans the IP. The central section of this tube was fabricated from a carbon-fiber epoxy composite with a thickness of 0.79 % of a radiation length.

## 2 The BABAR Detector

The components of the BABAR detector are arranged radially. The tracking consists of a silicon vertex detector (SVT) and a drift chamber (DCH). The SVT is located close to the beam pipe surrounded by the second tracking device, the DCH. The next component is the Detector of Internally Reflected Cherenkov Light (DIRC) which is mainly used to identify pions and kaons. Its photon detection system is located at the backward end of the BaBar detector. The Electromagnetic Calorimeter (EMC) is a crystal calorimeter with a forward endcap. It is the last sub-detector within the super-conducting magnet coil which provides a 1.5 T magnetic field. The Instrumented Flux Return (IFR) is the outermost component. Figure IV.2 shows a longitudinal section through the detector center, and Figure IV.3 shows an end view with the principal dimensions.

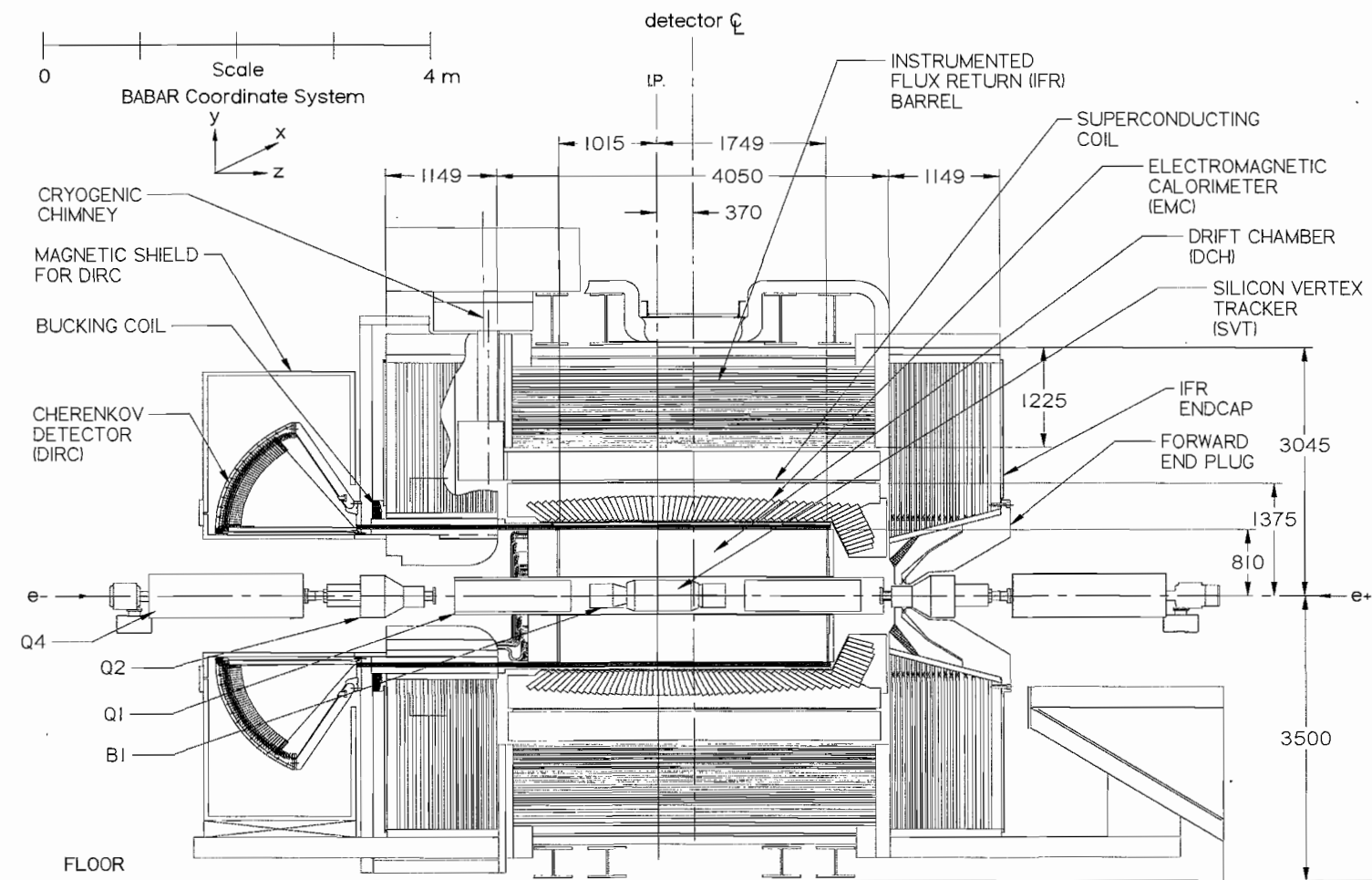


Fig. IV.2: BABAR Detector. The detector is designed according to the boosted CM system. The interaction point is not at the geometrical center of the detector. It is shifted towards the backward direction which is defined by the outgoing low energy beam.

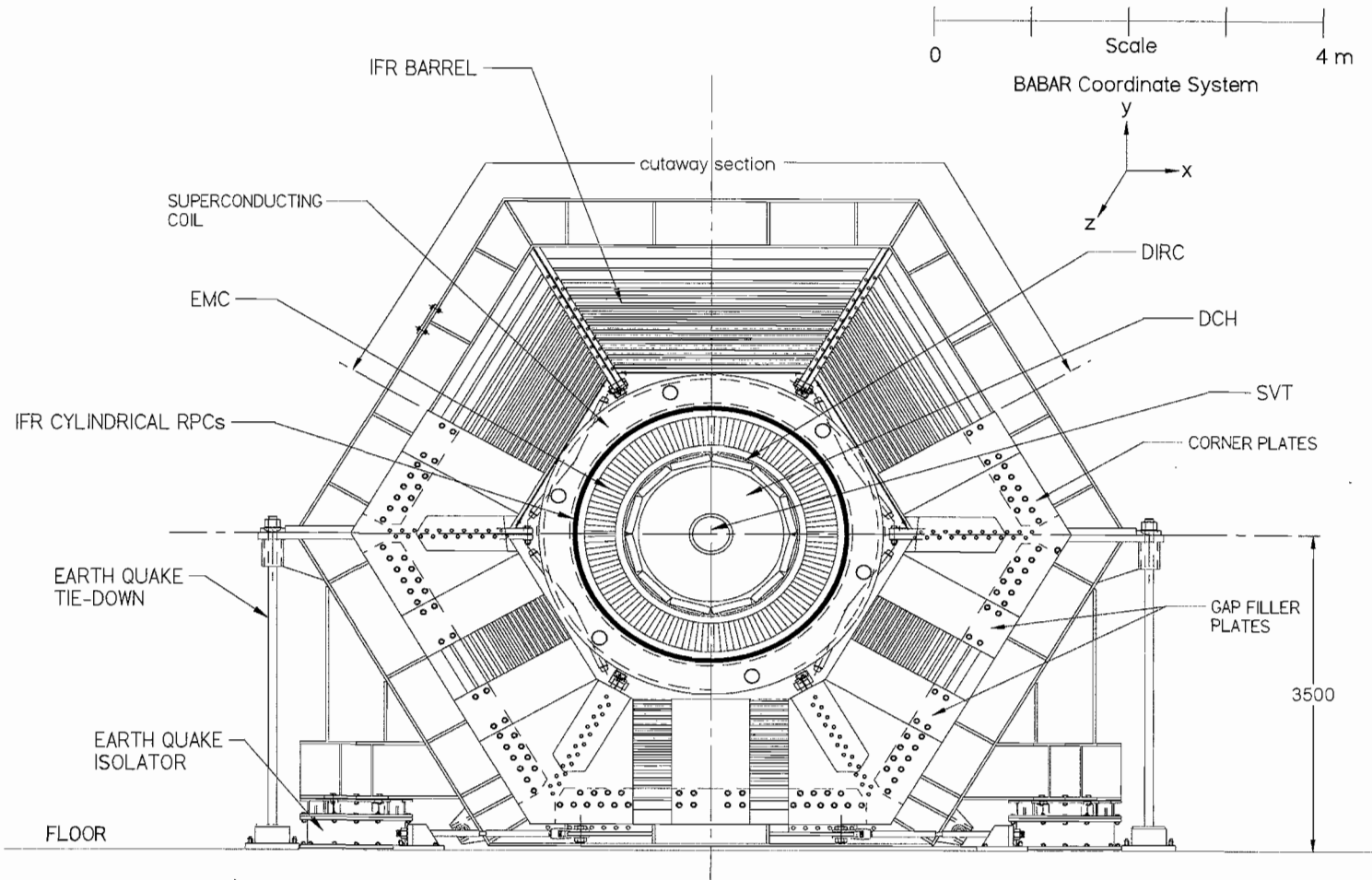


Fig. IV.3: BABAR detector end view.

## 2.1 Silicon Vertex Tracker

The silicon vertex tracker (SVT), as shown in Figure IV.4, is a part of the tracking devices of the detector. It is built from cylindrical layers of double sided silicon micro strip detectors.

The SVT covers the polar angle region from  $20^\circ$  to  $150^\circ$ . The three inner layers are critical for the measurement of the secondary vertices for the B-meson decays. The two outer layers are important for the pattern recognition and the low  $p_t$  tracking. The arrangement of the strip sensors along the beam direction as well as perpendicular to it allows the spatial measurement of the track directions and angles with a high resolution.

The SVT is especially optimized for excellent vertex resolution and reaches a precision of approximately  $70 \mu\text{m}$  for a fully reconstructed B-meson decay.

## 2.2 Drift Chamber

The drift chamber (DCH) measures the tracks of charged particles and their momenta. Additionally, the specific energy loss by ionization can be determined and contributes up to momenta of 700 MeV/c to the particle identification. The DCH complements the measurement of impact parameter and the directions of charged particles provided by the SVT near Interaction Point(IP). A side view is shown in Figure IV.5

The DCH is a multi-wire chamber with an inner radius of 26.6 cm and an outer radius of 80.9 cm and a length of 280 cm. It is composed of 40 layers with small hexagonal cells. In 24 of the layers, the wires are placed at small angles with respect to the z-axis. This provides longitudinal position information. The drift gas is a mixture of helium and iso-butane in a ratio of 80:20.

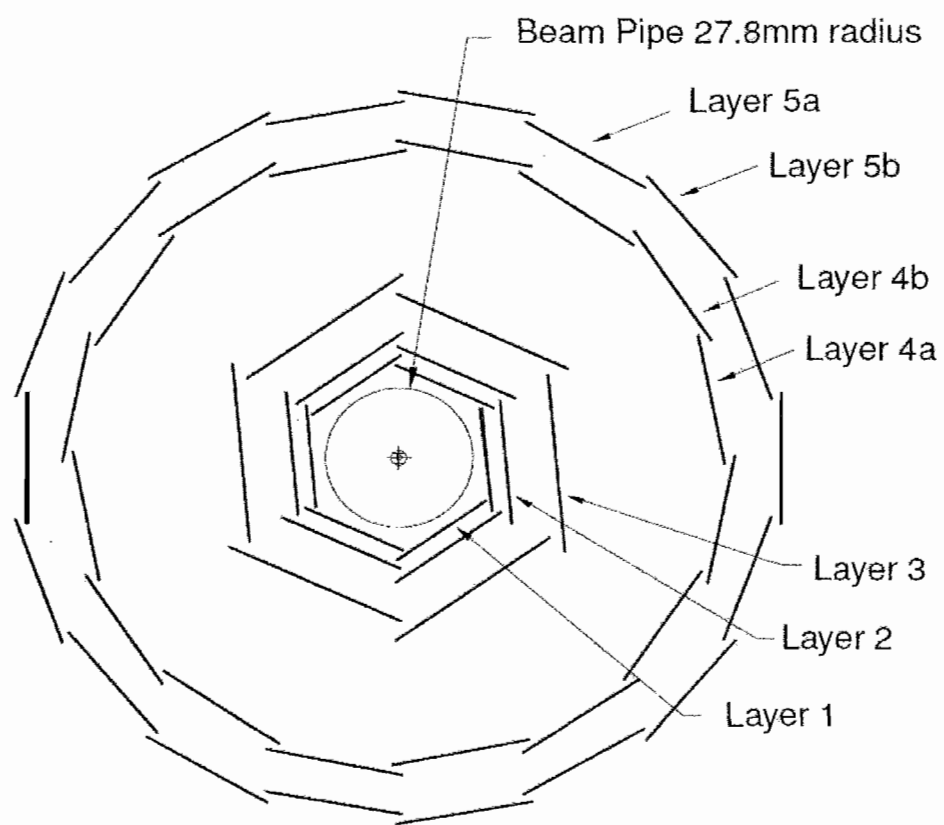


Fig. IV.4: Transverse section of Silicon Vertex Tracker(SVT).

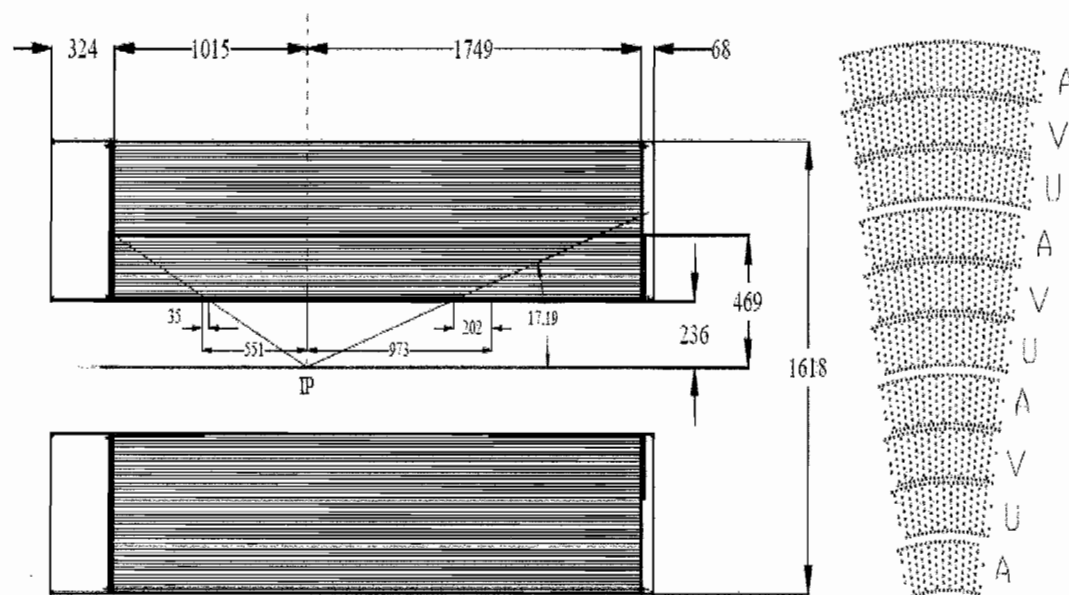


Fig. IV.5: The plot of longitudinal section of Drift Chamber(DCH). The chamber is offset by 370 mm from the interaction point(IP)

The reconstruction of tracks is done with a Kalman filter which considers data from the SVT and the DCH as well as the detector material and magnetic field. The average resolution for single tracks is given as  $125 \mu\text{m}$ .

Schematic view of the drift chamber. The center of the chamber has an offset of 370 mm from the IP. The pattern of axial (A) and stereo (U,V) layers is shown in the right hand side of Figure IV.5.

### 2.3 Cherenkov Detector

The detector for internally reflected Cherenkov light (DIRC), shown in Figure IV.6 is the most important particle identification device of the BABAR detector. It is used to separate pions and kaons from  $\tau$  and B decays. The  $\pi/\text{K}$  separation is possible up to momenta of 4 GeV with a significance of  $2.5\sigma$ .

The active detector material of the DIRC is constructed of 144 bars of fused silica arranged in bar boxes in a polygonal barrel. The DIRC bars are used both as radiators and as light pipes. Charged particles which traverse the DIRC-bars emit Cherenkov light in the angle  $\theta_C$  with respect to the direction of the particle track,

$$\cos\theta_C = \frac{1}{\beta n} = \frac{\sqrt{1 + (m/p)^2}}{n}, \quad (\text{IV.1})$$

where m and p are mass and momentum of the particle respectively and  $n=1.453$  is the refractive index of the synthetic quartz medium. The photons are reflected many times until they reach the *stand off box*, a tank of purified water. 10572 photomultiplier tubes(PMT) cover the inside of the surface of the standoff box, where fractions of the Cherenkov rings are projected.

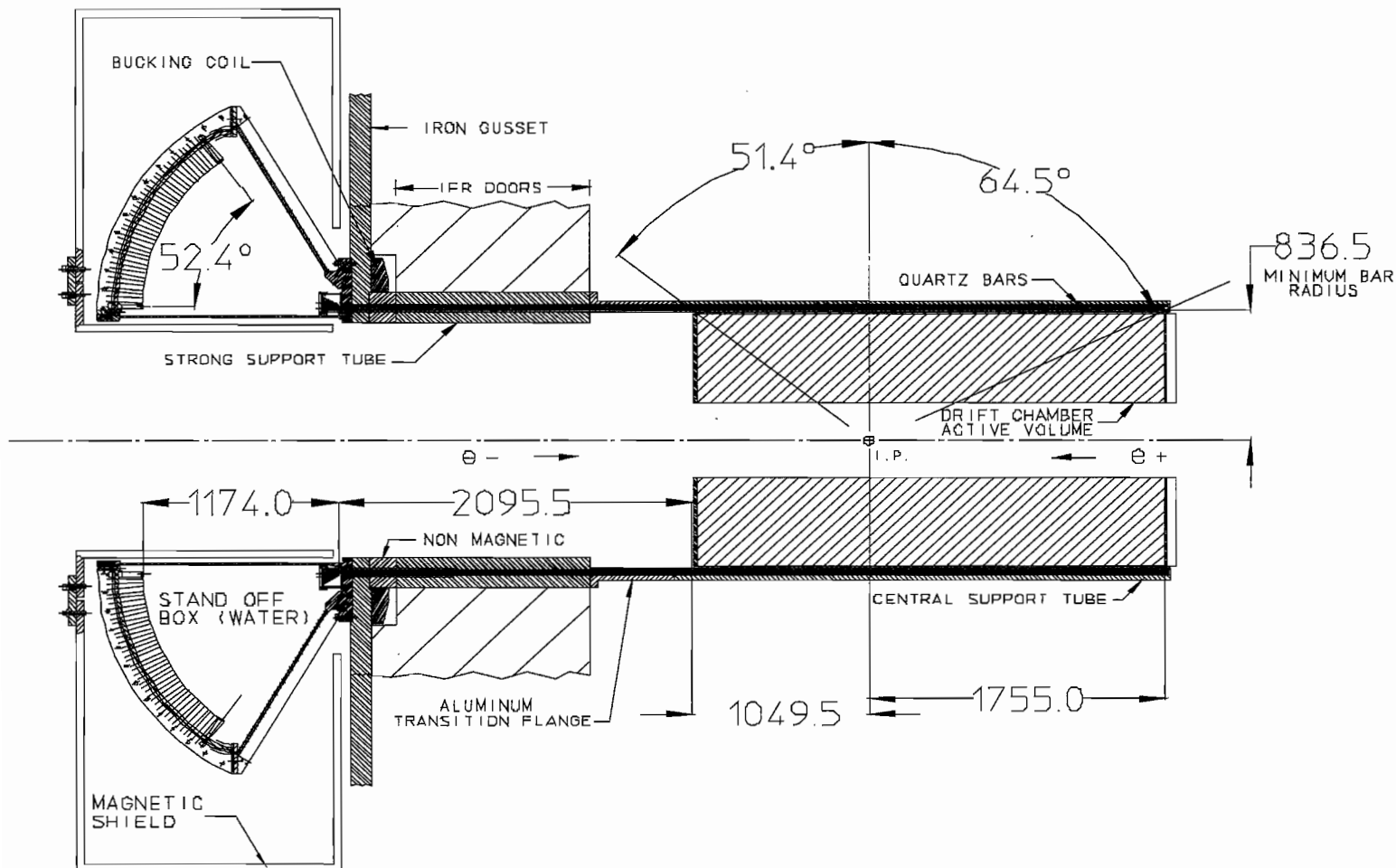


Fig. IV.6: The detector for internally reflected Cherenkov light(DIRC). The Cherenkov light is internally reflected until it gets detected in the water-filled readout reservoir.

## 2.4 Magnet Coil

All sub detector components are inside a toroidal super conducting magnet coil to allow momentum measurement from track curvature. The BABAR magnet creates a 1.5 T magnetic field parallel to the beam axis.

## 2.5 Electromagnetic Calorimeter

### Purpose and Layout

The electromagnetic calorimeter (EMC) is designed to measure the energy, the position and the transverse shape of showers with excellent efficiency. It is designed to detect electrons and photons over the energy range of 20 MeV to 9 GeV with high resolution. This allows the detection of photons from  $\pi^0$  and  $\eta$  decays as well as from QED and radiative processes. Besides that, the EMC contributes via  $E/p$  measurements to the electron identification for flavor tagging of neutral B-mesons and via the shower shape analysis to the identification of neutral hadrons. Furthermore, the EMC has to be compatible with the 1.5 T field of the solenoid and operate reliably over the anticipated 10-year lifetime of the experiment. The longitudinal cross section is shown in Figure IV.7.

To achieve these goals, a hermetic, total absorption calorimeter composed of thallium doped cesium iodite crystals ( $\text{CsI}(\text{Tl})$ ) was chosen. The main advantages are a very high light yield and good radiation hardness. This permits the use of silicon photodiodes which operate reliably in magnetic fields for the readout of the scintillation light. Another advantage of  $\text{CsI}(\text{Tl})$  crystals is the small Moliere Radius ( $R_M = 3.8$  cm) and the short radiation length ( $X_0 = 1.85$  cm) which allows a compact detector design for the measurement of fully contained showers.

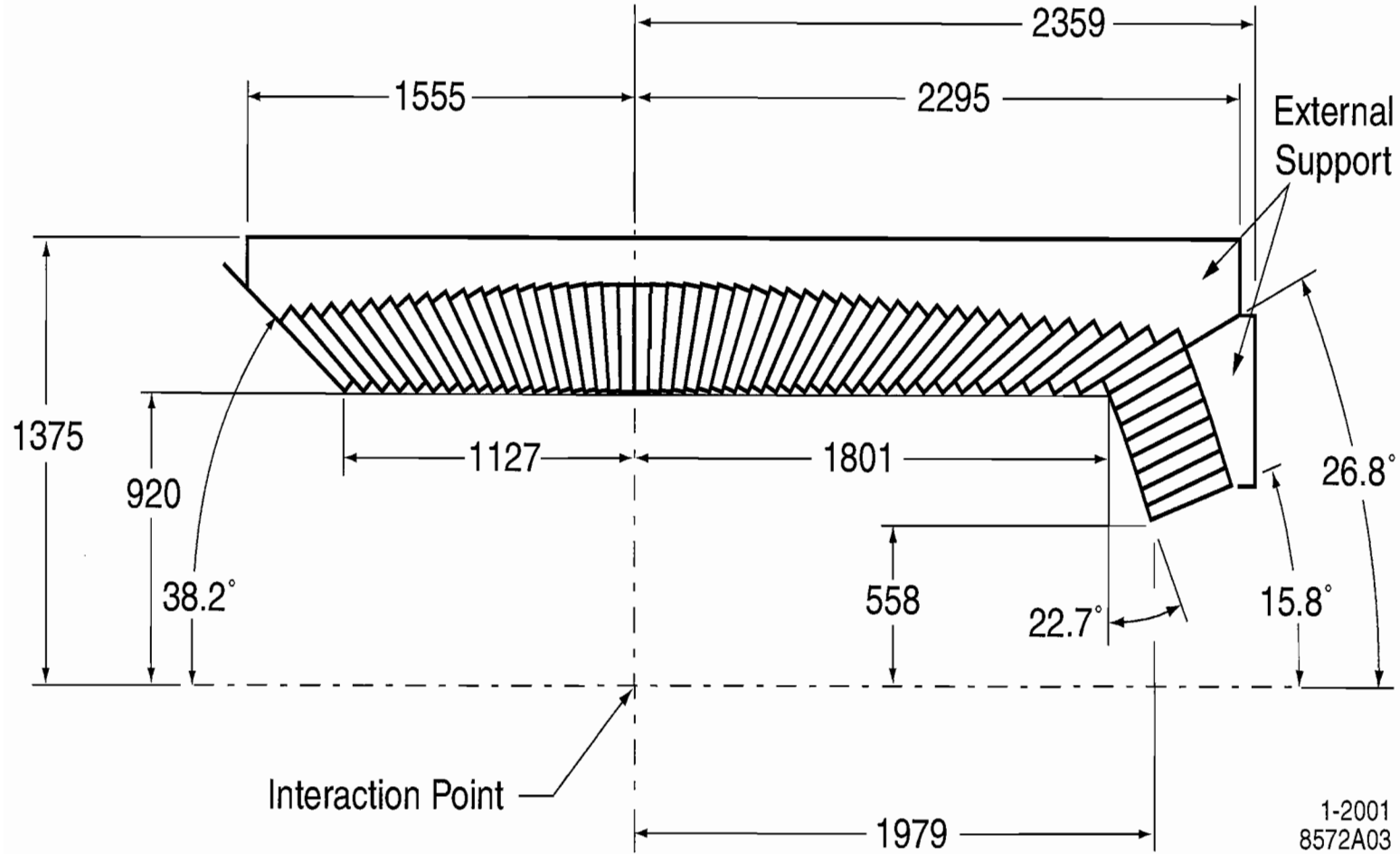


Fig. IV.7: The longitudinal view of the Electromagnetic Calorimeter(only the top half is shown) indicating arrangement of the 56 crystal rings. The detector is axially symmetric around  $z$ -axis. All number are given in milimeter

The energy resolution of a calorimeter as a function of energy can be parameterized to consist of two parts which are added quadratically: A constant part to which electronics nonlinearities and non-uniformities are contributing as well as calibration errors. The second, energy dependent part has a statistical nature since the basic processes in an electromagnetic shower are statistical processes as fluctuations in photon statistics, electronic noise and beam generated background. In crystal calorimeters, the energy dependent part of the resolution is assumed to be proportional to  $1/\sqrt[4]{E}$  due to photon statistics. The target energy resolution of the BABAR EMC was

$$\frac{\sigma_E}{E} = \frac{1\%}{\sqrt[4]{E(GeV)}} \oplus 1.2\%, \quad (\text{IV.2})$$

where both terms are added in quadrature.

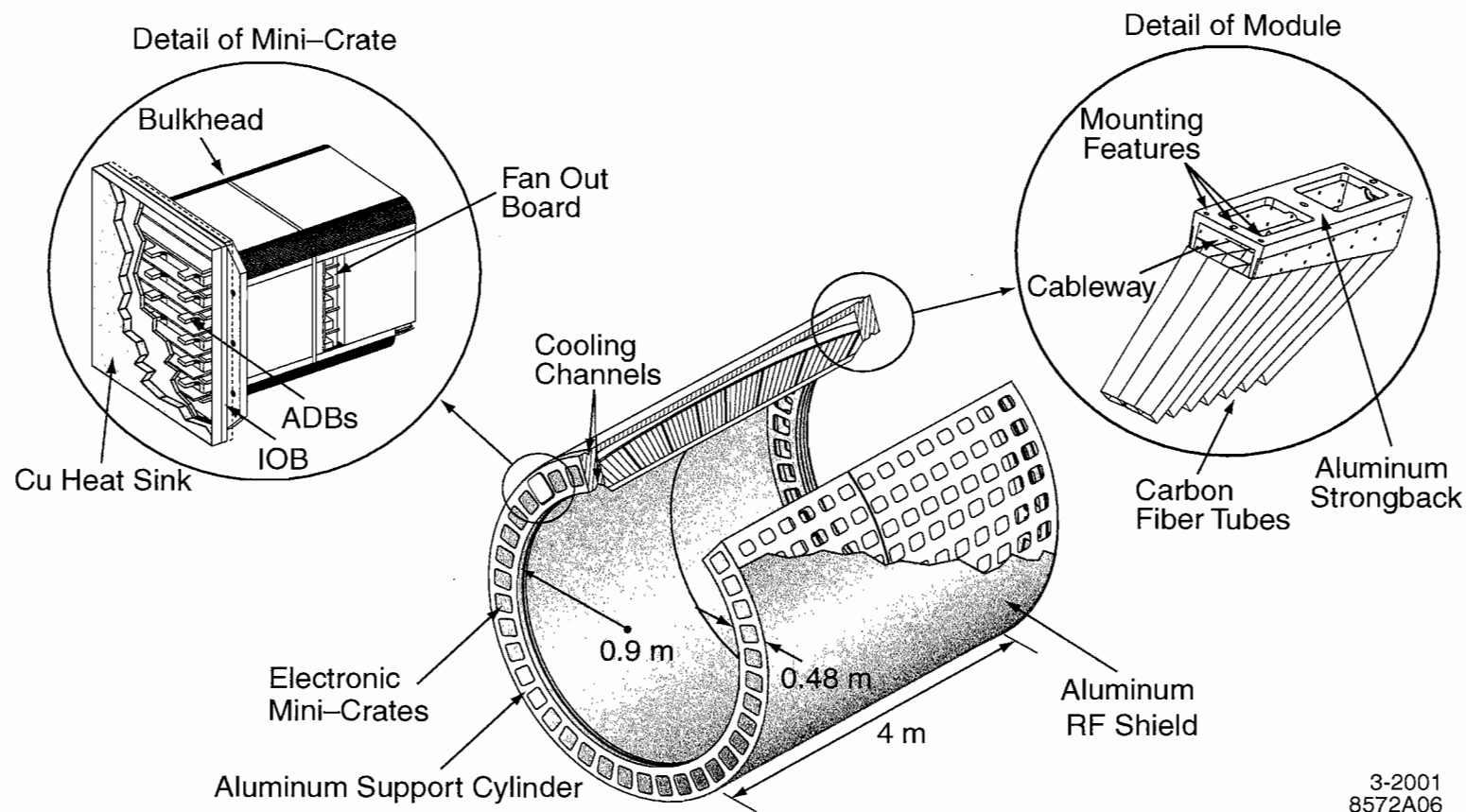
The angular resolution is determined by the transverse crystal size and the average distance to the interaction point. The target was to achieve

$$\sigma_\theta = \sigma_\phi = \left( \frac{3}{\sqrt{E(GeV)}} + 2 \right) \text{ mrad} \quad (\text{IV.3})$$

at  $90^\circ$  incident angle to the beam direction.

## Geometry

The EMC consists of a cylindrical barrel and a conical forward endcap. It has full coverage in azimuth and extends in polar angle from  $15.8^\circ$  to  $141.8^\circ$  corresponding to a solid angle coverage of 90% in the CM system. The barrel part consists of 5760 crystals which are ordered cylindrical around the beam axis. The radial distance from the interaction point to the crystal front face is 92 cm. Along the polar angle, the barrel is divided in 48 crystal rings. A longitudinal view along the polar angle is



3-2001  
8572A06

Fig. IV.8: The Electromagnetic Calorimeter(EMC) barrel support structure, with great details on the modules and electronic crates

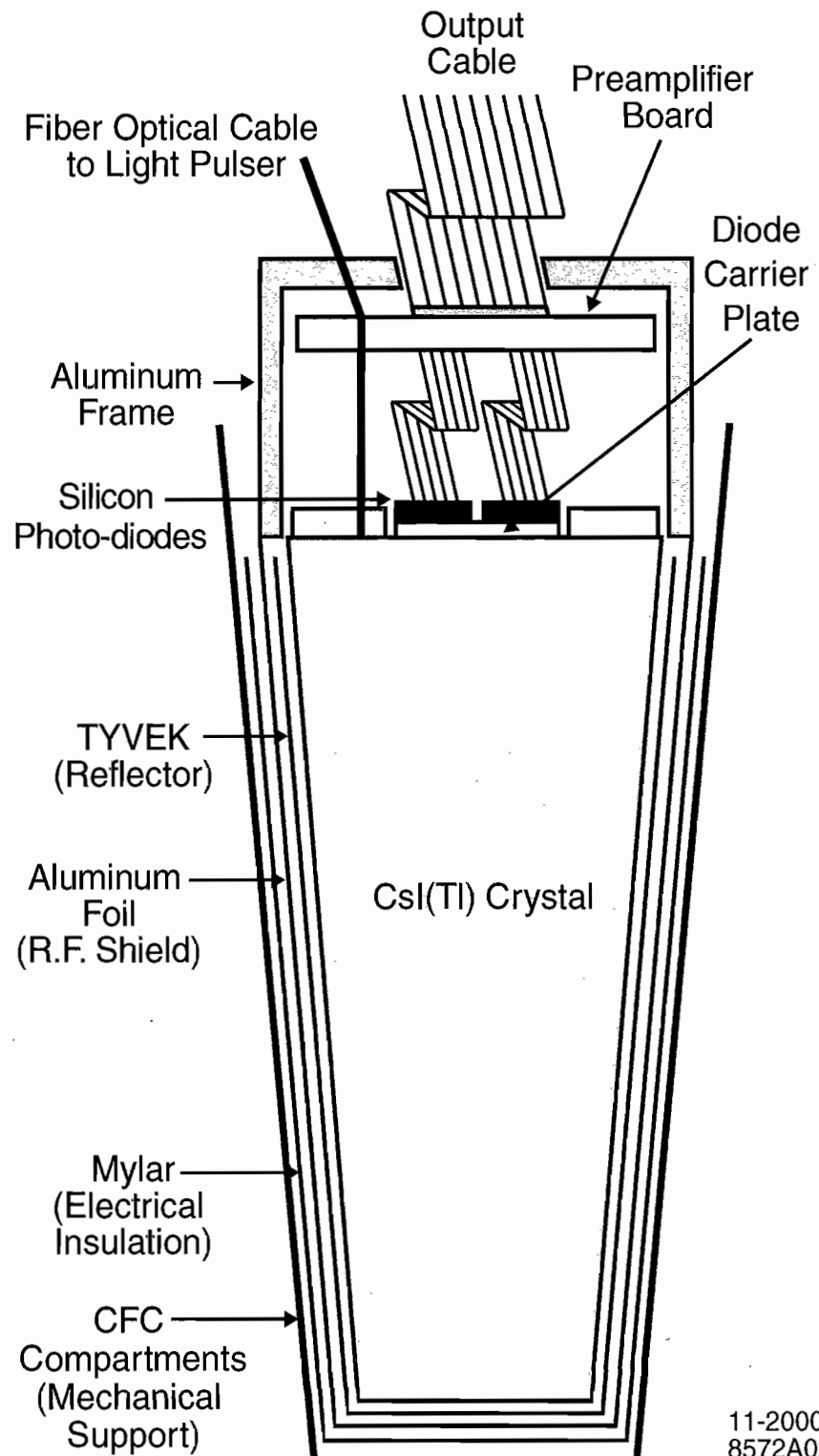


Fig. IV.9: The plot of one wrapped CsI(Tl) Crystal and the front-end readout package mounted on the rear face.

shown in Figure IV.7 along the azimuthal angle, 120 crystals are segmented. Each crystal is wrapped in aluminum and mylar foils. Thus, between two crystals is about  $130 \mu\text{m}$  of dead material. The crystals are ordered into *modules* of  $7 \cdot 3 (\theta \cdot \phi)$  crystals. Those modules are wrapped with carbon fiber tubes, in-between two modules is on average 1.3 mm of material. The modules are bonded to an aluminum strong-back that is mounted on the external support. By supporting the modules at the back, the material in front of the EMC is kept to a minimum. A schematic view of the cylindrical barrel and the assembly of a module is shown in Figure IV.8.

The endcap covers the forward area of the calorimeter. It consists of 820 crystals which are ordered circularly. The eight rings in the polar angle consist of 80 (the innermost two rings), 100 (the next three rings) and 120 (outer three rings) crystals respectively.

All crystals point with their front face to the interaction point. In order to minimize losses in-between the crystals, a small non-projectivity is added in the polar angle. The average size of this non-projectivity is 1.4 mrad.

The crystals are numbered with an index  $I_\theta$  which in the polar angle,

$$1 \leq I_\theta \leq 56, \quad (\text{IV.4})$$

where  $I_\theta = 1$  is the very forward part of the endcap, the barrel part begins with  $I_\theta = 9$  and the very backward part of the barrel is  $I_\theta = 56$ . In the azimuthal angle,

$$0 \leq I_\phi \leq 79/99/119 \text{ depending on } I_\theta. \quad (\text{IV.5})$$

The material in-front of the EMC was minimized, depending on the polar angle 0.3-0.6  $X_0$  of dead material are between the interaction point and the EMC. In front of the first 3 rings in the endcap are about 3  $X_0$  of support structure.

## Reconstruction of Clusters and Bumps

A particle which enters the EMC deposits, in general, energy in several crystals. Such a group of crystals is called a cluster. The following algorithm is used to reconstruct clusters from the information of individual crystals:

1. The crystal with the highest energy of the cluster is called the *seed*. It is required to have more than 5 MeV.
2. All adjacent crystals with energies above 1 MeV are added to the cluster.
3. The neighbors of each crystal with more than 3 MeV are added to the cluster if their energy exceeds 1 MeV
4. The cluster energy is defined as the sum of the energy of all associated crystals.  
The cluster energy is required to be more than 20 MeV in total for the cluster to be accepted.

If two particles enter the calorimeter close to each other, it is possible that the energy deposition takes place in one cluster with two local maxima. In this case the cluster is splitted according to the weights of its single crystal information into *bumps* with only one maximum each. The energy and the position of the *bump* is associated to one single particle.

## Energy Calibration of the Calorimeter

The calibration of the BABAR calorimeter is performed in three steps:

1. Electronics Calibration

The electronics calibration corrects the pedestal offsets, determines the overall gain and removes non-linearities.

## 2. Single Crystal Calibration

In this calibration step, the measured pulse height in a single crystal is assigned to an energy. It also corrects variations in the light yield from crystal to crystal and over time. The time dependence is mainly due to radiation damage.

## 3. Cluster Calibration

In the cluster energy calibration, energy losses which are not due to the features of a single crystal are corrected. These energy losses are due to interactions in front of the EMC, leakage behind the EMC and energy loss in dead material in-between the crystals.

The three steps of the energy calibration of the EMC are discussed in more detail in the following:

## Electronics Calibration

The electronics calibration is performed by precision charge injection into the preamplifier input. Initially up to 12% non-linearity were observed. These non-linearities were traced to oscillations on the ADC cards that have since been corrected. Remaining non-linearities are of the order of 2%.

## Single Crystal Calibration

The single crystal calibration is performed for two energies at opposite ends of the dynamic range, the two measurements are combined by a logarithmic interpolation (line calibrator). For low energies, a radiative source spectrum is used ( $E_\gamma = 6.13$  MeV) whereas for high energies, electrons from Bhabha scattering are used ( $E = 3\text{-}9$  GeV).

For the radioactive source calibration, irradiated Fluorinert gets pumped through thin walled aluminum pipes which are mounted right in front of the crystals of the EMC. The Fluorinert decays via a radioactive decay chain,



under emission of a monoenergetic photon with the energy of 6.13 MeV.

The high energy single crystal calibration factors are determined from electrons from Bhabha scattering

$$e^+ e^- \rightarrow e^+ e^-, \quad (\text{IV.9})$$

The deposited energy  $E_{dep}^k$  of a final state electron  $k$  is purely determined by the angle  $\theta_{lab}$  between  $e^+$  and  $e^-$ ,

$$E_{dep}^k(\theta) = \frac{E_{tot}^2 - \vec{P}_{tot}^2}{2(E_{tot} - |P_{tot}| \cos \theta_{lab})}, \quad (\text{IV.10})$$

where  $E_{tot}$ ,  $P_{tot}$  are the total energy and momentum in the laboratory system, respectively. The energy deposited in each individual crystal is compared to a prediction derived in a MC simulation. This means that not only the single crystal calibration factor can be determined, but also slight differences between data and simulation of the crystals are taken out. A more detailed description of the sophisticated algorithm can be found in

The crystal response with electronics calibration and single crystal calibration applied is called  $e_i$ . The raw cluster energy,  $E_{raw}$ , is defined as the sum of the single

crystal calibrated energies  $e_i$ ,

$$E_{raw} = \sum_i e_i, \quad (\text{IV.11})$$

where  $i$  is enumerating all crystals in the respective cluster.

## Cluster Calibration

The cluster energy calibration corrects for energy loss due to shower leakage, dead material in front of the calorimeter and in-between the crystals. The true energy of a photon can be expressed as

$$\text{photon energy} = \text{deposited energy} + \text{energy losses}. \quad (\text{IV.12})$$

The cluster calibration is obtained as a correction function  $c(E, \theta)$  which depends on the polar angle  $\theta$  and the energy,

$$E_{cal} = E_{raw} \cdot c(E, \theta), \quad (\text{IV.13})$$

where  $E_{cal}$  is the cluster calibrated energy,  $E_{raw}$  the raw energy as defined in Eq. and  $c(E, \theta)$  is the calibration function.

## On Simulation

The processes of energy loss in dead material are included in the simulation. The generated energy describes therefore the single crystal energy  $e_i$ . The raw cluster energy is obtained from the generated single crystal energies. In order to have the cluster energy in the simulation at the right scale, the raw energy has to be corrected for these simulated energy losses. This is called *MC calibration*. Since  $E_{true}$  is known

from the generator,  $c_{MC}(E, \theta)$  can easily be determined

$$c_{MC}(E, \theta) = \frac{E_{true}^{MC}}{E_{raw}^{MC}}. \quad (\text{IV.14})$$

## On Data

For data, the situation is more complicated. It is necessary to find a physics process which provides photons with known energies. Currently, the only mechanism which is exploited is the decay . The reconstructed two photon mass is known to be

$$m_{\gamma\gamma} = \sqrt{2E_{\gamma 1}E_{\gamma 2}(1 - \cos\alpha)} = 135.0 \text{ MeV}, \quad (\text{IV.15})$$

where  $E_\gamma$  is the photon energy and  $\alpha$  the opening angle between the two photons. This process produces clusters with an energy up to 1.5 GeV in the laboratory frame . At higher energies, the two photons are merged to one cluster and the reconstruction of neutral pions becomes difficult.

## 2.6 Instrumented Flux Return

The Instrumented Flux Return (IFR) was designed to identify muons with high efficiency and good purity, and to detect neutral hadrons (primarily  $K_L$  and neutrons) over a wide range of momenta and angles. IFR is very important for studying the decays of  $e^+e^- \rightarrow \mu^+\mu^-\gamma$  that will be used to assign some systematic uncertainties in this analysis.

The principal requirements for IFR are large solid angle coverage, good efficiency, and high background rejection for muons down to momenta below 1 GeV/c. For neutral hadrons, high efficiency and good angular resolution are most important.

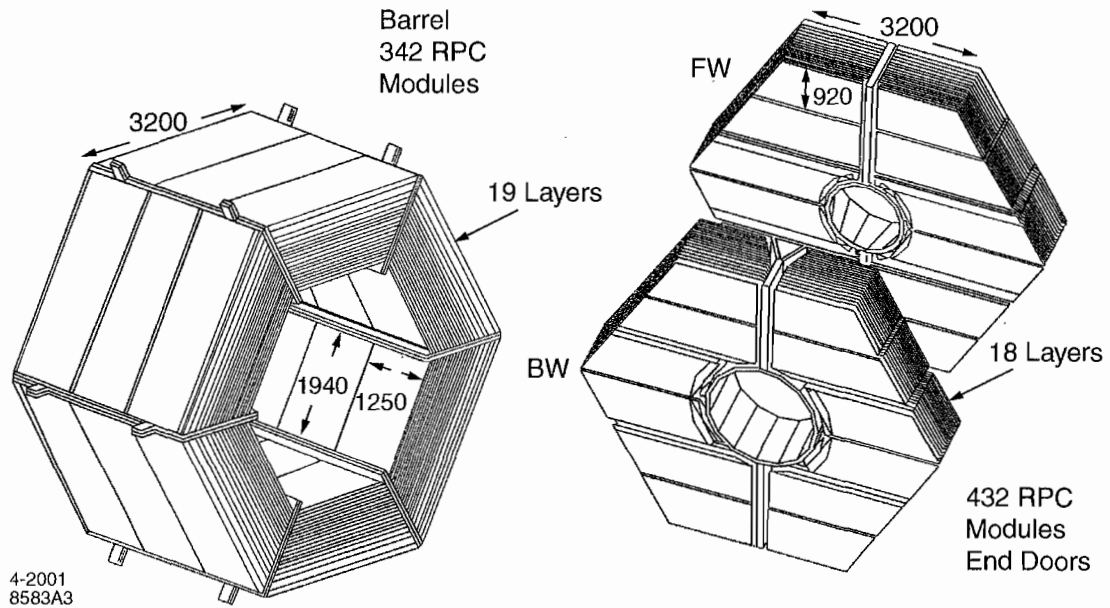


Fig. IV.10: Overview of the IFR: Barrel sectors and forward (FW) and backward (BW) end doors; the shape of the RPC modules and their dimensions are indicated.

Because this system is very large and difficult to access, high reliability and extensive monitoring of the detector performance and the associated electronics plus the voltage distribution are required.

The IFR uses the steel flux return of the magnet as muon filter and hadron absorber. Single gap resistive plate chambers with two-coordinate readout have been chosen as detectors.

The RPCs are installed in the gaps of the finely segmented steel of the barrel and the end doors of the flux return, as illustrated in Figure IV.10. The steel segmentation has been optimized on the basis of Monte Carlo studies of muon penetration and charged and neutral hadron interactions. The steel is segmented into 18 plates, increasing in thickness from 2 cm of the inner nine plates to 10 cm of the outermost plate.

The RPCs are inserted into the gaps between these plates in the six barrel sector and the two end doors, as illustrated in Figure IV.10. The nominal gap between the

steel plates is 3.5 cm in the inner layers of the barrel and 3.2 cm elsewhere. There are 19 RPC layers in the barrel and 18 in the endcaps. In addition, two layers of cylindrical RPCs are installed between the EMC and the magnet cryostat to detect particles exiting the EMC.

RPCs detect streamers from ionizing particles via capacitive readout strips. They offer several advantages: simple, low cost construction and the possibility of covering odd shapes with minimum dead space. Further benefits are large signals and fast response allowing for simple and robust front-end electronics and good time resolution, typically 1-2 ns. The position resolution depends on the segmentation of the readout: a few mm are achievable.

## 2.7 Trigger

The BABAR trigger is useful for selecting interesting physics events, which will subsequently be processed and written to the datastore. If competitive physics measurements are to be made, it is essential that a high efficiency is achieved and that this efficiency is well understood. The BABAR trigger consists of two levels. The Level1/L1 (hardware) trigger is designed to select candidate physics events at a rate of no more than 2 kHz, the maximum rate allowed by the data acquisition system. The Level3/L3 (software) trigger uses more complex algorithms (after event construction) to reduce the event rate to about 200 Hz, the maximum rate that the event processing farm and mass storage facility can tolerate.

### L1

The Level-1 trigger consists of the drift chamber trigger (DCT), calorimeter trigger (EMT) and global trigger (GLT). The DCT and EMT construct 'primitive objects'

which are then combined by the GLT to produce a whole range of 'trigger lines'. A L1 accept is generated if a GLT trigger line is active for a particular beam crossing. This accept signal must be distributed to the sub-system data acquisition systems with a latency of no more than 12 s. The main DCT primitive objects are short and long tracks, corresponding to tracks with a transverse momentum, 120 MeV/c and 180 MeV/c respectively. In the case of the EMT, the basic trigger object is a tower, corresponding to three adjacent rows of crystals along the length of the calorimeter.

To allow cross-calibration of efficiencies for the EMT and DCT, the L1 trigger system is designed to be able to trigger independently from pure DCT and EMT triggers for most physics channels. Tau and two-photon events are the exception, and rely mainly on DCT triggers. In order to keep the L1 trigger rate at a practical level, it is necessary to prescale some of the GLT trigger lines. The pre-scale factor determines what fraction of the accepts for a particular trigger line are logged, ensuring that processes with large cross sections, such as Bhabhas, do not dominate the data.

### L3

The L3 trigger consists of a set of software algorithms designed to reduce backgrounds while retaining physics events. In order to achieve the reduction in rate, the Level 3 algorithms use complete events rather than the elementary trigger objects constructed at the hardware level (Level 1) of the trigger. The rates of all other physics process amount to only about 200 Hz.

The L3 trigger software comprises event reconstruction and classification, a set of event selection filters, and monitoring. This software runs on the online computer farm. The filters have access to the complete event data for making their decision, including the output of the L1 trigger processors and Fast Control and Timing Sys-

tem(FCTS) trigger scalers. L3 operates by refining and augmenting the selection methods used in L1. For example, better DCH tracking (vertex resolution) and EMC clustering filters allow for greater rejection of beam backgrounds and Bhabha events.

The L3 system runs within the Online Event Processing (OEP) framework. OEP delivers events to L3, then prescales and logs those which pass the L3 selection criteria.

To provide optimum flexibility under different running conditions, L3 is designed according to a general logic model that can be configured to support an unlimited variety of event selection mechanisms. This provides for a number of different, independent classification tests, called *scripts*, that are executed independently, together with a mechanism for combining these tests into the final set of classification decisions..

The L3 trigger has three phases. In the first phase, events are classified by defining L3 input lines, which are based on a logical OR of any number of the 32 FCTS output lines. Any number of L3 input lines may be defined. The second phase comprises a number of scripts. Each script executes if its single L3 input line is true and subsequently produces a single pass-fail output flag. Internally, a script may execute one or both of the DCH or EMC algorithms, followed by one or more filters. The algorithms construct quantities of interest, while the filters determine whether or not those quantities satisfy the specific selection criteria. In the final phase, the L3 output lines are formed. Each output line is defined as the logical OR of selected script flags. L3 can treat script flags as vetoes, thereby rejecting, for example, carefully selected Bhabha events which might otherwise satisfy the selection criteria.

L3 utilizes the standard event data analysis framework and depends crucially on several of its aspects. Any code in the form of *modules* can be included and configured at run time. A sequence of these software modules compose a script. The same instance of a module may be included in multiple scripts yet it is executed only once, thus avoiding significant additional CPU overhead.

### 3 Offline Data Processing

Events which are selected by the L3 trigger are stored for further processing. These events are grouped into *runs*. The full set of detector signals for a run of events is written to a single data file, usually referred to as an extended tagged container (XTC) file. The raw size of each event in the XTC is about 30 KB, and XTC files are typically a few tens of GB in size.

#### 3.1 Prompt Data Reconstruction

In recent years, the full processing of the event data has been conducted offline, meaning that the data are not fully processed in real-time (i.e. as the signals are recorded by the detector). Instead, all subsequent processing operates groups of events corresponding to one run (and one XTC file). These data are processed in a two-pass system. First, calibration conditions are calculated from a subset of the events in the run and written to the conditions database. This step is referred to as Prompt Calibration (PC). Secondly, all the events are reconstructed based on the conditions in the database, and are written out to event collections. This step is referred to as Event Reconstruction (ER).

The PC step of the data processing makes use of only a subset of the events in a run. For technical reasons, these events are also stored in a secondary data file called a *calib-XTC*. The calib-XTC file for each run is filled with events passing a particular set of L3 trigger output lines, all of which are designed to provide a constant output rate of 1 or 2 Hz, depending on the trigger line. These output lines select Bhabha events, di-muon events, cosmic muons, and low-multiplicity hadronic events. The PC processing software runs on these events and writes out a set of calibrations which give a picture of the detector conditions at the moment the events were recorded.

To better account for changing detector conditions, the PC processing software makes use of *rolling calibrations*. In this method, the calibration constants from previous runs are stored and used as additional input information for the calculation of the current run's calibrations. This method also effectively provides for larger statistics without actually increasing the sampling rate for the calibration events. When all the calibration events in a run have been processed, the results are collected and passed to a final processing module. This module calculates the final calibration constants for that run and writes them to a temporary database where they are made available for the next run. The calibration constants are also written to the main conditions database, and assigned a validity interval corresponding to the time interval over which the run was recorded. During a period of high luminosity typical of the later years of BABAR running, the PC processing step was performed on computers at SLAC, utilizing around 30 CPUs.

The Event Reconstruction step processes the full set of events in the XTC file. Because the detector has already been calibrated for the run period, the event reconstruction can process the events in any order. This task is accomplished by a farm of a few hundred multi-CPU computers at Padova, Italy, along with (more recently) a similar farm at SLAC.

The actual reconstruction of an event (both PC and ER) is done by a software application called Elf. In contrast to the trigger algorithms, this software uses the full event data to reconstruct tracks in the DCH and SVT and clusters in the EMC and IFR. Elf also creates lists of different particles by running particle identification (PID) algorithms on the reconstructed tracks for a full description of the algorithms using in the analysis). Finally, Elf fills a set of Boolean variables called *tags* which provide a way of quickly classifying events based on very general characteristics. Background filter and trigger information are also stored as tags. The charged-track

lists, neutral particle lists, PID lists, and tag variables are written out to files called event collections, which are made available for further processing and analysts' use. Simulated data are also reconstructed with Elf, but are not run through the prompt reconstruction system. The event generator software is bundled with the detector simulation software and with Elf to form one integrated production package which directly outputs events collections.

### 3.2 Data Skimming

Most physics measurements made with the BABAR data involve only a specific type of event. Often these events constitute only a small fraction of the total data set. To facilitate the many BABAR analysts, one final step of centralized data processing takes place before the typical user sees the data. Once a run is processed by the prompt reconstruction system, the output collections are *skimmed*. A *skim* refers to a subset of reconstructed events which fulfill some basic criteria. Groups of physicists working with similar analyses define a skim by choosing a simple set of criteria that selects an acceptably large fraction of the events of interest. BABAR analysts have defined hundreds of skims over the years, and some number of these skims are chosen to be calculated for the data and MC events. Using a large farm of computers at SLAC, each event in an event collection is processed and assigned a true or false value for each skim being run. A *deep-copy skim* is a physical copy of the reconstructed data for each event that passes a particular skim. A *pointer skim* is a collection of pointers to the data for event that passes the skim. Pointer skims are much smaller, but the redundant data of deep-copy skims provides better computing performance with large numbers of users.

This analysis only uses data and MC events which pass the **Tau1N** skim. This skim selects events for which the following criteria are true

- Event passes either DCH L3 trigger or EMC L3 trigger (always true for data, not necessarily true for MC).
- Event passes one or more of the following background filters: BGFMultihadron, BGFNeutralHadron, BGFTau, BGFMuMU, BGFTwoProng.
- The number of entries in the ChargedTracks list is less than eleven.
- The thrust is defined as the vector which minimizes the transverse momentum for all entries in the ChargedTracks and CalorClusterNeutral lists. The thrust axis is used to divide the event into hemispheres in the CM frame. The number of EMC clusters with energy greater than 50 MeV in each hemisphere must be less than or equal to six.
- Using tracks from the GoodTracksVeryLoose list, one hemisphere must contain one track, while the other must contain at least three.

## CHAPTER V

### DATA AND MONTE CARLO(MC)

#### 1 Data

The number of tau pairs recorded in BABAR detector is proportional to the integrated BABAR Luminosity. We use about  $297 \text{ fb}^{-1}$  DATA taken by BABAR detector from Run 1-5 (see Table V.1), which consists of  $274 \text{ fb}^{-1}$  taken at a center-of-momentum energy of  $m_{\gamma(4S)} = 10.58 \text{ GeV}$  (On-Peak DATA, because at energy 10.58 GeV, the rate of  $B\bar{B}$  is at maximum) and  $22.9 \text{ fb}^{-1}$  taken at a center-of-momentum energy of  $m_{\gamma(4S)} = 10.54 \text{ GeV}$  (Off-Peak DATA). The integrated luminosity of the data recorded by BABAR detector as a function of time can be seen in Figure V.1.

Run	On-Peak Data ( $\text{pb}^{-1}$ )	Off-Peak Data ( $\text{pb}^{-1}$ )	Total Per Run ( $\text{pb}^{-1}$ )	Begin	End
1	19908 ( $\text{pb}^{-1}$ )	2307 ( $\text{pb}^{-1}$ )	22216 ( $\text{pb}^{-1}$ )	Feb 2000	Oct 2000
2	58692 ( $\text{pb}^{-1}$ )	5401 ( $\text{pb}^{-1}$ )	64093 ( $\text{pb}^{-1}$ )	Feb 2001	Jun 2002
3	31865 ( $\text{pb}^{-1}$ )	2440 ( $\text{pb}^{-1}$ )	34305 ( $\text{pb}^{-1}$ )	Dec 2002	Jun 2003
4	96423 ( $\text{pb}^{-1}$ )	8790 ( $\text{pb}^{-1}$ )	105213 ( $\text{pb}^{-1}$ )	Sep 2003	Jul 2004
5	67120 ( $\text{pb}^{-1}$ )	3954 ( $\text{pb}^{-1}$ )	71074 ( $\text{pb}^{-1}$ )	May 2005	Mar 2006
TOTAL	274008 ( $\text{pb}^{-1}$ )	22892 ( $\text{pb}^{-1}$ )	296900 ( $\text{pb}^{-1}$ )		

Tab. V.1: DATA and MC

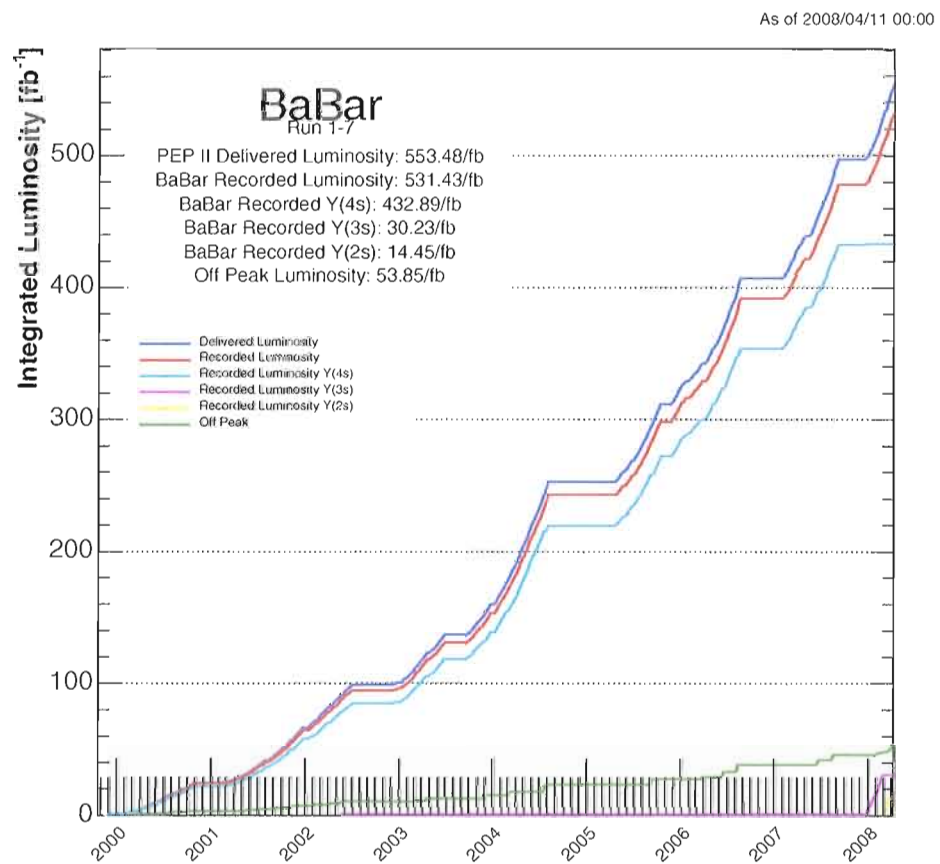


Fig. V.1: Integrated Luminosity of BABAR Detector

## 2 Monte Carlo(MC)

These simulations are very important to understand the detector response. Simulation of signal properties help one to study signal efficiency, while simulation of non-signal helps the analyst to reject and reduce background significantly. After background properties can be well simulated, they can be used to make predictions of some specific background contributions. Some backgrounds in this analysis for examples are Bhabhas, quark-antiquark and non-signal  $\tau$  decays.

To have better understanding of background, we generate significant number of Monte Carlo ntuples. Background estimations can be grouped into six classes: uds( $u\bar{u}, d\bar{d}, s\bar{s}$ ),  $b\bar{b}, c\bar{c}$  (these 3 can called  $q\bar{q}$  continuum background), Bhabha,  $\mu^+\mu^-$  and generic  $\tau^+\tau^-$ . The signal events are generated using KK2f generator[59], which simulates initial state radiation(ISR) and final state photon production more precisely than KORALB[60], while the generic  $\tau$  decays are simulated using TAUOLA[61] and radiation from final state leptons has been simulated with PHOTOS[62].

Exact process names, MC statistics used and cross sections for each process are given in Table V.2.

Special note,  $\rho''$  was not included in the simulation, so that Data and MC are not perfect match in invariant  $\pi^-\pi^0$  mass plot around  $\rho''$  peak region(1.6-1.8 GeV).

The path of simulated particles through the detector in the presence of magnetic field, their interaction with the detector material, and the response signal of the active detector. GEANT4 provides tools to construct the detector geometry, simulate the interactions and decays of each particle species and to display detector components, particle trajectories and track hits.

Sample name	MC Process name	$\sigma$ (nb)	$N_{sample}(10^6)$	$\frac{\mathcal{L}_{MC}}{\mathcal{L}_{Data}}$
$\tau\tau$	$e^+e^- \rightarrow \tau^+\tau^-$ (KK2F)	0.89	253.6	0.96
uds	$e^+e^- \rightarrow u\bar{u}/d\bar{d}/s\bar{s}$	2.09	604.3	0.97
$c\bar{c}$	$e^+e^- \rightarrow c\bar{c}$	1.30	547.3	1.42
$b\bar{b}$	$e^+e^- \rightarrow b\bar{b}$ (half $B^+B^0$ and half $B^0B^0$ )	1.05	950	3.05
Bhabha	$e^+e^- \rightarrow e^+e^-$	28	5.3	0.02
$\mu\mu$	$e^+e^- \rightarrow \mu^+\mu^-$	1.16	151.1	0.44

Tab. V.2: Generated Monte Carlo events for this analysis

## CHAPTER VI

### EVENT PRESELECTION

We will study the spectral function that we get from  $\tau^- \rightarrow \pi^-\pi^0\nu_\tau$  decays using 300  $\text{fb}^{-1}$  data recorded on the BABAR detector. The analysis was done using 1-3 Topology, which means there is 1 track in signal( $\tau^- \rightarrow \pi^-\pi^0\nu_\tau$ ) hemisphere and 3 tracks on the other hemisphere in every event. To do the analysis effectively, we need to remove background as much possible and it can be done in 2 steps: preselection(mainly to remove non- $\tau$  events, discussed in this chapter) and event selection(mainly to remove non-signal events, next chapter).

The main goal of preselection is reduce the size of the data significantly from unwanted events. After preselection, preselected events will be saved in “ntuples” (organized package data).

#### 1 $\pi^0$ Candidate Preselection

$\pi^0$  decays to 2 photons almost 100%, and we only need 1  $\pi^0$ , so that we can remove all events which have more than 4 photons in 1 track hemisphere. Then, every pair of energy deposits in the EMC, which are isolated from any charged tracks, is considered as  $\pi^0$  candidate if both the energy deposits exceed 100 MeV and the associated invariant mass of the pair is between  $90 \text{ MeV}/c^2$  and  $160 \text{ MeV}/c^2$ .

## 2 Charged Candidate Preselection

Tracks are found independently in the two tracking devices, the silicon vertex detector and the drift chamber; different algorithms are used in each. The silicon vertex detector algorithm first combines  $r - \phi$  and  $z$  hits in the same silicon wafer to form space points, and then does an exhaustive search for good helical tracks, requiring hits in at least four out of the five layers of silicon.

The analysis is started by selecting events with a 1-3 topology and rejecting most of the high multiplicity  $q\bar{q}$  and low multiplicity QED backgrounds. The Tau1N skim is used in event selection. The criteria for the Tau1N selection are described in [58]. The further preselection requirements are listed below. Efficiencies for each cut are shown in Table VI.1.

The preselection requirements are listed below. The tag event store (*nano*-level) cuts are applied for convenience to reduce the size of data sample and remove background<sup>1</sup>.

- The following cuts are applied to speed up the processing of data:
  - Event has either **L3OutDch** or **L3OutEmc** trigger bit set
  - Event has **BGFMultiHadron** filter bit set.

**BGFMultiHadron** is a special filter that requires an event to have number of tracks bigger than 2 and R2 is bigger than 0.92. R2 is the ratio of the second and zeroth Fox-Wolfram moments. Its value ranges from (0,1). This quantity is indicative of the collimation (jettiness) of an event topology (closer to 1); values of R2 closer to 0 indicate a more spherical event. The Fox Wolfram moment is defined in [57].

---

<sup>1</sup>The nano information derived from the OEP is stored separately from the much larger fully reconstructed events, and as such cuts applied at the nano level are much more efficient in terms of computing resources.

- Event has **Tau1N** tag bit set. The Tau1N skim was designed for a common use by the Tau Analysis Working Group at BABAR. The skim is designed to select  $\tau$ -pair events classified as 1-N( $N \geq 3$ ) topology. The events are required to have more than 2 tracks but less than 11 tracks
- Exactly 4 ‘good tracks’ are required in the event.

For this analysis we select *good tracks* from the **GoodTracksVeryLoose**(see Appendix B) list of the micro level. The tracks are required in addition to point to the default primary vertex ( $docaXY < 1$  cm,  $docaZ < 5$  cm) and have a momentum in the range  $p_T > 0.1$  GeV/c,  $p < 10$  GeV/c in the Lab frame<sup>2</sup>. The tracks identified as a part of a converted photon candidate (found in **gammaConversionDefault** list) are not counted as good tracks. No attempt has been made to reconstruct  $K_S$  decays.

- The event is divided on two hemispheres using the plane perpendicular to the thrust of the event. The sign of scalar product of the given track momentum with thrust direction determines which hemisphere this track belongs to.

The thrust is defined by

$$T = \max_{|n|=1} \frac{\sum_i |n.p_i|}{\sum_i |p_i|}, \quad (\text{VI.1})$$

where  $n$  is a unit vector. By definition, the thrust axis is chosen to minimize the sum of transverse momenta of all particles in an event, where momenta is taken with respect to this axis.

The thrust axis of the event is calculated using charged and neutral (with energy greater than 50 MeV) particle candidates in the center-of-mass frame (CM). One

---

<sup>2</sup>The Lab frame is the rest frame of the detector, as opposed to the rest frame of the  $e^+e^-$  collisions.

hemisphere must have exactly one good track, while other 3 tracks must belong to the second hemisphere. Each hemisphere must have total charge either -1 or +1. The total charge of the good tracks is equal to 0. This defines a *Confirmed topology*.

- $0.8 \leq \text{Thrust} \leq 0.985$ .

Thrust magnitude varies from 0.5 for isotropic events to 1.0 for back to back events. Since  $e^+e^- \rightarrow q\bar{q}$  events are more isotropic than  $e^+e^- \rightarrow \tau^+\tau^-$  events, one can differentiate  $\tau$  events from  $q\bar{q}$  events. Bhabha events have Thrust about 1, and this upper cut is effective to remove Bhabhas. While the lower cut is effective to remove  $q\bar{q}$ -background events.

- Number of clusters  $\leq 4$  in one track hemisphere

We select photon candidates from **CalorNeutral** list [63], which are single EMC bumps not matched with any track and have lateral moment  $< 0.8$  and energy  $> 100$  MeV. We reject all events which have more than 4 clusters in one track hemisphere. We select good neutrals from CalorNeutrals, which are single EMC bumps not matched with any track.

- $0.09 < M_{\pi^0} < 0.16$  GeV

We reconstruct  $\pi^0$  from 2 photon candidates, we pair all cluster to reconstruct all possible  $\pi^0$ , we save only events with at least 1  $\pi^0$  whose mass  $0.09 < M_{\pi^0} < 0.16$  GeV.

Cuts are applied sequentially and quoted in the table. The trigger cut means DCH or EMC trigger standard cuts(technically, one can say **L3OutDch** or **L3OutEmc** tagbit is set).

	$\tau$ Generic	uds	$C\bar{C}$	$B^0\bar{B}^0$	$B^+B^-$	Bhabha	DATA
Trigger	84.45	95.46	98.89	99.74	99.76	20.08	100.00
Passed BGFMultiHadron or BGFTau	99.73	99.25	99.38	99.45	99.61	2.24	98.84
Total Charge = 0	90.10	54.86	46.22	35.69	35.89	83.93	60.21
Confirmed 1-3 Topology	76.75	60.94	55.89	52.54	20.45	32.98	61.49
$0.8 < Thrust < 0.995$	98.25	79.87	70.51	20.80	4.70	4.84	73.54
nCluster $\leq 4$	98.02	70.83	57.12	70.77	3.01	56.80	87.66

Tab. VI.1: Event PreSelection Table After Tau1N. Preselection efficiencies in percent for Data and Monte Carlo background samples.

Cuts are applied sequentially and the marginal efficiencies are quoted

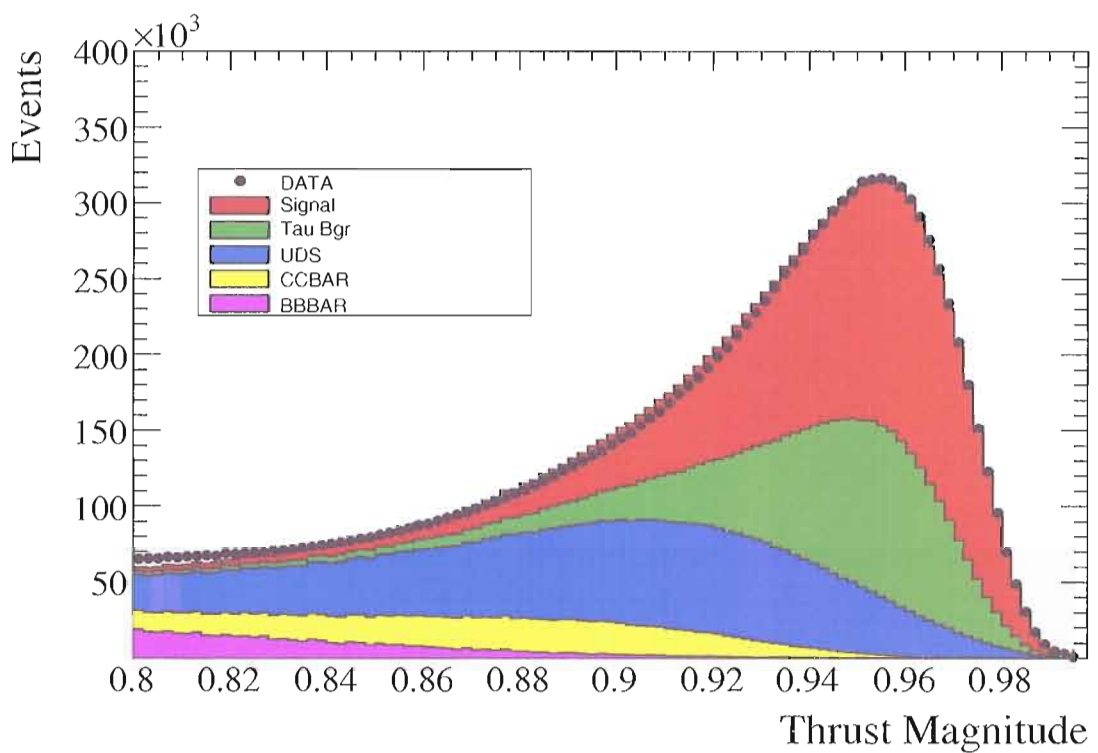


Fig. VI.1: Thrust Magnitude of MC and Data, all preselection cuts have been applied, except thrust magnitude cut. All MC samples are normalized to Data Luminosity.

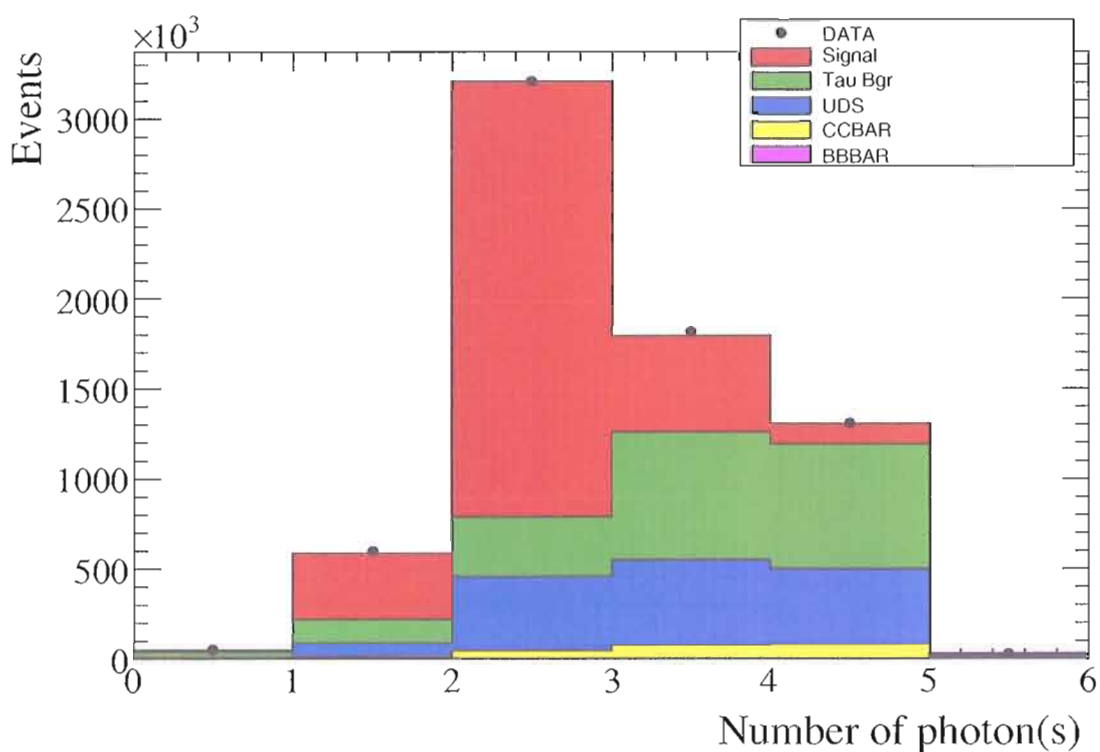


Fig. VI.2: The number of photon in signal hemisphere of MC and Data Distribution, all selection cuts have been applied, except number of cluster cut. All MC are normalized to Data Luminosity.

## CHAPTER VII

### EVENT SELECTION

In this analysis, the  $\tau^- \rightarrow \pi^-\pi^0\nu_\tau$  decay is called **signal**(see Figure VII.1) and all other decays are called as **background**. To be able to understand the signal, one should try to remove background as much as possible. The events that survived event selection are called **selected events**.

#### 1 Event Reconstruction

A pair of energy deposits in the EMC, which are isolated from any charged tracks, is considered as  $\pi^0$  candidate if both the energy deposits exceed 100 MeV and the associated invariant mass of the pair is between  $115 \text{ MeV}/c^2$  and  $155 \text{ MeV}/c^2$  with  $E_{\pi^0}$  bigger than 450 MeV(LAB). The  $\rho$  meson candidates are made by combining a selected  $\pi^0$  candidate with a charged track on the signal side.

#### 2 Selection Process

After preselection cuts applied to Data and Monte Carlo, all events are saved in ntuples, occupy about 100 GB and from Monte Carlo study we estimate that we still have significant number of backgrounds. To increase the purity, we apply event selection cut

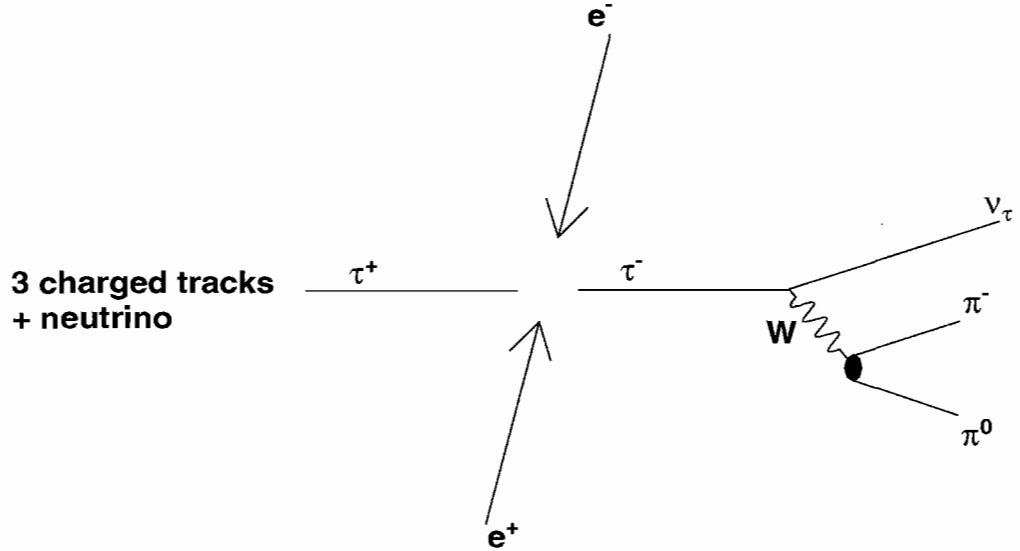


Fig. VII.1: Simplified picture of event reconstruction in this analysis.

- All tracks are required to fall in the fiducial range of detectors that we understand well. In this analysis we require  $-0.82 \leq \cos \theta_{track} \leq 0.98$  is the polar angle of the charged track candidates.
- Figure VII.6 shows the polar angle of missing momentum. In this analysis, the polar angle of missing momentum in the LAB frame is required to be  $-0.82 \leq \cos \theta_{miss} \leq 0.92$ .
- From Figure VI.2 we can see that most of our signal has 2 photons on one track hemisphere, so that we require only 2 photons on signal hemisphere, and both photons have energy bigger than 100 MeV in the LAB frame. From LorentzVector, we reconstruct  $\pi^0$  and asking  $\pi^0$  mass fall in the window 115 MeV to 155 MeV. Using these requirements we reduce tau backgrounds significantly, especially from  $\tau \rightarrow \pi^- \pi^0 \pi^0$ .

- In Figure VI.1 we can see that we reduce non-tau background if we use events which have  $0.9 \leq \text{Thrust} \leq 0.985$ , the upper thrust cut effective to remove Bhabhaswhile the lower thrust cut effective to reduce hadronic background.
- We reject  $\pi^0$  which have energy below 450 MeV (LAB frame) due discrepancy between Data and MC which have  $E_{\pi^0} \leq 450$  MeV(see Figure VII.4)
- To reduce background further, we require that the total mass on 3 prong side is less than 1.8 GeV.

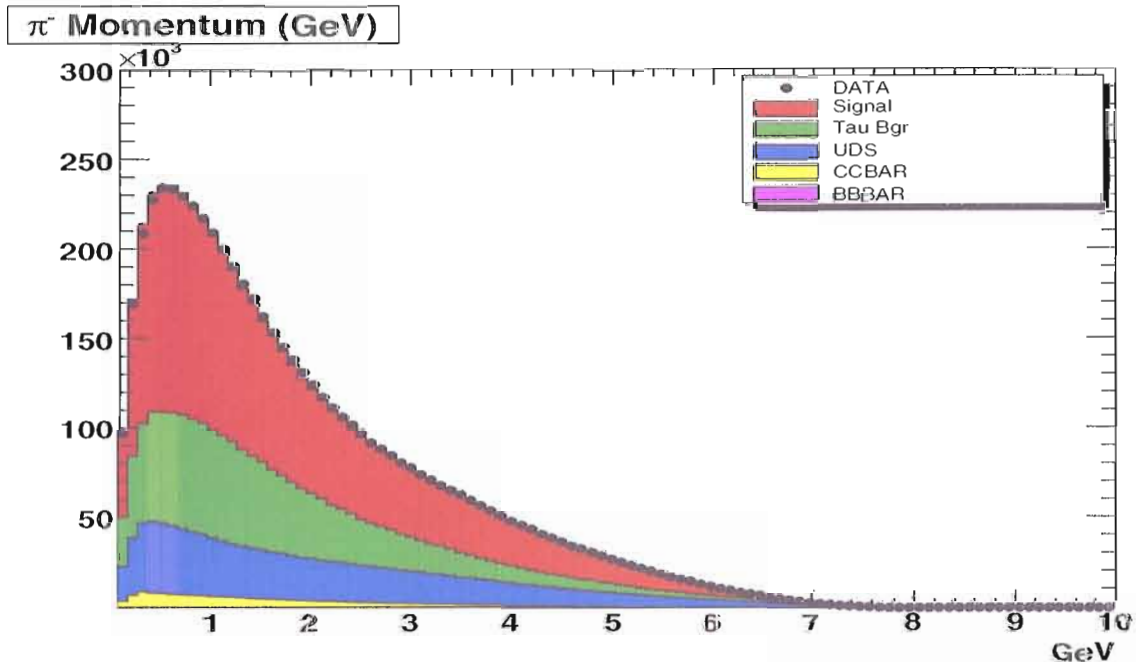


Fig. VII.2: The  $\pi^-$  Momentum (in  $\text{GeV}/c$ ) of the signal  $\pi^-\pi^0$ , in the LAB frame. All Monte Carlo samples are generated using SP8 and normalized to collected Data Luminosity. DATA and Monte Carlo show good agreement, All cuts have been applied, except  $\pi^-$  Momentum cut.

The table of event selection efficiency(see Table VII.1) is in sequential percentage(%) of efficiency after each cut.

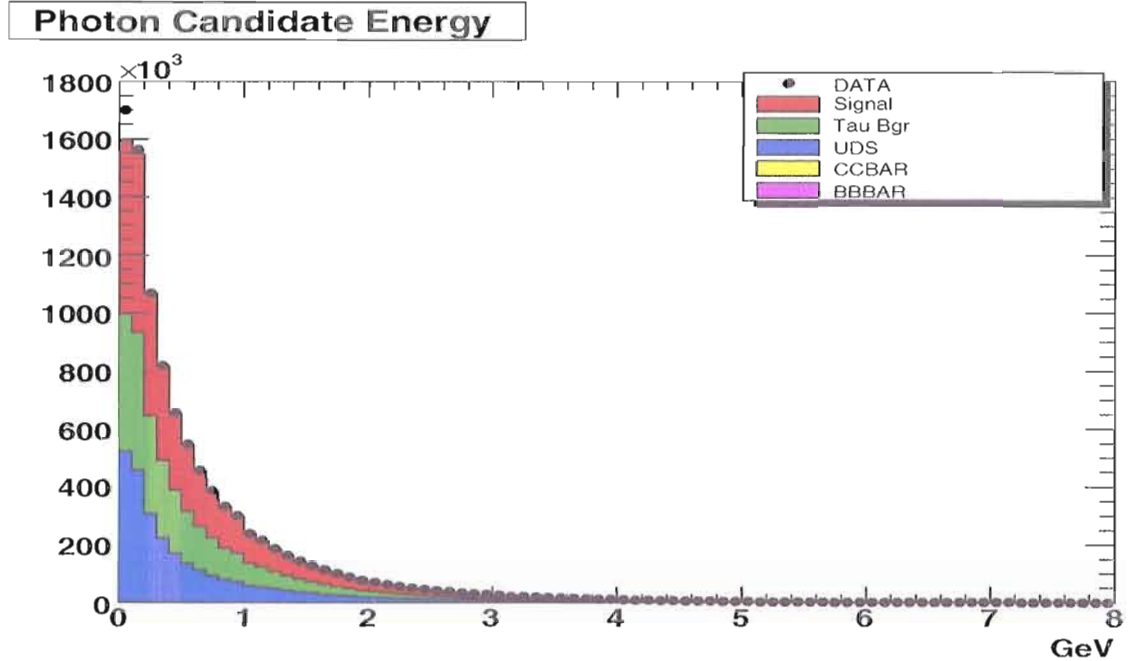


Fig. VII.3: The  $\gamma$  Candidate Energy (in GeV) on the signal side, in the LAB frame. All MC samples are normalized to the collected Data Luminosity. DATA and MC show good agreement, all cuts have been applied, except  $\gamma$  energy cut.

In addition, by choosing 1-3 Topology, we get much smaller Bhabhas, mupair, two-photon backgrounds compared to 1-1 Topology. We would like to emphasize that the chance that Bhabha and Mupair mimic the channel is very small, due to the fact that Bhabha, mupair(mostly they decay to 1-1 Topology) and two-photon background have totally different topology. In addition, by requiring exactly two photons in signal hemisphere would make Bhabha,mupair and two-photon contributions very small, due to the fact that these backgrounds produce two photons on 1-track hemispher very rarely. From the previous study done in  $\tau \rightarrow lll$  [64] and  $\tau \rightarrow lhh$ [65], which used the same preslection, from the tables in those analysis, we can assume that the contribution from Bhabha, mu-pair are negligible.

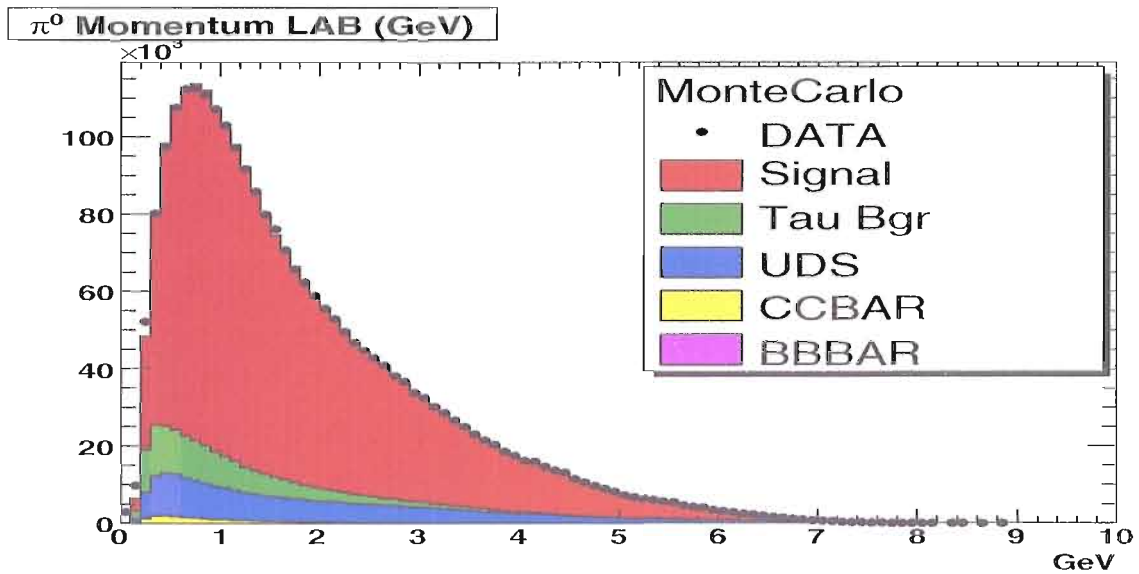


Fig. VII.4: The  $\pi^0$  Momentum (in GeV/c) of the signal  $\pi^-\pi^0$ , in the LAB frame. All MC samples are normalized to the collected Data Luminosity. DATA and MC show good agreement, all cuts have been applied, except  $\pi^-$  Momentum cut.

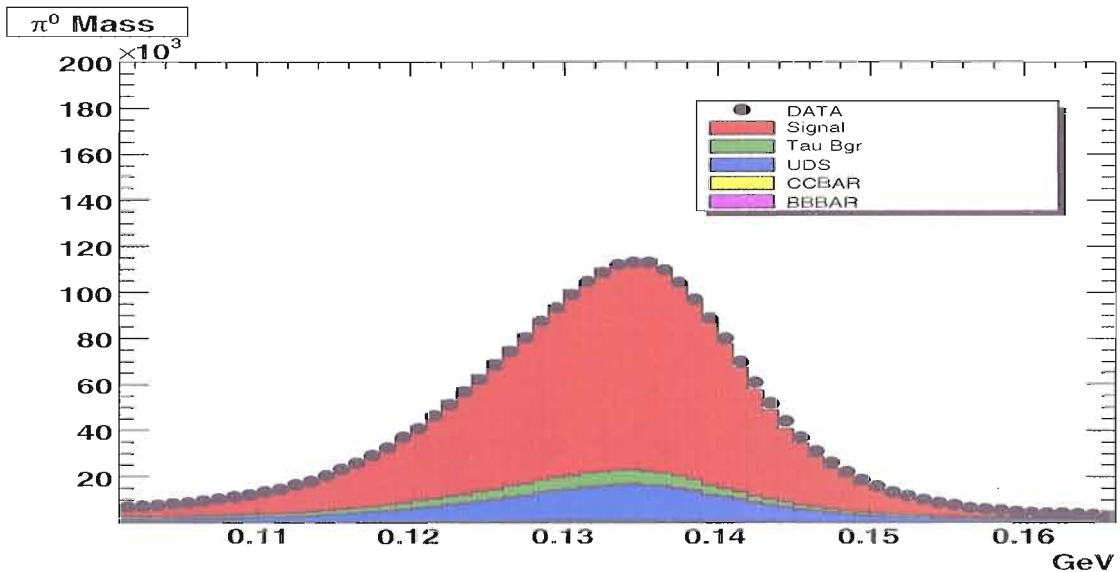


Fig. VII.5: The  $\pi^0$  invariant mass (in GeV) of the signal  $\pi^-\pi^0$ . All MC samples are normalized to the collected Data Luminosity. DATA and MC show good agreement, all cuts have been applied, except  $\pi^0$  Mass cut.

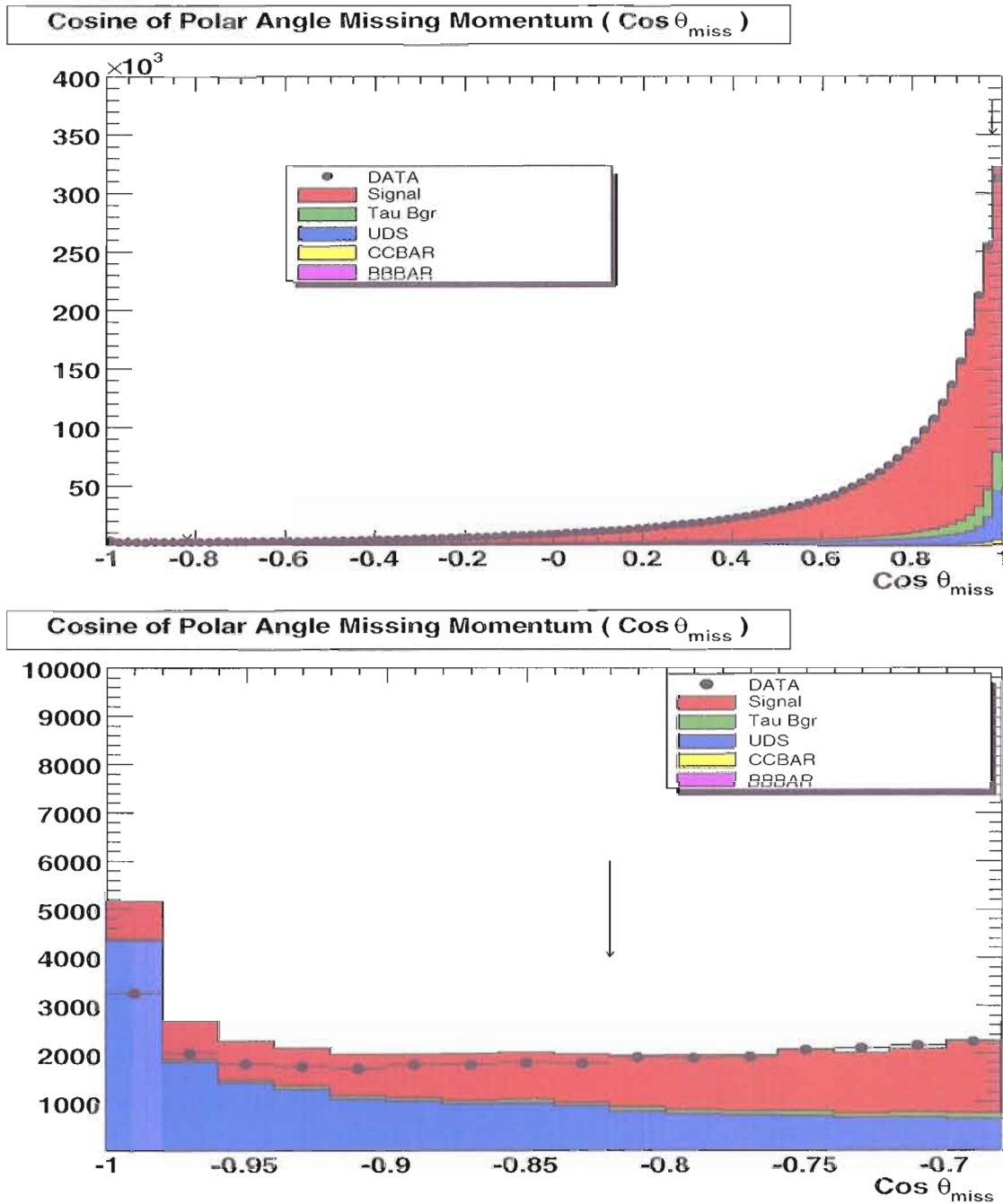


Fig. VII.6: Polar Angle of Missing Momentum  $\theta_{\text{miss}}$  (rad) of the event in the LAB frame. All MC samples are normalized to the collected Data Luminosity. DATA and MC show good agreement. All cuts have been applied, except polar angle of missing momentum  $\theta_{\text{miss}}$  cut. The lower plot is the zoom for high polar angle region, where cut is applied to reduce the contributions from non-signal events.

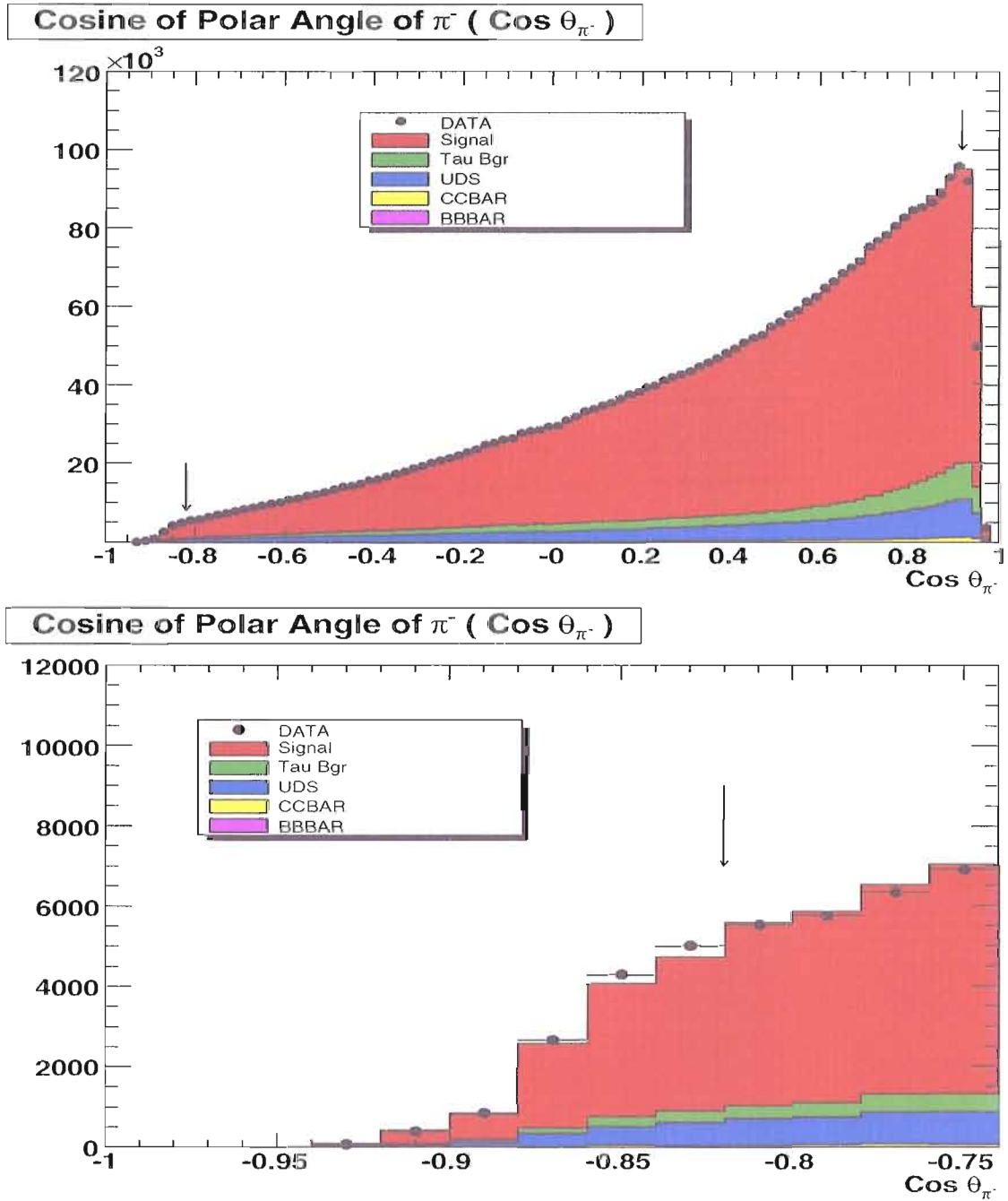


Fig. VII.7: The Polar Angle of  $\pi^-$  (rad) in the LAB frame. All MC samples are normalized to the collected Data Luminosity. DATA and MC show good agreement, all cuts have been applied, except the polar angle of  $\pi^-$  cut. The lower plot is the zoom for high polar angle region, cuts are applied to non-signal events.

	Signal	$\tau$ Bgr	UDS	$C\bar{C}$	$B^0\bar{B}^0$	$B^+\bar{B}^-$	DATA
Preselection	100.00	100.00	100.00	100.00	100.00	100.00	100.00
$0.9 \leq Thrust \leq 0.985$	88.58	89.08	47.08	26.16	4.11	4.12	67.40
$-0.82 \leq \text{Cos } \theta_{miss} \leq 0.92$	68.42	62.94	65.06	56.73	49.15	54.12	66.88
$-0.82 \leq \text{Cos } \theta_{track} \leq 0.98$	93.12	78.21	92.98	93.32	92.57	94.62	41.83
Exactly 2 100-MeV clusters	65.94	19.36	23.81	15.95	26.74	21.38	44.97
$115 \leq M_{\pi^0} \leq 155$ MeV	94.56	54.88	72.86	66.50	78.00	76.74	86.34
$E_{\pi^0} > 450$ MeV	93.81	72.21	88.25	78.91	76.92	80.82	91.94
Mass 3 prong $< 1.8$ MeV	99.88	96.73	85.78	88.79	83.33	86.88	98.93
Expected Events	2183168	60164	42059	12518	108	98	2318974
Percentage(%)	95.00	2.62	1.84	0.54	0.00	0.00	

Tab. VII.1: Event Selection Table in sequential percentage(%) of efficiency after each cut. MC is normalized to data luminosity

### 3 Final Event Sample

We normalize all Monte Carlo to the Data Luminosity from RUN 1-5, using Bbk-Lumi(standard BABAR package to calculate luminosity), no additional luminosity correction applied. After passing event selection, there are 2318974 events of data and 2298565 MC events(normalized to Data Luminosity) remain which dominated by signal events(2,183,168 events).

We define the efficiency( $\varepsilon$ ) as the the number of selected  $\pi^-\pi^0$  events ( $N_{selected}^{signal}$ ) divided by the number generated  $\pi^-\pi^0$  events ( $N_{generated}^{signal}$ ). The efficiency plot can be seen in Figure VII.10

$$\varepsilon = \frac{N_{selected}^{signal}}{N_{generated}^{signal}}, \quad (\text{VII.1})$$

The overall efficiency in this analysis is about 1.5 %, which understandable because we are using 1-3 Topology (only about 14% of  $\tau$  decays to 3 tracks).

We define the purity( $P$ ) as the percentage of number of selected  $\pi^-\pi^0$  events ( $N_{selected}^{signal}$ ) divided by the total number of selected MC events ( $N_{selected}^{MC}$ ) events(signal + backgrounds).

$$P = \frac{N_{selected}^{signal}}{N_{selected}^{MC}}. \quad (\text{VII.2})$$

Total number of events from MC background is very small (less than 5%). We have a high purity sample because about 95% signal events survive.

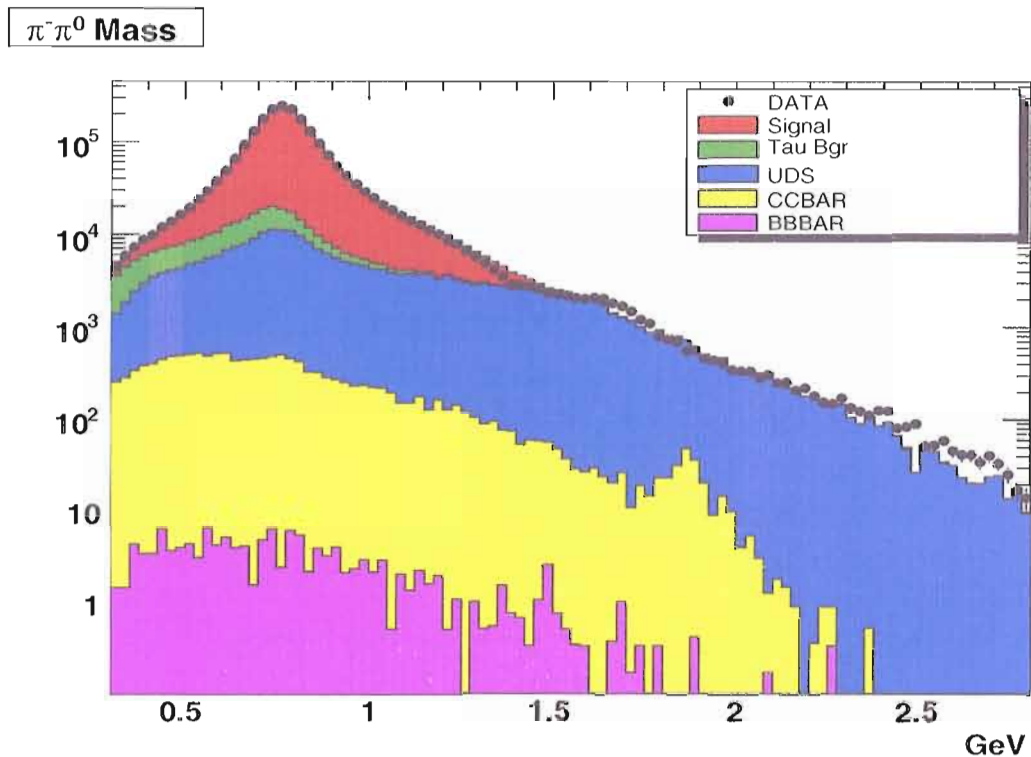


Fig. VII.8: The plot of the  $\pi^- \pi^0$  invariant mass of Data(black dots) and MC samples, all Monte Carlo samples are normalized to data luminosity. The major backgrounds are the contributions from non signal  $\tau$  and continuum  $q\bar{q}$  backgrounds

MC Backgrounds are simply subtracted from final data sample, no additional correction applied at this stage.

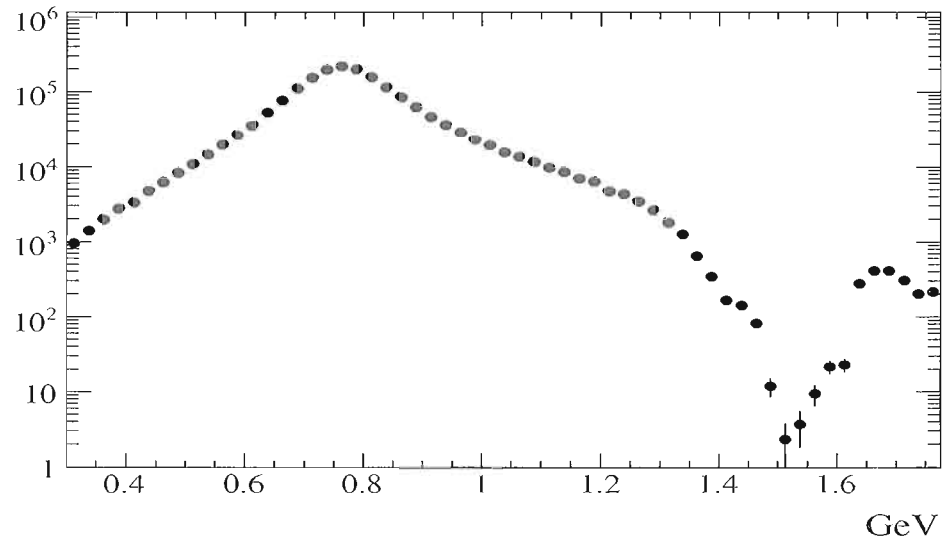


Fig. VII.9: The plot of  $\pi^- \pi^0$  invariant mass after MC backgrounds are subtracted from Data. The dip about 1.5 GeV shows a destructive interference between  $\rho'$  and  $\rho''$ .

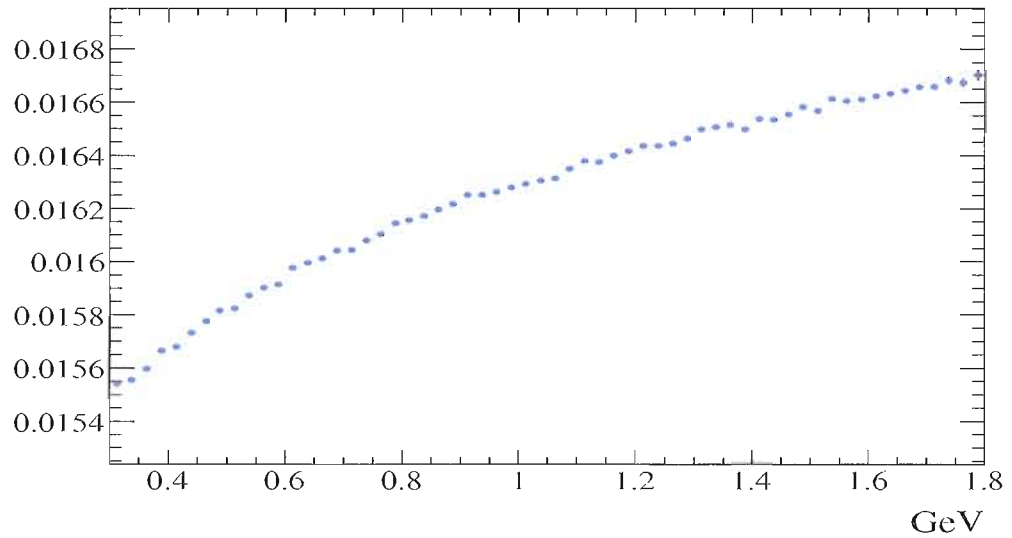


Fig. VII.10: The efficiency plot, as defined by the number of selected  $\pi^- \pi^0$  events divided by the number of generated  $\pi^- \pi^0$  events, plotted as a function of  $\pi^- \pi^0$  invariant mass.

## CHAPTER VIII

### UNFOLDING

The measured spectrum of a physical observable, like the invariant mass or the lepton energy, is distorted by detector effects. A comparison of the spectrum with theoretical predictions and with the spectra measured by other experiments, affected by different detector effects, is therefore difficult. Thus, the removal of the distortions to obtain the true, underlying physical spectrum is desirable.

In order to extract the physical mass distribution (and hence the fully corrected partial width as a function of invariant  $\pi^-\pi^0$  mass for the signal decay) it is necessary to unfold the measured spectrum from the effects of measurement distortion. The RooUnfHistoSyd package [70] software package contains routines which perform the relevant procedure, a description of which is contained in the following sections.

The effects of finite resolution on an invariant mass distribution during the measurement process can be written as:

$$Ax_j = b_i \quad (\text{VIII.1})$$

where  $x = x_1, \dots, x_j$  is the binned true mass distribution to be determined and  $b = b_1, \dots, b_i$  is the measured distribution.  $A = A_{11}, \dots, A_{ij}$  is the detector response matrix which can be produced by simulating the measurement process using MC techniques. The matrix element  $A_{ij}$  gives the probability that an event with a true

mass in bin  $j$  is reconstructed in bin  $i$ . If we generate the distribution and perform our detector simulation, every entry in a measured bin can be traced back to its origin, giving us a set of relations between the generated and measured distributions, as in Equation VIII.1. In the unfolding procedure, matrix  $A$  incorporates the efficiency and resolution matrix.

Because the matrix  $A$  is usually singular, the direct inversion leads to unstable and therefore useless results. The following sections outline the steps in solving Equations VIII.1. The method, based the *singular value decomposition* of the response matrix  $A$ .

## 1 Singular Value Decomposition

A Singular Value Decomposition(SVD) of a real  $m \times n$  matrix  $A$  is its factorization of the form

$$A = USV^T, \quad (\text{VIII.2})$$

where  $U$  is an  $m \times m$  orthogonal matrix,  $V$  is an  $n \times n$  orthogonal matrix, while  $S$  is an  $m \times n$  diagonal matrix

$$UU^T = U^TU = I, \quad (\text{VIII.3})$$

$$VV^T = V^TV = I, \quad (\text{VIII.4})$$

$$S_{ij} = 0 \text{ for } i \neq j, S_{ii} \equiv s_i. \quad (\text{VIII.5})$$

The quantities  $s_i$  are called *singular values* of the matrix  $A$ . and columns of  $U$  and  $V$  are called the left and right *singular vectors*.

The singular values contain very valuable information about the properties of the matrix. If, for example, A is itself orthogonal, all of its singular values are equal to 1. On the contrary, a degenerate matrix will have at least one zero among its singular values. In fact the rank, the rank of a matrix is the number of its non-zero singular values. Once the matrix is decomposed into the form written in Equation VIII.2, its properties can be analyzed and it becomes very easy to manipulate. This technique is extremely useful for ill-defined linear systems with almost (or even exactly) degenerate matrices. Comprehensive description of SVD with many technical details can be found in [71] and [72]

Once the matrix is decomposed into the form VIII.2, progress can be made. The factorization in this way means that its properties can be analyzed and calculation is made less difficult.

## 2 Unfolding Procedure

We study about the reconstruction of generated  $\pi^-\pi^0$  using MC. The inputs for Unfolding are Background-subtracted Data plot, 2D MC Truth-Reco matrix and efficiency plot. Some useful plots are shown in Figure VIII.1 (2 dimensional plot) and VIII.2 (3 dimensional plot to clarify 2 dimensional plot). The output of unfolding is the unfolded plot.

At the end of unfolding procedure, the final result of unfolding of Background subtracted data is compared to the one without unfolding(see Figure VIII.4).

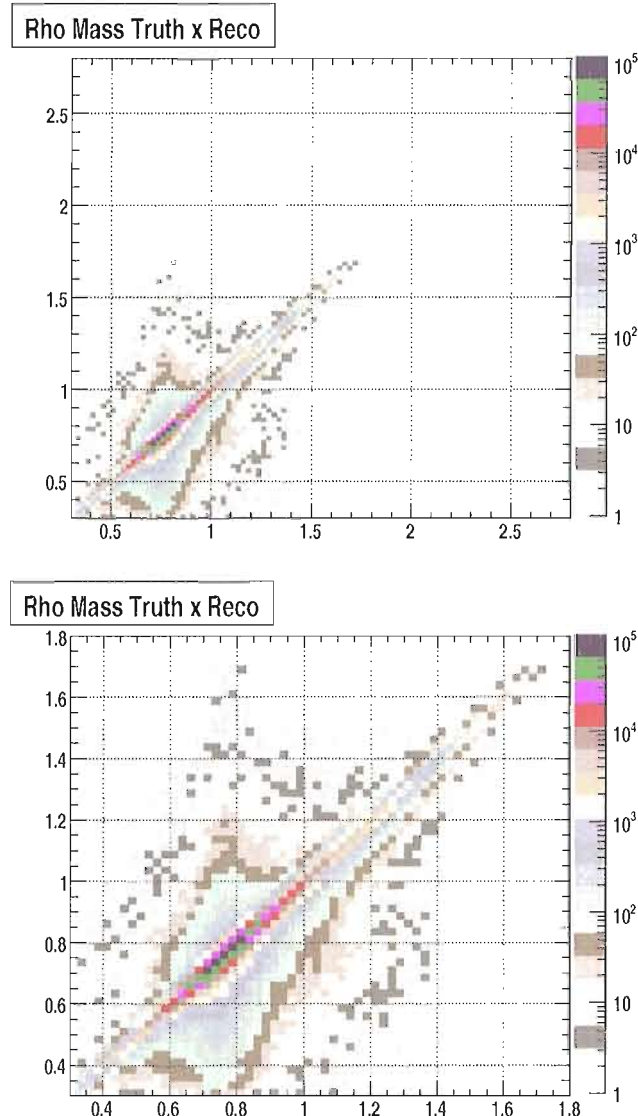


Fig. VIII.1: Unfolding Matrix in 2D. The upper plot is the unfolding matrix for full MC with  $0.3 \text{ GeV} < M_{\pi-\pi^0} < 2.8 \text{ GeV}$ . The lower plot is the unfolding matrix for lower mass region MC with  $0.3 \text{ GeV} < M_{\pi-\pi^0} < 1.8 \text{ GeV}$ . Efficiency is not included.

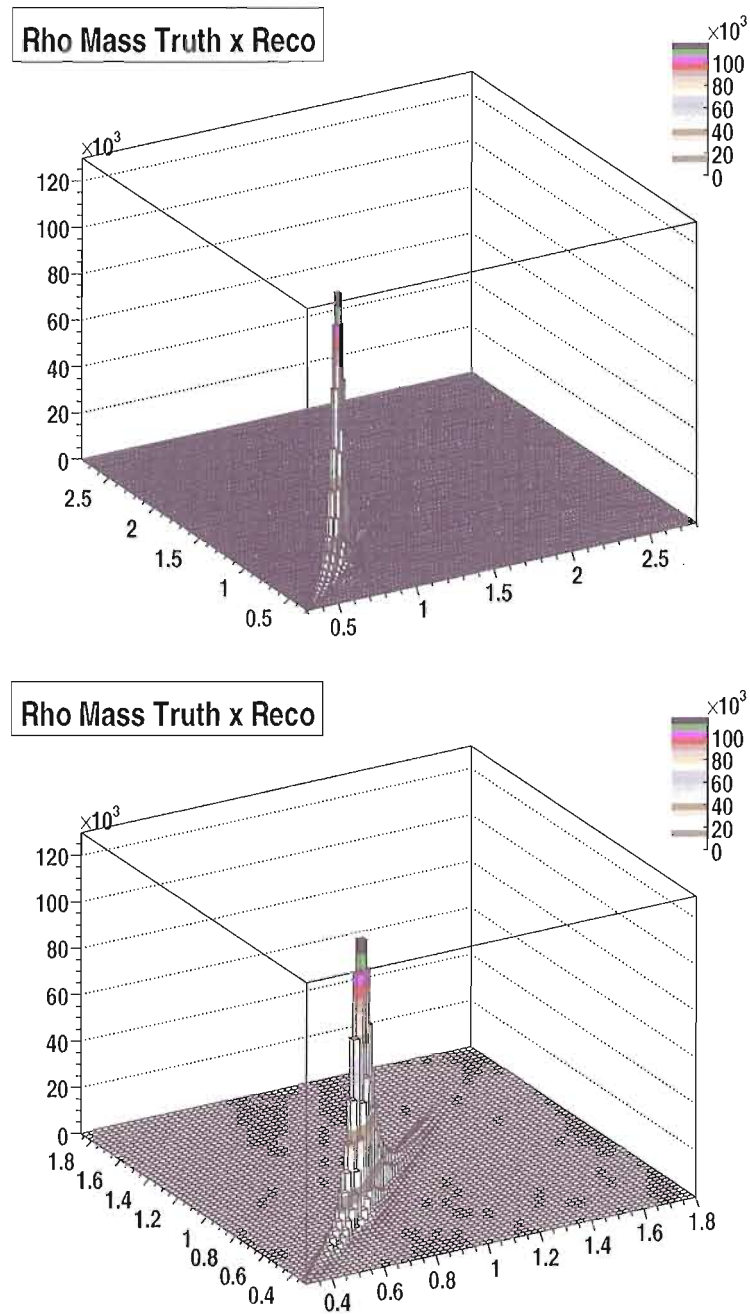


Fig. VIII.2: Unfolding Matrix in 3D. The upper plot is the unfolding matrix in box style for full MC with  $0.3 \text{ GeV} < M_{\pi^- \pi^0} < 2.8 \text{ GeV}$ . The lower plot is the unfolding matrix in box style for lower mass region MC with  $0.3 \text{ GeV} < M_{\pi^- \pi^0} < 1.8 \text{ GeV}$ . Efficiency is not included.

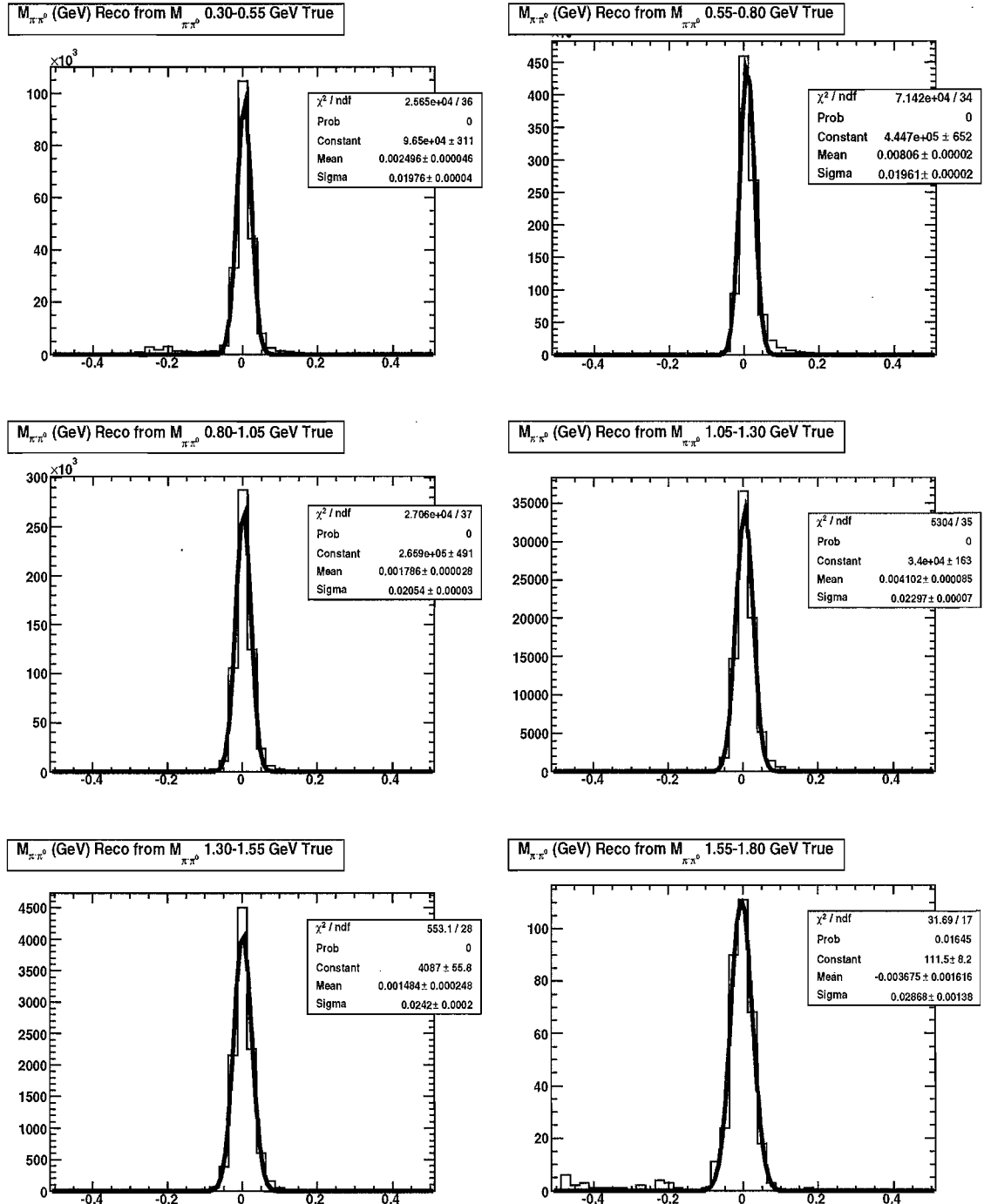


Fig. VIII.3: The Reconstruction Mass - The True Mass and fit it using Gaussian. The 0s are the mean value of invariant mass of the specific truth bins

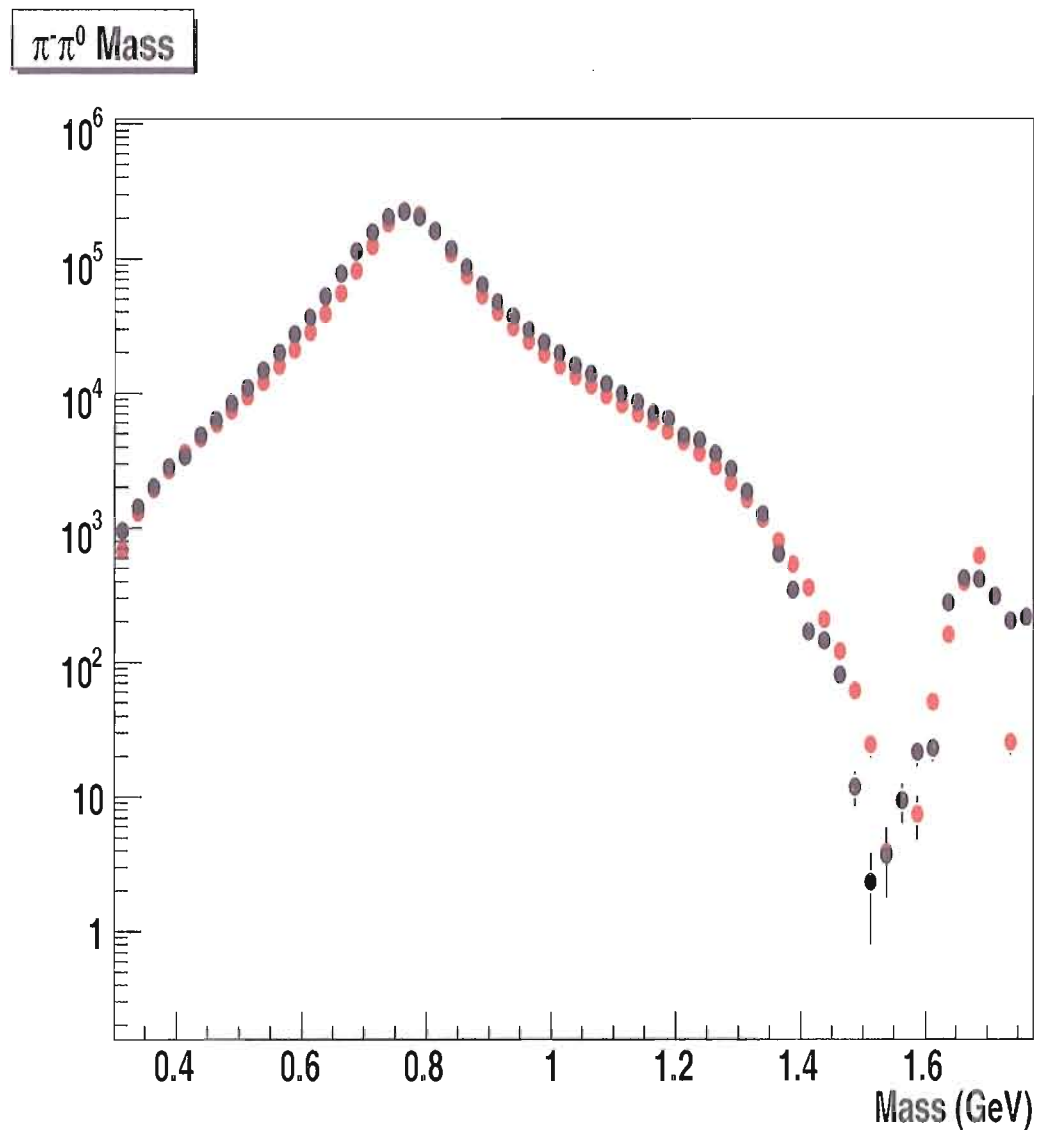


Fig. VIII.4: Comparison between background-subtracted DATA(black) and Unfolded DATA(red)

## CHAPTER IX

### FITTING RESULTS

To obtain the important parameters in this analysis, a  $\chi^2$  fit using Gounaris-Sakurai function (see Section 2) is performed to the unfolded invariant  $\pi^-\pi^0$  mass spectrum. The Gounaris-Sakurai function is used in this thesis, because it is used in many  $\tau$  experiments such as OPAL [6], CLEO[5], ALEPH[4] and Belle, to fit invariant  $\pi^-\pi^0$  mass.

The off-diagonal components of the covariance matrix of bin-by-bin invariant mass in this analysis are small(about 0.1%), and not included in  $\chi^2$  evaluation. The reason the smallness of off-diagonal components of the covariance matrix is because the bin size(25 MeV) is bigger than resolution(about 20 MeV).

The fit utilizes a calculation software, RooFit[33], with 10 free parameters, we obtain the result of Fitting parameters using Gounaris-Sakurai and their statistical errors. We found the value of  $\chi^2/\text{d.o.f}$ (degree of freedom) of default is around 48/50.

The dip about 1.6 GeV in invariant  $\pi^-\pi^0$  mass is predicted from destructive interference of  $\rho'$  and  $\rho''$

The value of  $|F_\pi|^2$  at  $s = 0$ , is expected to be 1, and in this analysis we didn't fix the value  $|F_\pi(s = 0)|^2 = 1$ . Using the parameter values in Table IX we can interpolate the value of  $|F_\pi(0)|^2$  and we get  $|F_\pi(0)|^2 = 1.008 \pm 0.09$ , very close to unity. The  $|F_\pi(0)|^2$  uncertainty is calculated by varying the input parameters that go into  $|F_\pi(0)|^2$ , using

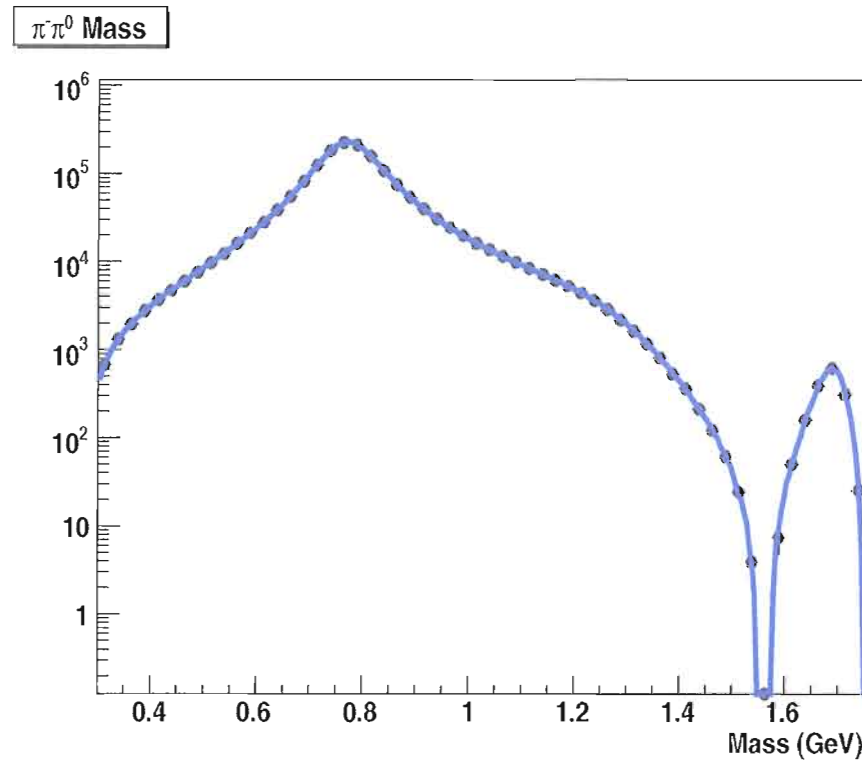


Fig. IX.1: Fitting to Unfolded Background Subtracted Data using Gounaris Sakurai Function

G&S Parameters	
$M_\rho$	$774.4 \pm 0.2$ MeV
$\Gamma_\rho$	$1499 \pm 0.3$ MeV
$M_{\rho'}$	$1298.3 \pm 24.4$ MeV
$\Gamma_{\rho'}$	$501.2 \pm 12$ MeV
$M_{\rho''}$	$1652.4 \pm 6.8$ MeV
$\Gamma_{\rho''}$	$245.3 \pm 36.2$ MeV
$\beta$	$0.088 \pm 0.012$
$\gamma$	$0.058 \pm 0.008$
$ \phi_\beta $	$118.3 \pm 8.2$ deg
$ \phi_\gamma $	$58.9 \pm 8.2$ deg
$\chi^2/\text{d.o.f}$	48/50

Tab. IX.1: Fitting Result with Gounaris Sakurai Function. The statistical errors are shown in the table

the statistical uncertainties in Table IX.

Below is the Correlation Matrix between all fit parameters in Gounaris-Sakurai Fit. The result taken from RooFit.

	Correlation Matrix							
	$M_\rho$	$M_{\rho'}$	$M_{\rho''}$	$\Gamma_\rho$	$\Gamma_{\rho'}$	$\Gamma_{\rho''}$	$\beta$	$\gamma$
$M_\rho$	1.000							
$M_{\rho'}$	-0.008	1.000						
$M_{\rho''}$	-0.006	-0.002	1.000					
$\Gamma_\rho$	0.007	0.003	-0.001	1.000				
$\Gamma_{\rho'}$	-0.005	-0.001	-0.001	0.004	1.000			
$\Gamma_{\rho''}$	-0.005	-0.000	-0.001	-0.001	-0.004	1.000		
$\beta$	-0.004	-0.000	-0.004	0.002	-0.002	-0.004	1.000	
$\gamma$	-0.009	-0.008	-0.002	0.009	-0.008	-0.009	-0.011	1.000

Tab. IX.2: Correlation Matrix between fit parameters

## 1 Form Factor

Form factor is calculated from numerical integration, but in this part only we study it in model-independent (no KS or GS functions are used). To have model-independent study, we can also use Equation IX.1 from [5] and the spectral function of selected Data after background subtraction to calculate the pion Form Factor  $|F_\pi(q^2)|^2$  as:

$$\bar{v}^{\pi\pi}(M_i) = \frac{B_{\pi\pi^0}}{B_e} \frac{M_\tau^8}{12\pi|Vud|^2} \frac{S_{EW}^e}{S_{EW}^{\pi\pi}} \frac{1}{M_i(M_\tau^2 - M_i^2)^2(M_\tau^2 + 2M_i^2)} \frac{1}{N} \frac{N_i}{\Delta M_i}, \quad (\text{IX.1})$$

$M_i$  is the central value of  $M_{\pi\pi^0}$  for the  $i^{th}$  bin,

$N_i$  is the number of entries in the  $i^{th}$  bin,

$N$  is the total number of entries,

$B_{\pi\pi^0}$  is the branching fraction  $\tau^- \rightarrow \pi^-\pi^0\nu_\tau$

$B_e$  is the branching fraction  $\tau^- \rightarrow e^-\bar{\nu}_e\nu_\tau$

$M_\tau$  is the  $\tau$  mass

$|V_{ud}|$  is a component in CKM matrix

$S_{EW}$  is the electroweak radiative correction

This model-independent form factor is shown in Figure IX.2

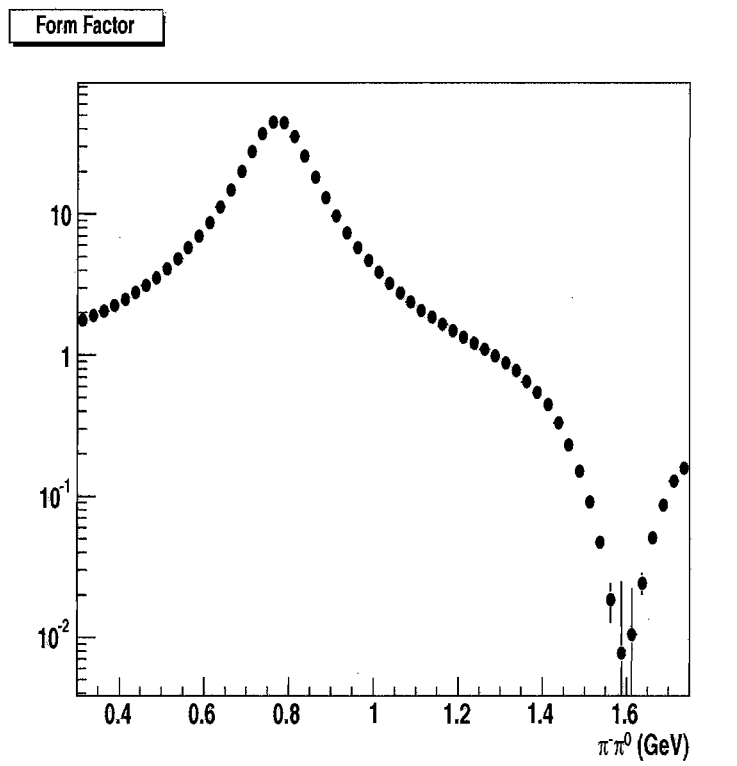


Fig. IX.2: The pion Form factor  $|F|^2$  as derived from the spectral function of selected Data after background subtraction

## 2 Integration Procedure

To evaluate  $a_\mu^{\pi\pi^0}$ , we perform a numerical integration employing the Gounaris-Sakurai model(see Section 2 Chapter III) to the unfolded  $\pi^-\pi^0$  mass spectrum. This procedure has more benefits relative to direct integration of the data points because the effects of statistical fluctuations are reduced particularly in the low-entries bins and is technically simple to implement. The disadvantages include possible biases associated with choice of model.

The range of integration is from  $\sqrt{s} = 0.5$  to 1.8 GeV of invariant  $\pi^-\pi^0$  mass.  $a_\mu^{\pi\pi}$  calculation in this range(0.5-1.8 GeV) from  $\tau$  data has (about 2 times) better precision than  $e^+e^-$  data.  $a_\mu^{\pi\pi}$  calculation from  $2m_\pi$ -0.5 GeV, is already available from  $e^+e^-$  data with very high precision compared to all  $\tau$  data[34].

From this procedure that includes electroweak factor( $S_{EW} = 1.0232 \pm 0.0006$ ) we obtain, prior to application of the corrections that will be described in Section 1 Chapter XI,

$$a_\mu^{\pi\pi}(0.50, 1.80) = 458.45 \pm 0.40(stat). \quad (\text{IX.2})$$

We have checked this method of integrating the spectral function by reproducing the CLEO evaluation. We take the fitting results of CLEO's table and put these parameters in our  $a_\mu^{\pi\pi}$  function to be integrated analytically. and the result agrees with the value they obtained.

# CHAPTER X

## UNCERTAINTIES

### 1 Method

It is very important to study to the systematic uncertainties in this precision measurement analysis. There are two sources of systematic uncertainties: external systematic uncertainties and internal systematic uncertainties. The external systematic uncertainties are all uncertainties that come from outside this BABAR experiment and usually calculated in other experiments, such as uncertainty of  $|V_{ud}|$  and  $S_{EW}$ , these will be discussed in the next chapter.

In this chapter, we focus on the internal systematic uncertainties, which defined as all uncertainties that come from inside this BABAR experiment and the next sections will discuss all of the major internal systematic uncertainties. We study the systematic uncertainties by varying the inputs corresponding to their uncertainties that enter the equations, including MC inputs and reevaluate everything. For example the uncertainties of non-signal  $\tau$  background are studied by varying the contribution of specific  $\tau$  channels by their branching fraction uncertainties taken from the PDG 2007. Other internal systematic uncertainties are studied in the same spirit using independent samples.

The sources of uncertainties can be classified into efficiency, resolution, other systematic and statistical uncertainties. All of them will be discussed in the following subsections.

## 2 Efficiency

### 2.1 Tracking

One should study the efficiency of charged tracks. This analysis studied the tracking efficiency correction using the table from AWG Charged Particles(Hamano's table). The tracking efficiency was studied using Tau 1-3 Topology, which means that each event, three tracks in one hemisphere and one track(in this study electron or muon) in the other hemisphere. All events are divided into 6 bins in Pt, 6 bins in  $\theta$ (Theta) and 3 bins in  $\phi$ (Phi), as prescribed in the recipe of AWG Charged Particles. This analysis takes the difference between initial values and values after efficiency correction as our systematic uncertainty. The result of this study is in Table X.1.

### 2.2 $\pi^0$ Efficiency

This analysis use  $e^+e^- \rightarrow \mu^+\mu^-\gamma$  decays as independent control samples to study *photon* efficiency. Main advantages of  $e^+e^- \rightarrow \mu^+\mu^-\gamma$  channel are it has large number of events and very low multiplicities(tracks) with small background and one can reconstruct the characteristic of photon from the detected 2 muons in each event without information from the calorimeter. In addition,  $e^+e^- \rightarrow \mu^+\mu^-\gamma$  samples have relatively low background.

The first step of using  $e^+e^- \rightarrow \mu^+\mu^-\gamma$  are using the "ntuples"(the collection of samples) for both Data and Simulation(MC) in about the same range of period and

	Default	After Track Correction	Correction $+\sigma_{trk\ eff}$	Correction $-\sigma_{trk\ eff}$
$M \rho(\text{GeV})$	$0.7744 \pm 0.0002$	$0.7743(-0.0001)$	$0.7743(-0.0001)$	$0.7743(-0.0001)$
$\Gamma \rho(\text{GeV})$	$0.1499 \pm 0.0003$	$0.1500(0.0001)$	$0.1500(0.0001)$	$0.1500(0.0001)$
$M \rho'(\text{GeV})$	$1.2983 \pm 0.0024$	$1.2981(-0.0002)$	$1.2981(-0.0002)$	$1.2981(-0.0002)$
$\Gamma \rho'(\text{GeV})$	$0.5012 \pm 0.012$	$0.5015(0.0003)$	$0.5015(0.0003)$	$0.5015(0.0003)$
$M \rho''(\text{GeV})$	$1.6524 \pm 0.0068$	$1.6521(-0.0003)$	$1.6521(-0.0003)$	$1.6521(-0.0003)$
$\Gamma \rho''(\text{GeV})$	$0.2453 \pm 0.0362$	$0.2455(0.0002)$	$0.2455(0.0002)$	$0.2455(0.0002)$
$\beta$	$0.088 \pm 0.012$	$0.088(0.000)$	$0.088(-0.000)$	$0.088(-0.000)$
$\gamma$	$0.058 \pm 0.008$	$0.057(-0.001)$	$0.057(-0.001)$	$0.057(-0.001)$
$ \phi_\beta (\text{degree})$	$118.3 \pm 8.2$	$118.2(-0.1)$	$118.2(-0.1)$	$118.2(-0.1)$
$ \phi_\gamma (\text{degree})$	$58.9 \pm 8.2$	$58.8(-0.1)$	$58.8(-0.1)$	$58.8(-0.1)$
$a_\mu^{\pi\pi}(10^{-10})$	458.80	458.98	458.98	458.98
$\Delta a_\mu^{\pi\pi}(10^{-10})$		0.18	0.18	0.18

Tab. X.1: Parameters after Track Efficiency correction. The number in parentheses are only statistical errors.

condition. The ntuples are created in RELEASE 18 from Run 1 to Run 5. The data are from AllEvents skim list. The ntuples are created by requiring exactly 2 tracks in the final products of every event. A kinematic fit of the two muons to the beam spot with constraint that the missing momentum must have  $m = 0$  is performed, and a cut on the fit probability is applied. The detail of the algorithm can be found in [77].

After ntuples are created, one need to reconstruct photon variables ( $E_\gamma, \theta_\gamma, \phi_\gamma$ ) from the tracks information. Then, one can reconstruct the photon detection efficiency of Data and MC, by comparing the number of expected photons(reconstructed photon from the 2 tracks) and the number of photons detected in BABAR detector on some ranges of photon energy. The ratio of efficiency Data and MC is taken as the photon efficiency correction factor that needs to be applied to MC. To propagate to  $\pi^0$  correction factor, we multiply the correction factors from 2 photons.

This analysis made a ratio table of efficiency Data and MC, with efficiency defined as the number of photons detected divided by the number of photons expected(reconstructed from tracks) as a function of their energies. After fitting the numbers in the table with a linear function, we get a correction function( $f(x) = a + b.x$ , where  $x$  defined as photon momentum,  $P_\gamma$ ) that can be used to correct photon efficiency in rho samples. The result of this study is in X.1.

We take the differences of central values(such as  $a_\mu^{\pi\pi}, M_\rho$ , etc.) between before and after correction as the systematic uncertainty of  $\pi^0$  efficiency. The  $a_\mu^{\pi\pi}$  systematic uncertainty is relatively low due to the fact the calculation of  $a_\mu^{\pi\pi}$  depends only the shape of  $\pi^-\pi^0$  spectrum, which weakly depend on  $\pi^0$  efficiency uncertainty.

One important fact that the value  $a_\mu^{\pi\pi}$  is taken after the spectrum normalized by the total number of selected events

$$\left( \frac{N_i}{N_{TOTAL}} \right), \quad (\text{X.1})$$

$N_i$  = number of events at bin i,

$N_{TOTAL}$  = number of events from all of the bins,

and this may make  $a_\mu^{\pi\pi}$  less dependant to  $\pi^0$  Efficiency.

It is important that MC samples of  $\mu\mu\gamma$  can simulate tracks information that recorded in the detector properly. To check it, we plot the momentum and polar angle of tracks for both Data and MC (see plots X.2 and X.3). We didn't try to separate the samples based on their charges( $\mu^+$  and  $\mu^-$ ) and Run periods(Run 1 - Run 5). From these plots, we can see reasonable agreement between Data and MC.

### 2.3 $\pi^0$ Reconstruction

One can reconstruct invariant  $\pi^0$  mass using the information of energy from exactly 2 photons( $E_{\gamma 1}, E_{\gamma 2}$  and their opening angle, the angle between 2 photons from  $\pi^0$  decay). We study the opening angle of two gammas to understand how well one simulate MC to match Data.

We plot the opening angle of 2 photons in LAB frame as a function of Cosine  $\psi$  (opening angle) after all cuts applied. Three plots are presented coresponding to different ranges of Cosine  $\psi$ . Figure X.6 shows that the difference between the opening angle of Data and MC are negligible. Please check the plots in Figure X.6. In addition, we also compare the MC opening angle before and after  $\pi^0$  efficiency correction applied(see Figure X.7). There are no significant difference between MC opening angle before and after  $\pi^0$  efficiency correction applied.

Due to the fact the neutral efficiency correction improves the agreement between Data and MonteCarlo (see Figure X.5 and X.7), we shift all of the central values to the values after neutral efficiency correction and leaving all systematic uncertainties unchanged(because only tiny shift in central values).

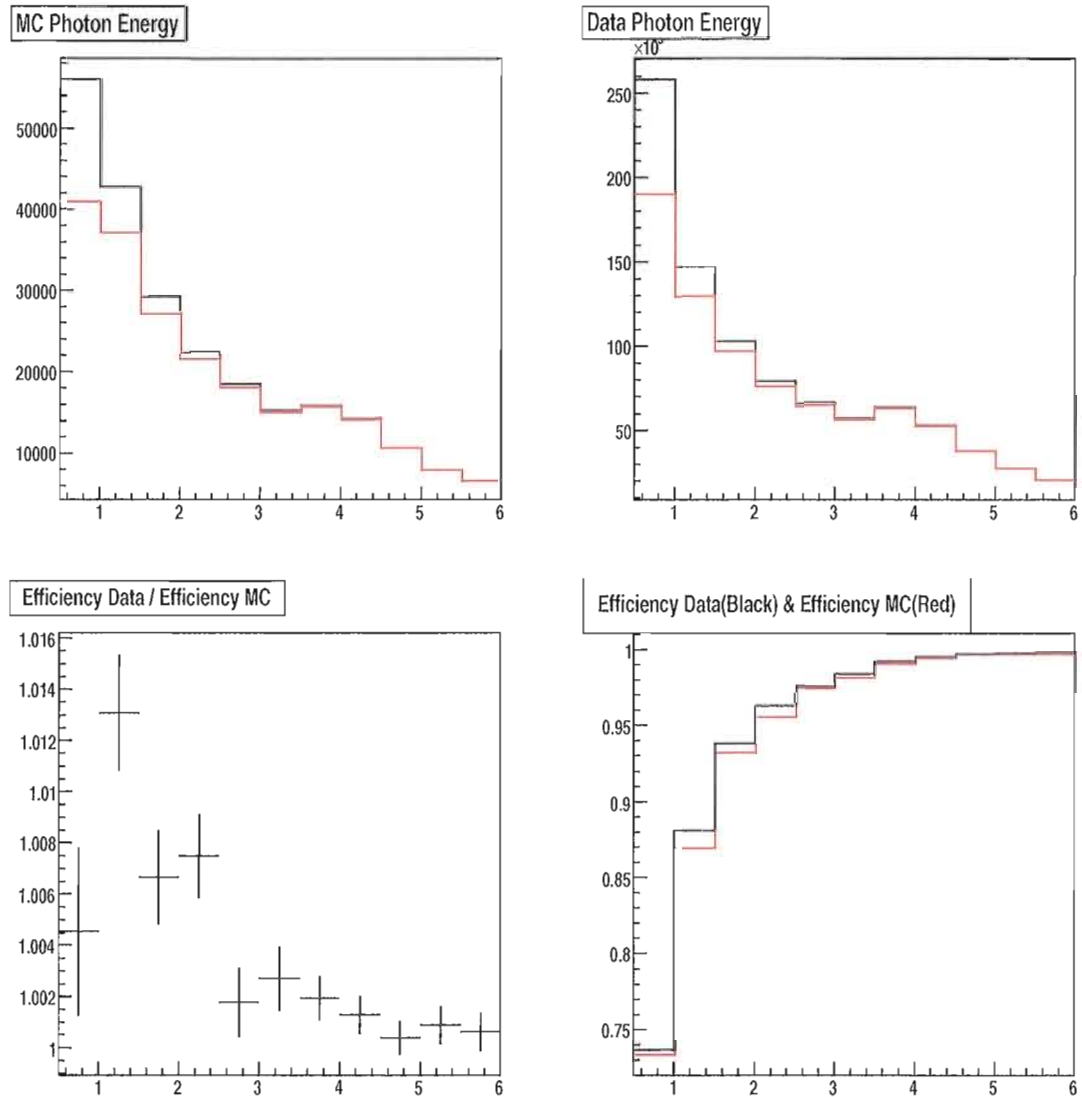


Fig. X.1: The upper left plot is the comparison between Reconstructed(black) and Detected(red)  $E_{\gamma}^{MC}$ . The upper right plot is the comparison between Reconstructed(black) and Detected(red)  $E_{\gamma}^{Data}$ . The lower right plot is the comparison between efficiency of Data(black) and MC(red). The lower left plot is the the ratio between efficiency Data and MC.

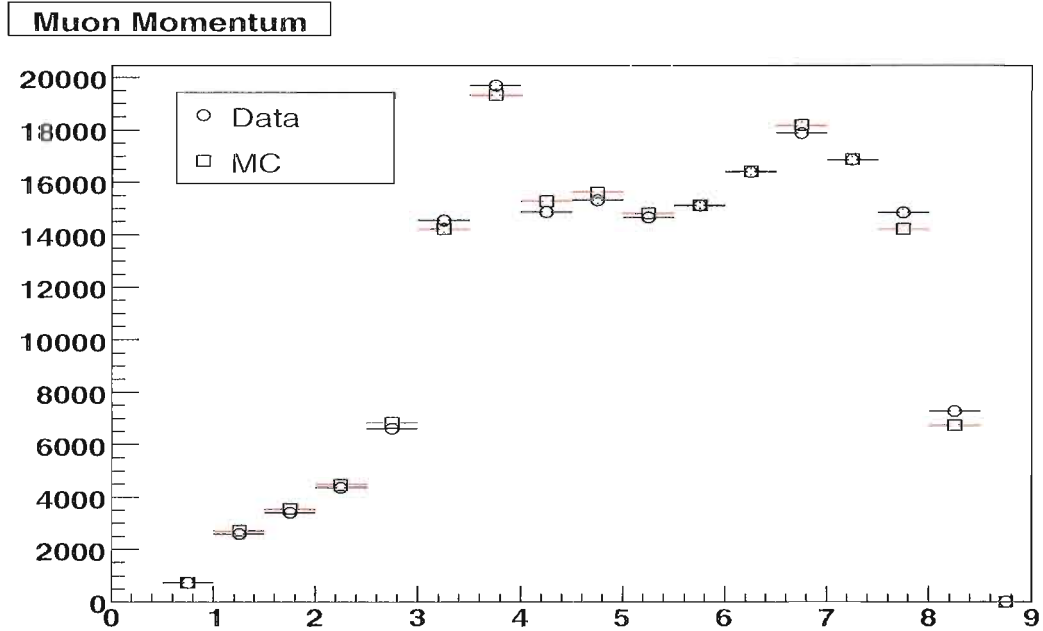


Fig. X.2: Comparison of Muon Momentum between Data(circle) and MC(square) from  $e^+e^- \rightarrow \mu^+\mu^-\gamma$  samples. MC is normalized to Data Luminosity

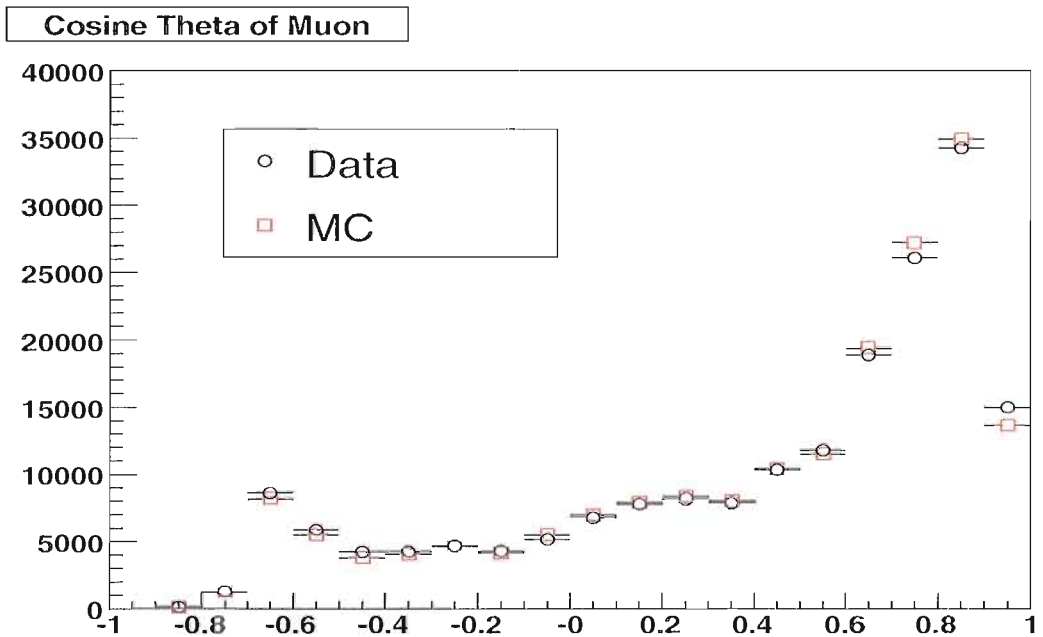


Fig. X.3: Comparison of Cosine Theta(LAB) of Muon between Data(circle) and MC(square) from  $e^+e^- \rightarrow \mu^+\mu^-\gamma$  samples. MC is normalized to Data Luminosity

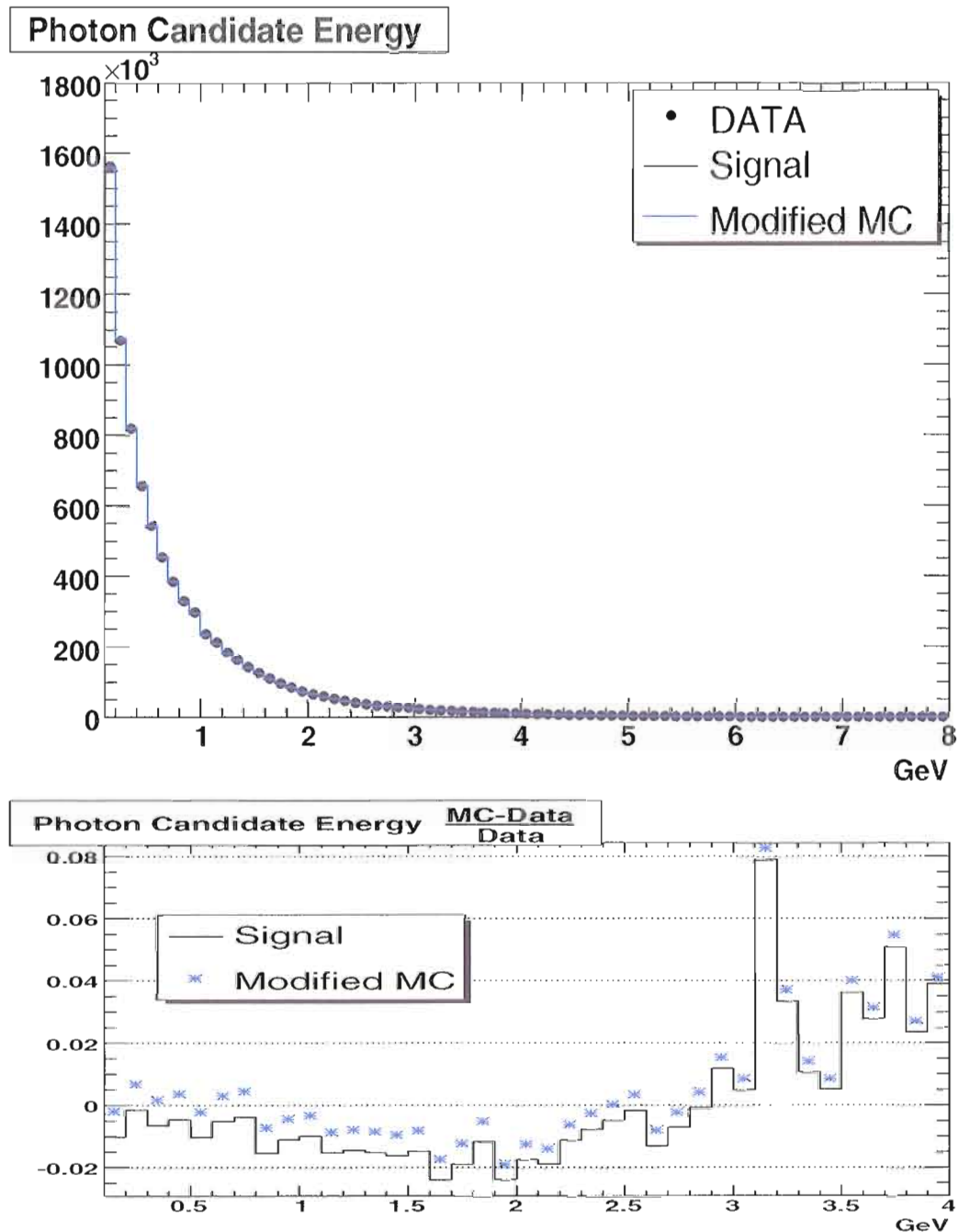


Fig. X.4: Comparison between selected photon energy Data, MC and Corrected-MC. Corrected MC is MC after photon efficiency correction applied which calculated using  $\mu\mu\gamma$  sample. Both MCs are normalized to Data Luminosity.

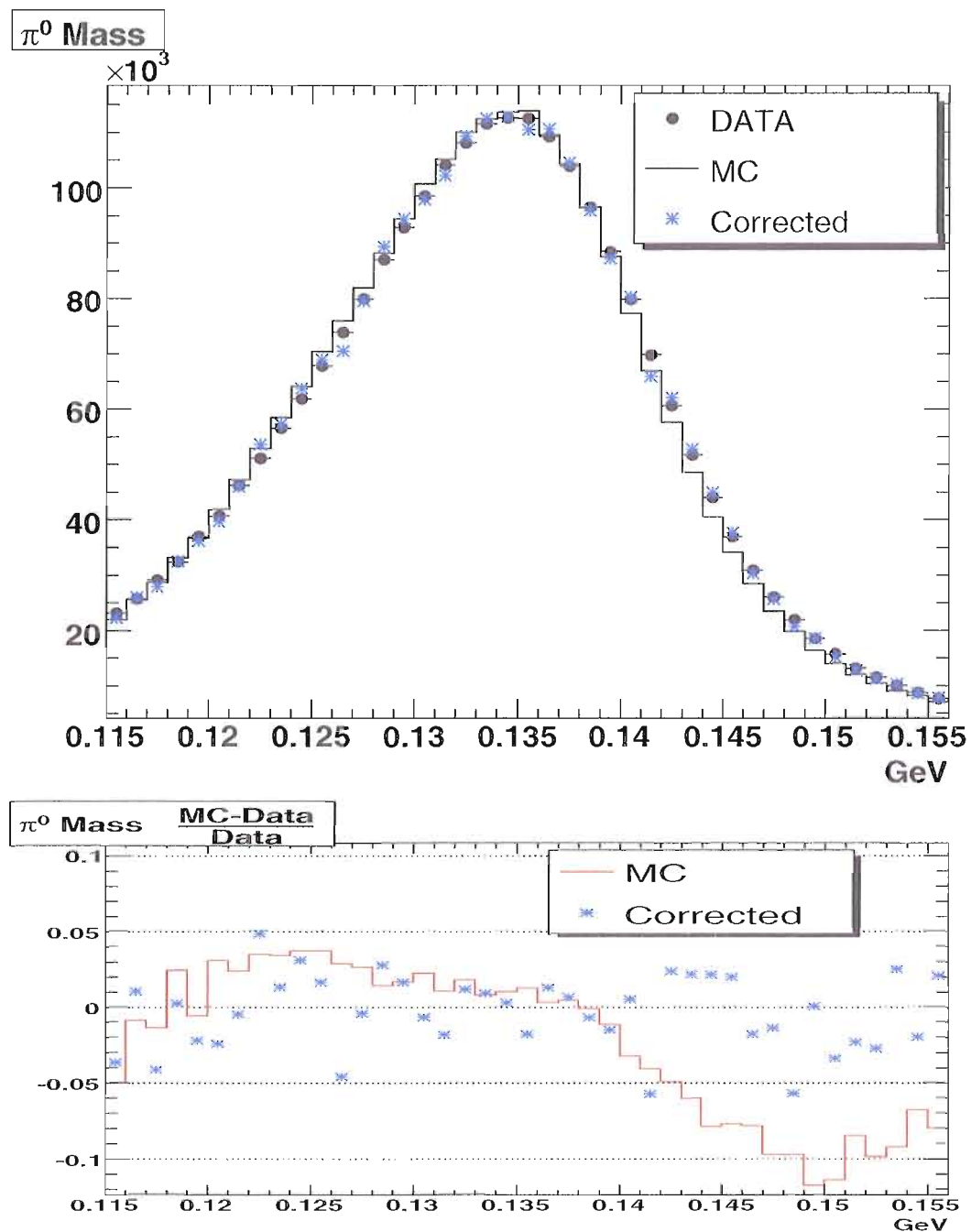


Fig. X.5: Comparison between selected  $M_{\gamma\gamma}$  of Data, MC and Corrected-MC. Both MCs are normalized to Data Luminosity. Corrected MC is MC after photon efficiency correction which calculated using  $\mu\mu\gamma$  sample.

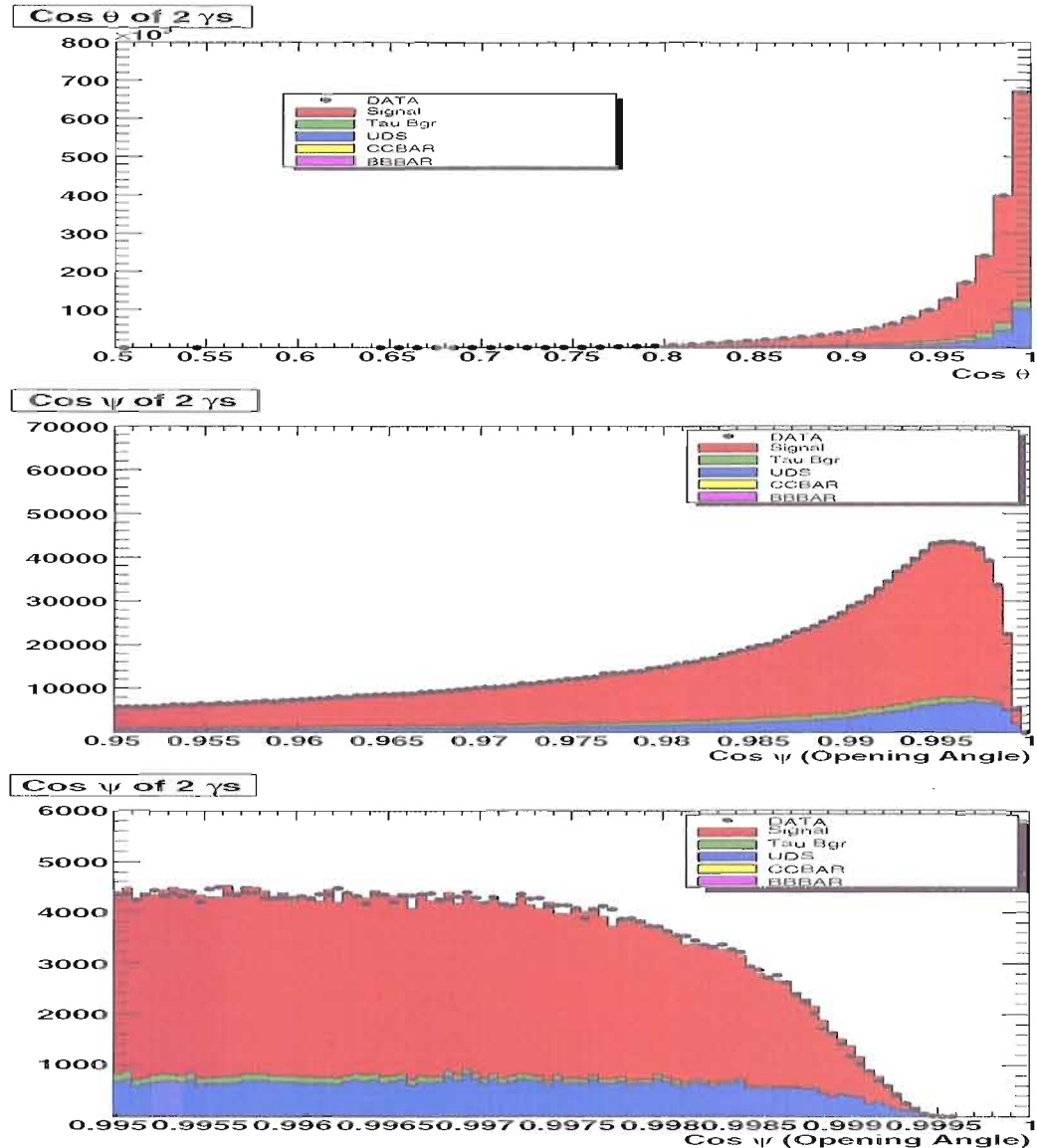


Fig. X.6: The Cosine of Opening Angle between 2 photons of  $\pi^0$  in LAB frame after all selection cuts applied. From top to bottom, the plots are zoomed. Top plot ranges from 0.5-1, Mid plot ranges from 0.95-1 and Bottom plot ranges from 0.995-1. MC is normalized to Data Luminosity.

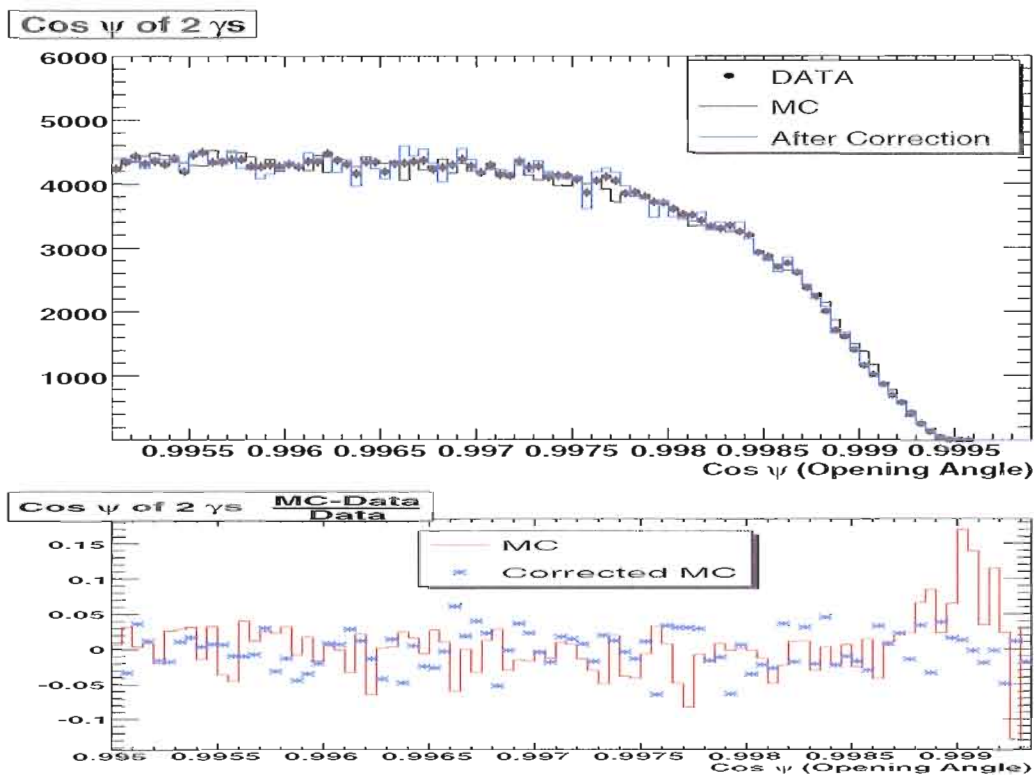


Fig. X.7: The opening angle of selected 2 photons of  $\pi^0$  decay(LAB frame) after all selection cuts applied. Corrected MC is MC after photon efficiency correction which calculated using  $\mu\mu\gamma$  sample.

	Default	$\pi^0$ Eff Correction	$a - \sigma_a, b - \sigma_b$	$a - \sigma_a, b + \sigma_b$	$a + \sigma_a, b - \sigma_b$	$a + \sigma_a, b + \sigma_b$
M $\rho$ (GeV)	$0.7744 \pm 0.0002$	$0.7745(0.0001)$	$0.7745(0.0001)$	$0.7745(0.0001)$	$0.7745(0.0001)$	$0.7745(-0.0001)$
$\Gamma\rho$ (GeV)	$0.1499 \pm 0.0003$	$0.1493(-0.0006)$	$0.1494(-0.005)$	$0.1495(-0.0005)$	$0.1492(-0.0007)$	$0.1493(0.0006)$
M $\rho'$ (GeV)	$1.2983 \pm 0.0024$	$1.2993(0.0010)$	$1.2992(0.0009)$	$1.2991(0.0008)$	$1.2995(0.0012)$	$1.2994(0.0011)$
$\Gamma\rho'$ (GeV)	$0.5012 \pm 0.012$	$0.4990(-0.0022)$	$0.4999(-0.0013)$	$0.4996(-0.0016)$	$0.4985(-0.0027)$	$0.4988(-0.0024)$
M $\rho''$ (GeV)	$1.6524 \pm 0.0068$	$1.6614(0.0090)$	$1.6610(0.0086)$	$1.6605(0.0081)$	$1.6623(0.0099)$	$1.6617(0.0093)$
$\Gamma\rho''$ (GeV)	$0.2453 \pm 0.0362$	$0.2433(-0.0020)$	$0.2436(-0.0019)$	$0.2435(-0.0018)$	$0.2431(-0.0022)$	$0.2432(-0.0021)$
$\beta$	$0.088 \pm 0.012$	$0.090(0.002)$	$0.090(0.002)$	$0.090(0.002)$	$0.090(0.002)$	$0.090(0.002)$
$\gamma$	$0.058 \pm 0.008$	$0.060(0.002)$	$0.060(0.002)$	$0.060(0.002)$	$0.060(0.002)$	$0.060(0.002)$
$ \phi_\beta $ (degree)	$118.3 \pm 8.2$	$118.9(0.6)$	$118.8(0.5)$	$118.8(0.5)$	$118.9(0.6)$	$118.9(0.6)$
$ \phi_\gamma $ (degree)	$58.9 \pm 8.2$	$59.4(0.5)$	$59.4(0.5)$	$59.4(0.5)$	$59.4(0.5)$	$59.4(0.5)$
$a_\mu^{\pi\pi}(10^{-10})$	458.80	458.45	458.47	458.48	458.42	459.43
$\Delta a_\mu^{\pi\pi}(10^{-10})$		0.35	0.33	0.32	0.38	0.37

Tab. X.2: Fitting parameters before and after linear  $\pi^0$  efficiency correction. We also include the uncertainties of  $a(\sigma_a)$  and  $b(\sigma_b)$ , by varying their  $1\sigma$  up and down. The number in parentheses are only statistical errors.

### 3 Resolution

#### 3.1 Tracking Resolution

One can use  $e^+e^- \rightarrow \mu^+\mu^-\gamma$  to study charge track resolution. To estimate the tracking resolution uncertainty, we vary our MC samples using the correction factors derived from  $e^+e^- \rightarrow \mu^+\mu^-\gamma$  study [75]. Taking the difference between initial and after resolution correction values as our systematic uncertainties, we found that only P(momentum) and  $\theta$ (theta) resolutions are quite significant sources of uncertainties, while  $\phi$ (phi) resolution contributes negligible uncertainty. The result of this study is in Table X.3 and X.4.

#### 3.2 Photon Resolution

The control sample of  $e^+e^- \rightarrow \mu^+\mu^-\gamma$  ntuples are taken to study neutral resolution.

This analysis takes the ratio of  $E_\gamma^{expected}$  (reconstructed from  $\mu^+$  and  $\mu^-$  information) and  $E_\gamma^{detected}$  variables(energy and angles). The measurement are done in the LAB frame for both Data and MonteCarlo samples. We divide the samples based on their Runs periods(Run 1 - Run 5). Using this information we can get mean ratio( $R_{MEAN}$ ) and width( $\sigma_{smearing}$ ) of Data and MonteCarlo, which we define as:

$$R_{MEAN} = \frac{MEAN\left(\frac{E_\gamma^{expectedDATA}}{E_\gamma^{detectedDATA}}\right)}{MEAN\left(\frac{E_\gamma^{expectedMC}}{E_\gamma^{detectedMC}}\right)}, \quad (X.2)$$

and

$$\sigma_{smearing} = \sqrt{\sigma_{Data}^2 - \sigma_{MC}^2}. \quad (X.3)$$

If we have a perfect detector, the energy ratio of  $R_{MEAN}$  is equal to one. In fact, we get the distribution of ratio that centered about 1. We fit this ratio distribution

	Default	$\theta$ Correction	$\theta$ Correction $-\sigma_\theta$	$\theta$ Correction $+\sigma_\theta$
$M \rho(\text{GeV})$	$0.7744 \pm 0.0002$	$0.7744(0.0000)$	$0.7744(0.0000)$	$0.7744(0.0000)$
$\Gamma \rho(\text{GeV})$	$0.1499 \pm 0.0003$	$0.1500(0.0001)$	$0.1500(0.0001)$	$0.1500(0.0001)$
$M \rho'(\text{GeV})$	$1.2983 \pm 0.0024$	$1.2982(-0.0001)$	$1.2982(-0.0001)$	$1.2982(-0.0001)$
$\Gamma \rho'(\text{GeV})$	$0.5012 \pm 0.012$	$0.5013(0.0001)$	$0.5013(0.0001)$	$0.5013(0.0001)$
$M \rho''(\text{GeV})$	$1.6524 \pm 0.0068$	$1.6522(-0.0002)$	$1.6522(-0.0002)$	$1.6522(-0.0002)$
$\Gamma \rho''(\text{GeV})$	$0.2453 \pm 0.0362$	$0.2455(0.0002)$	$0.2455(0.0002)$	$0.2455(0.0002)$
$\beta$	$0.088 \pm 0.012$	$0.087(-0.001)$	$0.0857(-0.001)$	$0.0857(-0.001)$
$\gamma$	$0.058 \pm 0.008$	$0.057(-0.001)$	$0.057(-0.001)$	$0.057(-0.001)$
$ \phi_\beta (\text{degree})$	$118.3 \pm 8.2$	$118.1(-0.2)$	$118.1(-0.2)$	$118.1(-0.2)$
$ \phi_\gamma (\text{degree})$	$58.9 \pm 8.2$	$58.8(-0.1)$	$58.8(-0.1)$	$58.8(-0.1)$
$a_\mu^{\pi\pi}(10^{-10})$	458.80	458.87	458.87	458.87
$\Delta a_\mu^{\pi\pi}(10^{-10})$		0.07	0.07	0.07

Tab. X.3: GS Fitting Parameters after  $\theta_{track}$  resolution correction. The number in parentheses are only the statistical errors.

	Default	$P_{scale}$ correction	$P_{res}$ correction	$P_{scale}$ & $P_{res}$ Correction
$M \rho(\text{GeV})$	$0.7744 \pm 0.0002$	$0.7742(-0.0002)$	$0.7745(0.0001)$	$0.7744(0.0000)$
$\Gamma\rho(\text{GeV})$	$0.1499 \pm 0.0003$	$0.1499(0.0000)$	$0.1501(0.0002)$	$0.1501(0.0002)$
$M \rho'(\text{GeV})$	$1.2983 \pm 0.0024$	$1.2982(-0.0003)$	$1.2984(0.0001)$	$1.2982(-0.0001)$
$\Gamma\rho'(\text{GeV})$	$0.5012 \pm 0.012$	$0.5012(0.0000)$	$0.5014(0.0002)$	$0.5014(0.0002)$
$M \rho''(\text{GeV})$	$1.6524 \pm 0.0068$	$1.6520(-0.0004)$	$1.6526(0.0002)$	$1.6522(-0.0002)$
$\Gamma\rho''(\text{GeV})$	$0.2453 \pm 0.0362$	$0.2455(0.0002)$	$0.2457(0.0004)$	$0.2458(0.0005)$
$\beta$	$0.088 \pm 0.012$	$0.088(0.000)$	$0.0857(-0.001)$	$0.0857(-0.001)$
$\gamma$	$0.058 \pm 0.008$	$0.058(0.000)$	$0.057(-0.001)$	$0.057(-0.001)$
$ \phi_\beta (\text{degree})$	$118.3 \pm 8.2$	$118.1(-0.2)$	$118.4(0.1)$	$118.1(-0.2)$
$ \phi_\gamma (\text{degree})$	$58.9 \pm 8.2$	$58.8(-0.1)$	$58.9(0.0)$	$58.8(-0.1)$
$a_\mu^{\pi\pi}(10^{-10})$	458.80	458.96	458.88	458.98
$\Delta a_\mu^{\pi\pi}(10^{-10})$		0.16	0.08	0.18

Tab. X.4: GS Fitting Parameters after  $P_{track}$  resolution correction. The number in parentheses are only statistical errors.

using Crystal Ball function, which gives us Mean and Width of ratio distribution. Crystal Ball, a function named after Crystal Ball Collaboration, is a Gaussian with a tail one side. One advantage of Crystal Ball function is because this function is included in RooFit package. We compare it for both Data and MC to understand how good MC can simulate real data.

Using Equations X.2 and X.3, we can smear our MonteCarlo generally (with assumptions that variation Run by Run is small).

$$E_{MC}^{modified} = E_{MC}^{initial} * R_{MEAN}, \quad (\text{X.4})$$

Second step, increase the MC energy resolution using:

$$E_{MC}^{modified} = E_{MC}^{initial} * [gRandom \rightarrow Gaus(1, \sigma_{smearing})]. \quad (\text{X.5})$$

Note:  $[gRandom \rightarrow Gaus(1, \sigma_{smearing})]$  is a ROOT function that return random numbers which have gaussian distribution with mean 1 and width  $\sigma_{smearing}$ .

The photon energy resolution uncertainty of x(central values) is:

$$\sigma_{\gamma \text{ resolution}} = \frac{x^{\text{after smearing}} - x^{\text{before smearing}}}{x^{\text{before smearing}}}. \quad (\text{X.6})$$

In applying the shift and smearing procedure, we use a general correction, that independent from Run periods. The same strategy will be applied to theta( $\theta$ ) and phi( $\phi$ ) resolution, but with Gaussian fitting. The result of this study is in Table X.5. Many plots that related to photon resolution study can be found in Appendix A: Section 1 for photon energy( $E_\gamma$ ), Section 2 for photon polar angle( $\theta_\gamma$ ) and Section 3 for photon azimuthal angle( $\phi_\gamma$ ).

	Default	Shift E	Smear E	Combi E	$\theta$ Smearing	$\phi$ Smearing
$M\rho(\text{GeV})$	$0.7744 \pm 0.0002$	$0.7740(-0.0004)$	$0.7746(0.0002)$	$0.7741(-0.0003)$	$0.7746(0.0002)$	$0.7743(-0.0001)$
$\Gamma\rho(\text{GeV})$	$0.1499 \pm 0.0003$	$0.1496(-0.0003)$	$0.1491(-0.0008)$	$0.1492(-0.0007)$	$0.1451(0.0002)$	$0.1498(-0.0001)$
$M\rho'(\text{GeV})$	$1.2983 \pm 0.0024$	$1.2967(-0.0016)$	$0.1294(0.0011)$	$1.2969(-0.0014)$	$1.2990(0.0007)$	$1.2981(-0.0002)$
$\Gamma\rho'(\text{GeV})$	$0.5012 \pm 0.012$	$0.4982(-0.0030)$	$0.4964(-0.0048)$	$0.4962(-0.0050)$	$0.5018(0.0006)$	$0.5009(-0.0003)$
$M\rho''(\text{GeV})$	$1.6524 \pm 0.0068$	$1.6422(-0.0102)$	$1.6545(0.0021)$	$1.6425(-0.0099)$	$1.6569(0.0045)$	$1.6519(-0.0005)$
$\Gamma\rho''(\text{GeV})$	$0.2453 \pm 0.0362$	$0.2430(-0.0023)$	$0.2414(-0.0039)$	$0.2418(-0.0035)$	$0.2468(0.0015)$	$0.2450(-0.0003)$
$\beta$	$0.088 \pm 0.012$	$0.090(0.002)$	$0.087(-0.001)$	$0.089(0.001)$	$0.089(0.001)$	$0.087(-0.01)$
$\gamma$	$0.058 \pm 0.008$	$0.060(0.002)$	$0.059(0.001)$	$0.060(0.002)$	$0.059(0.01)$	$0.057(-0.01)$
$ \phi_\beta (\text{degree})$	$118.3 \pm 8.2$	$119.0(0.7)$	$117.8(-0.5)$	$118.9(0.6)$	$118.6(0.3)$	$118.0(-0.3)$
$ \phi_\gamma (\text{degree})$	$58.9 \pm 8.2$	$59.5(0.6)$	$58.6(-0.3)$	$59.4(0.5)$	$59.2(0.3)$	$58.5(-0.4)$
$a_\mu^{\pi\pi}(10^{-10})$	458.80	458.34	458.43	458.49	458.95	458.72
$\Delta a_\mu^{\pi\pi}(10^{-10})$		-0.46	-0.37	-0.31	0.15	-0.08

Tab. X.5: Photon Resolution Uncertainties. The numbers in parentheses are only statistical errors.

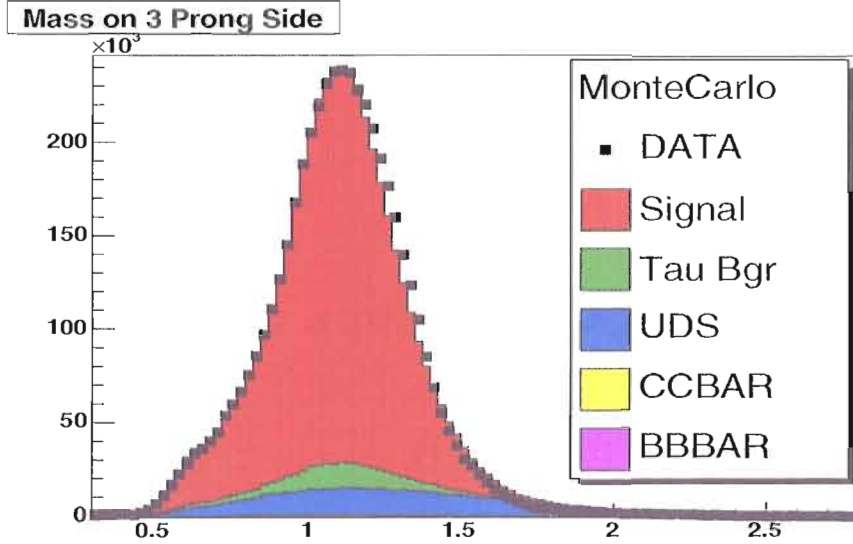


Fig. X.8: The total mass on the 3 Prong side(tag side), assuming the 3 tracks are pions after all cuts applied, x axis is in GeV. MC is normalized to Data Luminosity.

## 4 Backgrounds

### 4.1 $q\bar{q}$ Background

One type of major backgrounds from  $q\bar{q}$  is uds (jets from u, d, and s quarks). We can study this type of background by counting the number of events in  $\pi^-\pi^0$  invariant mass - above nominal  $\tau$  mass(at this range of mass, the contribution from  $\tau$  decays is small compared to uds). By calculating the ratio of the events in reconstructed  $\rho$  mass between MonteCarlo and Data above  $\tau$  mass, we get 1.048, and conservatively we assign 5% uncertainties from non-tau background. We add(reduce) by this number the contribution of uds to the invariant  $\pi^-\pi^0$  mass and then refit the invariant  $\pi^-\pi^0$  mass using Gounaris-Sakurai function. Taking the maximum difference between initial and after-correction values as the uncertainty The result of this study is in Table X.6.

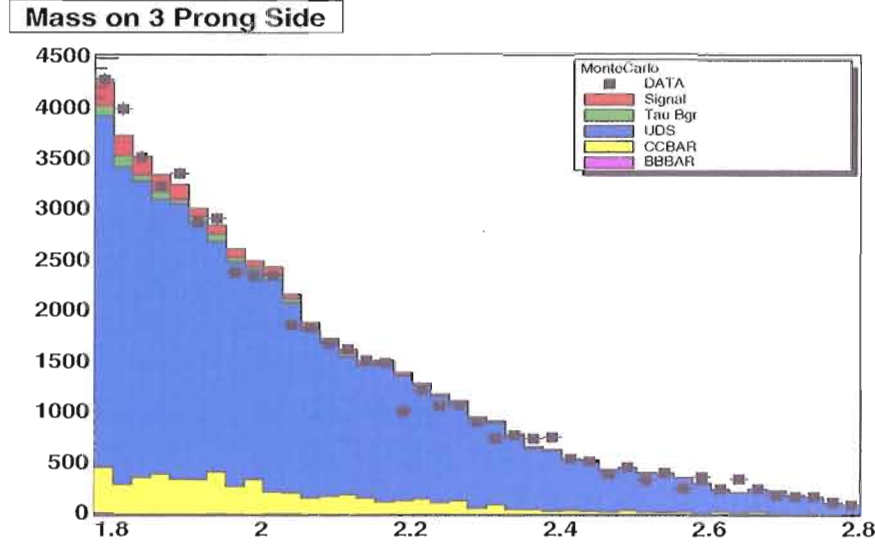


Fig. X.9: The total mass on the 3 Prong side above tau Mass, assuming the 3 tracks are pions after all cuts applied, x axis is in GeV

	Default	$+\sigma_{uds}$	$-\sigma_{uds}$
$M \rho(\text{GeV})$	$0.7744 \pm 0.0002$	$0.7745(0.0001)$	$0.7744(-0.0001)$
$\Gamma \rho(\text{GeV})$	$0.1499 \pm 0.0003$	$0.1498(-0.0001)$	$0.1500(0.0001)$
$M \rho'(\text{GeV})$	$1.2983 \pm 0.0024$	$1.2986(0.0003)$	$1.2980(-0.0003)$
$\Gamma \rho'(\text{GeV})$	$0.5012 \pm 0.012$	$0.5010(-0.0002)$	$0.5014(0.0002)$
$M \rho''(\text{GeV})$	$1.6524 \pm 0.0068$	$1.6528(0.0004)$	$1.6520(-0.0004)$
$\Gamma \rho''(\text{GeV})$	$0.2453 \pm 0.0362$	$0.2538(-0.0005)$	$0.2548(0.0005)$
$\beta$	$0.088 \pm 0.012$	$0.087(-0.001)$	$0.089(0.001)$
$\gamma$	$0.058 \pm 0.008$	$0.057(-0.001)$	$0.059(0.001)$
$ \phi_\beta (\text{degree})$	$118.3 \pm 8.2$	$118.5(0.2)$	$118.1(-0.2)$
$ \phi_\gamma (\text{degree})$	$58.9 \pm 8.2$	$59.0(0.1)$	$58.8(-0.1)$
$a_\mu^{\pi\pi}(10^{-10})$	458.82	458.57	459.02
$\Delta a_\mu^{\pi\pi}(10^{-10})$		-0.23	0.22

Tab. X.6: We estimate the contribution of uds background uncertainty using the ratio of Data and MC above tau mass ( 1.8 GeV). After varying the uds background contribution by its uncertainty  $\pm\sigma$ , we refit the spectrum using GS function. This table shows the parameters before(default values) and after uds background variation. The numbers in parentheses are only statistical errors.

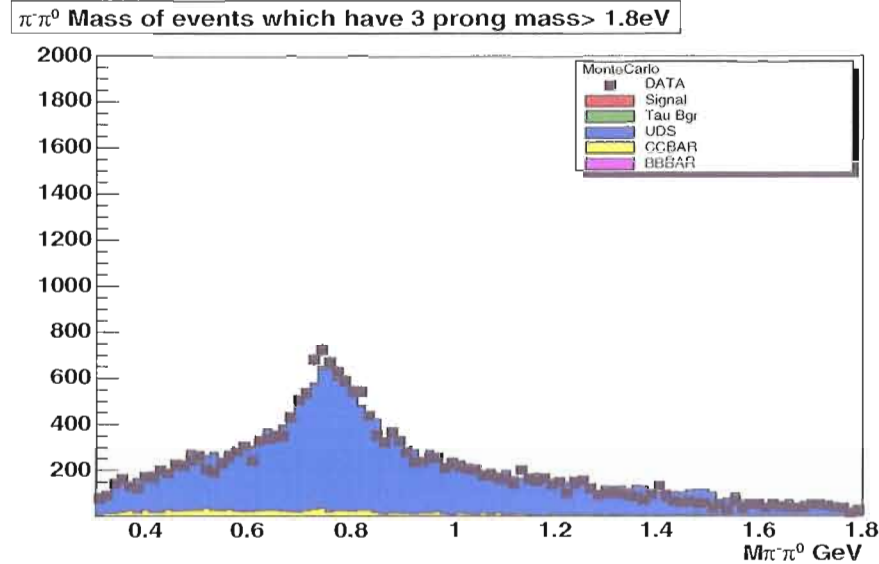


Fig. X.10: The Signal  $\pi^-\pi^0$  invariant mass of some events which have total mass on 3 prong side bigger than 1.8 GeV (Log Scale).

## 4.2 $\tau$ Background

$\tau$  background is background constructed from other tau decay channels, not from signal ( $\tau \rightarrow \pi^-\pi^0\nu_\tau$ ). There are 6 decay modes that dominate  $\tau$  background:

- $\tau^- \rightarrow a_1^- \rightarrow \pi^-\pi^0\pi^0\nu_\tau$ ,
- $\tau^- \rightarrow K^{*-} \rightarrow K^-\pi^0\nu_\tau$ ,
- $\tau^- \rightarrow e^-\nu_e\nu_\tau$ ,
- $\tau^- \rightarrow \pi^-\nu_\tau$ ,
- $\tau^- \rightarrow K^-K^0\pi^0\nu_\tau$ ,
- $\tau^- \rightarrow \pi^-K^0\nu_\tau$

$\tau$  background is dominated by the decay  $\tau^- \rightarrow \pi^-\pi^0\pi^0\nu_\tau$  (55.22%), followed by  $\tau^- \rightarrow K^{*-}\nu_\tau$  (28.77%).

The overall estimated BF systematic uncertainty due to the errors in the branching fraction of the  $\tau$  background events surviving all the cuts is given by:

$$\sigma^{\tau-bgr} = \sqrt{\sum_i \left( w_i \frac{\sigma_i^{PDG}}{BF_i^{PDG}} \right)^2}, \quad (\text{X.7})$$

where  $w_i$  is the weight of the tau background mode  $i$ , that is the fraction of the selected events of mode  $i$  in the total number of selected events.  $BF_i^{PDG}$  is the branching fraction and  $\sigma_i^{PDG}$  is the uncertainty of decay mode  $i$  from PDG 2007.

In the table below, we quote some significant  $\tau$  backgrounds, the left column shows the  $\tau$  modes (charge conjugate is implied) and the right column is its contribution to the total  $\tau$  background (in percentage). The results of this study are in Tables [X.8],[X.9],[X.10],[X.11],[X.11],[X.12],[X.13],[X.14] and [X.15].

Decay Mode	Contribution to $\tau$ Background (%)	$w_i(/10^{-4})$	$\frac{\sigma^{PDG}}{Br^{PDG}}(\%)$
$\tau^- \rightarrow e^- \nu_\tau \nu_e$	1.71	4.91	0.34
$\tau^- \rightarrow \mu^- \nu_\tau \nu_\mu$	0.24	0.69	0.34
$\tau^- \rightarrow \pi^- \nu_\tau$	2.83	8.12	0.99
$\tau^- \rightarrow \pi^- \pi^0 \pi^0 \nu_\tau$	55.22	158.48	1.53
$\tau^- \rightarrow K^- \nu_\tau$	0.22	0.63	3.35
$\tau^- \rightarrow 2\pi^- \pi^+ \nu_\tau$	0.05	0.54	1.10
$\tau^- \rightarrow 2\pi^- \pi^+ \pi^0 \nu_\tau$	0.58	1.66	2.06
$\tau^- \rightarrow \pi^- 3\pi^0 \nu_\tau$	0.71	2.04	9.26
$\tau^- \rightarrow K^0 K^- \nu_\tau$	0.31	0.89	10.39
$\tau^- \rightarrow K^- \bar{K}^0 \pi^0 \nu_\tau$	1.81	5.19	12.90
$\tau^- \rightarrow K^- 2\pi^0 \nu_\tau$	0.39	1.12	39.66
$\tau^- \rightarrow \pi^- K^0 \pi^0 \nu_\tau$	6.00	17.22	4.49
$\tau^- \rightarrow \eta \pi^- \pi^0 \nu_\tau$	0.08	0.23	13.79
$\tau^- \rightarrow K^* \nu_\tau$	28.77	82.57	3.88

Tab. X.7: After cuts applied, the  $\tau$  backgrounds are reduced significantly. This table shows the main  $\tau$  decays that contributes to  $\tau$  Backgrounds after all cuts applied.

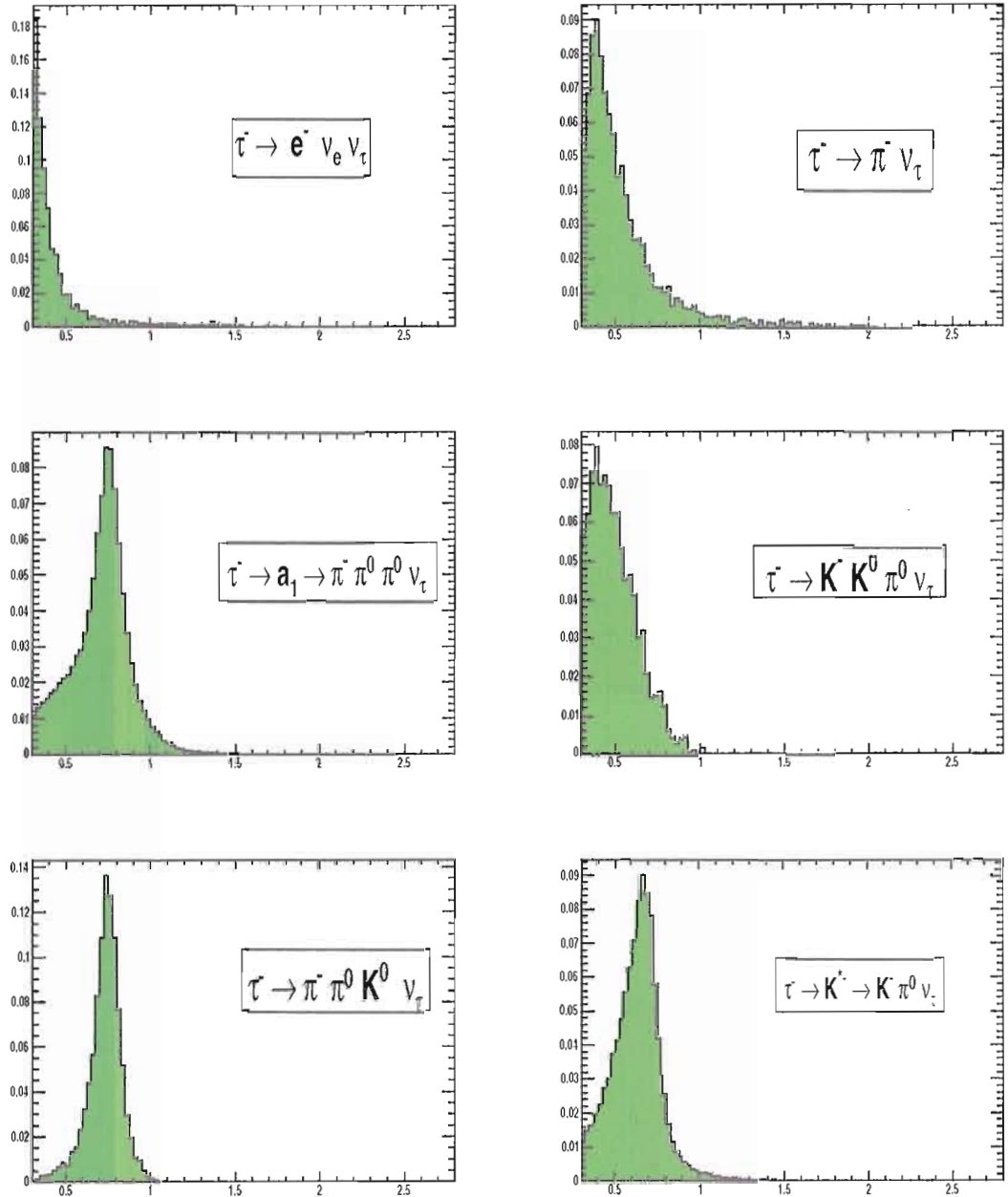


Fig. X.11: The invariant  $\pi^- \pi^0$  Mass from major contributors to  $\tau$  background, after all cuts applied. The horizontal line is in GeV

In this analysis, we study the uncertainty by varying the specific  $\tau$  decay mode by  $\pm 1\sigma$  (Branching Fraction uncertainty taken from PDG 2007). For all these modes,

we refit the invariant  $\pi^-\pi^0$  mass spectrum using Gounaris-Sakurai function, all of the fitting results are written in the tables below. The maximum difference between + and - values is taken as the uncertainty of a parameter, in a conservative way. Another method to assign uncertainty is taking the average of the absolute values of both differences (from + and - uncertainty variation), but we didn't use because this method gives lower uncertainty.

	Default	$+\sigma_{\tau^- \rightarrow e^- \nu_e \nu_\tau}$	$-\sigma_{\tau^- \rightarrow e^- \nu_e \nu_\tau}$
$M \rho(\text{GeV})$	$0.7744 \pm 0.0002$	$0.7744(0.0000)$	$0.7744(0.0000)$
$\Gamma\rho (\text{GeV})$	$0.1499 \pm 0.0003$	$0.1499(0.0000)$	$0.1499(0.0000)$
$M \rho'(\text{GeV})$	$1.2983 \pm 0.0244$	$1.2983(0.0000)$	$1.2983(0.0000)$
$\Gamma\rho'(\text{GeV})$	$0.5012 \pm 0.012$	$0.5012(0.0000)$	$0.5012(0.0000)$
$M \rho'(\text{GeV})'$	$1.6524 \pm 0.0068$	$1.6524(0.0000)$	$1.6524(0.0000)$
$\Gamma\rho'' (\text{GeV})$	$0.2453 \pm 0.0362$	$0.2543(0.0000)$	$0.2543(0.0000)$
$\beta$	$0.088 \pm 0.012$	$0.088(0.000)$	$0.088(0.000)$
$\gamma$	$0.058 \pm 0.008$	$0.058(0.000)$	$0.058(0.000)$
$ \phi_\beta (\text{degree})$	$118.3 \pm 8.2$	$118.3(0.0)$	$118.3(0.0)$
$ \phi_\gamma (\text{degree})$	$58.9 \pm 8.2$	$58.9(0.0)$	$58.9(0.0)$
$a_\mu^{\pi\pi}(10^{-10})$	458.80	458.80	458.80
$\Delta a_\mu^{\pi\pi}(10^{-10})$		0.00	0.00

Tab. X.8: Parameters after  $\tau^- \rightarrow e^- \nu_e \nu_\tau$  background variation. The number in parentheses are only statistical errors.

### The Study of A1( $\tau \rightarrow \pi^-\pi^0\pi^0\nu_\tau$ )

This analysis study the possibility that missing  $1\pi^0$  from the  $\tau \rightarrow \pi^-\pi^0\pi^0\nu_\tau$  decays can fake our signals.

Starting from equation :  $f(b, e) = 2be(1 - e)$

b = branching fraction of a1

e = efficiency of  $\pi^0$

2 because of  $2\pi^0$  involved in the process

	Default	$+\sigma_{\tau^- \rightarrow \pi^- \nu_\tau}$	$-\sigma_{\tau^- \rightarrow \pi^- \nu_\tau}$
M $\rho$ (GeV)	$0.7744 \pm 0.0002$	0.7744(0.0000)	0.7744(0.0000)
$\Gamma\rho$ (GeV)	$0.1499 \pm 0.0003$	0.1499(0.0000)	0.1499(0.0000)
M $\rho'$ (GeV)	$1.2983 \pm 0.0024$	1.2983(0.0000)	1.2983(0.0000)
$\Gamma\rho'$ (GeV)	$0.5012 \pm 0.012$	0.5012(0.0000)	0.5012(0.0000)
M $\rho''$ (GeV)	$1.6524 \pm 0.0068$	1.6524(0.0000)	1.6524(0.0000)
$\Gamma\rho''$ (GeV)	$0.2453 \pm 0.0362$	0.2543(0.0000)	0.2543(0.0000)
$\beta$	$0.088 \pm 0.012$	0.088(0.000)	0.088(0.000)
$\gamma$	$0.058 \pm 0.008$	0.058(0.000)	0.058(0.000)
$ \phi_\beta $ (degree)	$118.3 \pm 8.2$	118.3(0.0)	118.3(0.0)
$ \phi_\gamma $ (degree)	$58.9 \pm 8.2$	58.9(0.0)	58.9(0.0)
$a_\mu^{\pi\pi}(10^{-10})$	458.80	458.79	458.81
$\Delta a_\mu^{\pi\pi}(10^{-10})$		-0.01	0.01

Tab. X.9: Parameters after  $\tau^- \rightarrow \pi^- \nu_\tau$  background variation(MC Mode 3). The number in parentheses are only statistical errors.

	Default	$+\sigma_{\tau^- \rightarrow a_1 \rightarrow \pi^- \pi^0 \pi^0 \nu_\tau}$	$-\sigma_{\tau^- \rightarrow a_1 \rightarrow \pi^- \pi^0 \pi^0 \nu_\tau}$
M $\rho$ (GeV)	$0.7744 \pm 0.0002$	0.7744(0.0000)	0.7744(0.0000)
$\Gamma\rho$ (GeV)	$0.1499 \pm 0.0003$	0.1499(0.0000)	0.1499(0.0000)
M $\rho'$ (GeV)	$1.2983 \pm 0.0024$	1.2982(-0.0001)	1.2984(0.0001)
$\Gamma\rho'$ (GeV)	$0.5012 \pm 0.012$	0.5011(-0.0001)	0.5013(0.0001)
M $\rho''$ (GeV)	$1.6524 \pm 0.0068$	1.6522(-0.0002)	1.6526(0.0002)
$\Gamma\rho''$ (GeV)	$0.2453 \pm 0.0362$	0.2542(-0.0001)	0.2544(0.0001)
$\beta$	$0.088 \pm 0.012$	0.088(0.000)	0.088(0.000)
$\gamma$	$0.058 \pm 0.008$	0.058(0.000)	0.058(0.000)
$ \phi_\beta $ (degree)	$118.3 \pm 8.2$	118.3(0.0)	118.3(0.0)
$ \phi_\gamma $ (degree)	$58.9 \pm 8.2$	58.9(0.0)	58.9(0.0)
$a_\mu^{\pi\pi}(10^{-10})$	458.80	458.73	458.87
$\Delta a_\mu^{\pi\pi}(10^{-10})$		-0.07	0.07

Tab. X.10: Parameters after  $\tau^- \rightarrow a_1 \rightarrow \pi^- \pi^0 \pi^0 \nu_\tau$  background variation. The number in parentheses are only statistical errors.

	Default	$+2\epsilon_{\pi^0}(1 - \epsilon_{\pi^0})$	$-2\epsilon_{\pi^0}(1 - \epsilon_{\pi^0})$
$M_\rho$ (GeV)	$0.7744 \pm 0.0002$	$0.7745(0.0001)$	$0.7743(-0.0001)$
$\Gamma_\rho$ (GeV)	$0.1499 \pm 0.0003$	$0.1498(-0.0001)$	$0.1500(0.0001)$
$M_{\rho'}$ (GeV)	$1.2983 \pm 0.0024$	$1.2989(0.0006)$	$1.2977(-0.0006)$
$\Gamma_{\rho'}$ (GeV)	$0.5012 \pm 0.012$	$0.5009(-0.0003)$	$0.5015(0.0003)$
$M_{\rho''}$ (GeV)	$1.6524 \pm 0.0068$	$1.6530(0.0006)$	$1.6518(-0.0006)$
$\Gamma_{\rho''}$ (GeV)	$0.2453 \pm 0.0362$	$0.2451(-0.0002)$	$0.2455(0.0002)$
$\beta$	$0.088 \pm 0.012$	$0.088(0.000)$	$0.088(0.000)$
$\gamma$	$0.058 \pm 0.008$	$0.058(0.000)$	$0.058(0.000)$
$ \phi_\beta $ (degree)	$118.3 \pm 8.2$	$118.2(-0.1)$	$118.4(0.1)$
$ \phi_\gamma $ (degree)	$58.9 \pm 8.2$	$58.9(0.0)$	$58.9(0.0)$
$a_\mu^{\pi\pi}(10^{-10})$	458.80	458.66	458.94
$\Delta a_\mu^{\pi\pi}(10^{-10})$		-0.14	0.14

Tab. X.11: We vary the contribution of  $\tau^- \rightarrow a_1 \rightarrow \pi^-\pi^0\pi^0\nu_\tau$  due to possibility that 1 missing  $\pi^0$  of a1 can be mis-identified as signal. The number in parentheses are only statistical errors.

	Default	$+\sigma_{\tau^- \rightarrow K^- K^0 \pi^0 \nu_\tau}$	$-\sigma_{\tau^- \rightarrow K^- K^0 \pi^0 \nu_\tau}$
$M_\rho$ (GeV)	$0.7744 \pm 0.0002$	$0.7744(0.0000)$	$0.7744(0.0000)$
$\Gamma_\rho$ (GeV)	$0.1499 \pm 0.0003$	$0.1499(0.0000)$	$0.1499(0.0000)$
$M_{\rho'}$ (GeV)	$1.2983 \pm 0.0024$	$1.2983(0.0000)$	$1.2983(0.0000)$
$\Gamma_{\rho'}$ (GeV)	$0.5012 \pm 0.012$	$0.5012(0.0000)$	$0.5012(0.0000)$
$M_{\rho''}$ (GeV)	$1.6524 \pm 0.0068$	$1.6524(0.0000)$	$1.6524(0.0000)$
$\Gamma_{\rho''}$ (GeV)	$0.2453 \pm 0.0362$	$0.2543(0.0000)$	$0.2543(0.0000)$
$\beta$	$0.088 \pm 0.012$	$0.088(0.000)$	$0.088(0.000)$
$\gamma$	$0.058 \pm 0.008$	$0.058(0.000)$	$0.058(0.000)$
$ \phi_\beta $ (degree)	$118.3 \pm 8.2$	$118.3(0.0)$	$118.3(0.0)$
$ \phi_\gamma $ (degree)	$58.9 \pm 8.2$	$58.9(0.0)$	$58.9(0.0)$
$a_\mu^{\pi\pi}(10^{-10})$	458.80	458.78	458.82
$\Delta a_\mu^{\pi\pi}(10^{-10})$		-0.02	0.02

Tab. X.12: Parameters after  $\tau^- \rightarrow K^- K^0 \pi^0 \nu_\tau$  background variation. The number in parentheses are only statistical errors.

	Default	$+\sigma_{\tau^- \rightarrow \pi^- K^0 \nu_\tau}$	$-\sigma_{\tau^- \rightarrow \pi^- K^0 \nu_\tau}$
M $\rho$ (GeV)	$0.7744 \pm 0.0002$	$0.7744(0.0000)$	$0.7744(0.0000)$
$\Gamma \rho$ (GeV)	$0.1499 \pm 0.0003$	$0.1499(0.0000)$	$0.1499(0.0000)$
M $\rho'$ (GeV)	$1.2983 \pm 0.0024$	$1.2983(0.0000)$	$1.2983(0.0000)$
$\Gamma \rho'$ (GeV)	$0.5012 \pm 0.012$	$0.5012(0.0000)$	$0.5012(0.0000)$
M $\rho''$ (GeV)	$1.6524 \pm 0.0068$	$1.6524(0.0000)$	$1.6524(0.0000)$
$\Gamma \rho''$ (GeV)	$0.2453 \pm 0.0362$	$0.2543(0.0000)$	$0.2543(0.0000)$
$\beta$	$0.088 \pm 0.012$	$0.088(0.000)$	$0.088(0.000)$
$\gamma$	$0.058 \pm 0.008$	$0.058(0.000)$	$0.058(0.000)$
$ \phi_\beta $ (degree)	$118.3 \pm 8.2$	$118.3(0.0)$	$118.3(0.0)$
$ \phi_\gamma $ (degree)	$58.9 \pm 8.2$	$58.9(0.0)$	$58.9(0.0)$
$a_\mu^{\pi\pi}(10^{-10})$	458.80	458.84	458.76
$\Delta a_\mu^{\pi\pi}(10^{-10})$		0.04	-0.04

Tab. X.13: Parameters after  $\tau^- \rightarrow \pi^- K^0 \pi^0 \nu_\tau$  background variation. The number in parentheses are only statistical errors.

	Default	$+\sigma_{\tau^- \rightarrow K^{*-} \rightarrow K^- \pi^0 \nu_\tau}$	$-\sigma_{\tau^- \rightarrow K^{*-} \rightarrow K^- \pi^0 \nu_\tau}$
M $\rho$ (GeV)	$0.7744 \pm 0.0002$	$0.7745(0.0001)$	$0.7743(-0.0001)$
$\Gamma \rho$ (GeV)	$0.1499 \pm 0.0003$	$0.1498(-0.0001)$	$0.1500(0.0001)$
M $\rho'$ (GeV)	$1.2983 \pm 0.0024$	$1.2990(0.0007)$	$1.2976(-0.0007)$
$\Gamma \rho'$ (GeV)	$0.5012 \pm 0.012$	$0.5008(-0.0004)$	$0.5016(0.0004)$
M $\rho''$ (GeV)	$1.6524 \pm 0.0068$	$1.6535(0.0011)$	$1.6514(-0.0010)$
$\Gamma \rho''$ (GeV)	$0.2453 \pm 0.0362$	$0.2540(-0.0003)$	$0.2546(0.0003)$
$\beta$	$0.088 \pm 0.012$	$0.087(-0.001)$	$0.089(0.001)$
$\gamma$	$0.058 \pm 0.008$	$0.057(-0.001)$	$0.059(0.001)$
$ \phi_\beta $ (degree)	$118.3 \pm 8.2$	$118.4(0.1)$	$118.2(-0.1)$
$ \phi_\gamma $ (degree)	$58.9 \pm 8.2$	$60.0(0.1)$	$58.8(-0.1)$
$a_\mu^{\pi\pi}(10^{-10})$	458.80	458.64	458.96
$\Delta a_\mu^{\pi\pi}(10^{-10})$		-0.16	0.16

Tab. X.14: Parameters after  $\tau^- \rightarrow K^{*-} \rightarrow K^- \pi^0 \nu_\tau$  background variation. The number in parentheses are only statistical errors.

	Default	$2e_{track}(1 - e_{track})$ correction
M $\rho$ (GeV)	$0.7744 \pm 0.0002$	$0.7744(0.0000)$
$\Gamma\rho$ (GeV)	$0.1499 \pm 0.0003$	$0.1499(0.0000)$
M $\rho'$ (GeV)	$1.2983 \pm 0.0024$	$1.2983(0.0000)$
$\Gamma\rho'$ (GeV)	$0.5012 \pm 0.012$	$0.5012(0.0000)$
M $\rho''$ (GeV)	$1.6524 \pm 0.0068$	$1.6524(0.0000)$
$\Gamma\rho''$ (GeV)	$0.2453 \pm 0.0362$	$0.2553(0.0000)$
$\beta$	$0.088 \pm 0.012$	$0.088(0.000)$
$\gamma$	$0.058 \pm 0.008$	$0.058(0.000)$
$ \phi_\beta $ (degree)	$118.3 \pm 8.2$	$118.3(0.0)$
$ \phi_\gamma $ (degree)	$58.9 \pm 8.2$	$58.9(0.0)$
$a_\mu^{\pi\pi}(10^{-10})$	458.80	458.80
$\Delta a_\mu^{\pi\pi}(10^{-10})$		0.00

Tab. X.15: We also vary the track efficiency correction to  $\tau^- \rightarrow K^{*-} \rightarrow K^-\pi^0\nu_\tau$  background. The number in parentheses are only statistical errors.

If  $\partial e = 3\%$  and  $e = 0.60$  and using the equation below:

$$\left( \frac{df(b, e)}{f(b, e)} \right) \approx \frac{2(0.6) - 1}{0.6(1 - 0.6)} 3\% \approx 2.5\%. \quad (\text{X.8})$$

We can vary the contribution of a1 by 2.5% up and down and takes the biggest difference from the default values as our systematic uncertainty. The result of this study is in Table 26.

We also check the shape of reconstructed  $\tau^- \rightarrow \pi^-\pi^0\pi^0\nu_\tau$  to check whether MonteCarlo can simulate Data. Using the same selection procedures we can plot both Data and MC. From the plot in X.12, we see that there is no significance difference between Data and MC in simulating  $\tau^- \rightarrow \pi^-\pi^0\pi^0\nu_\tau$ .

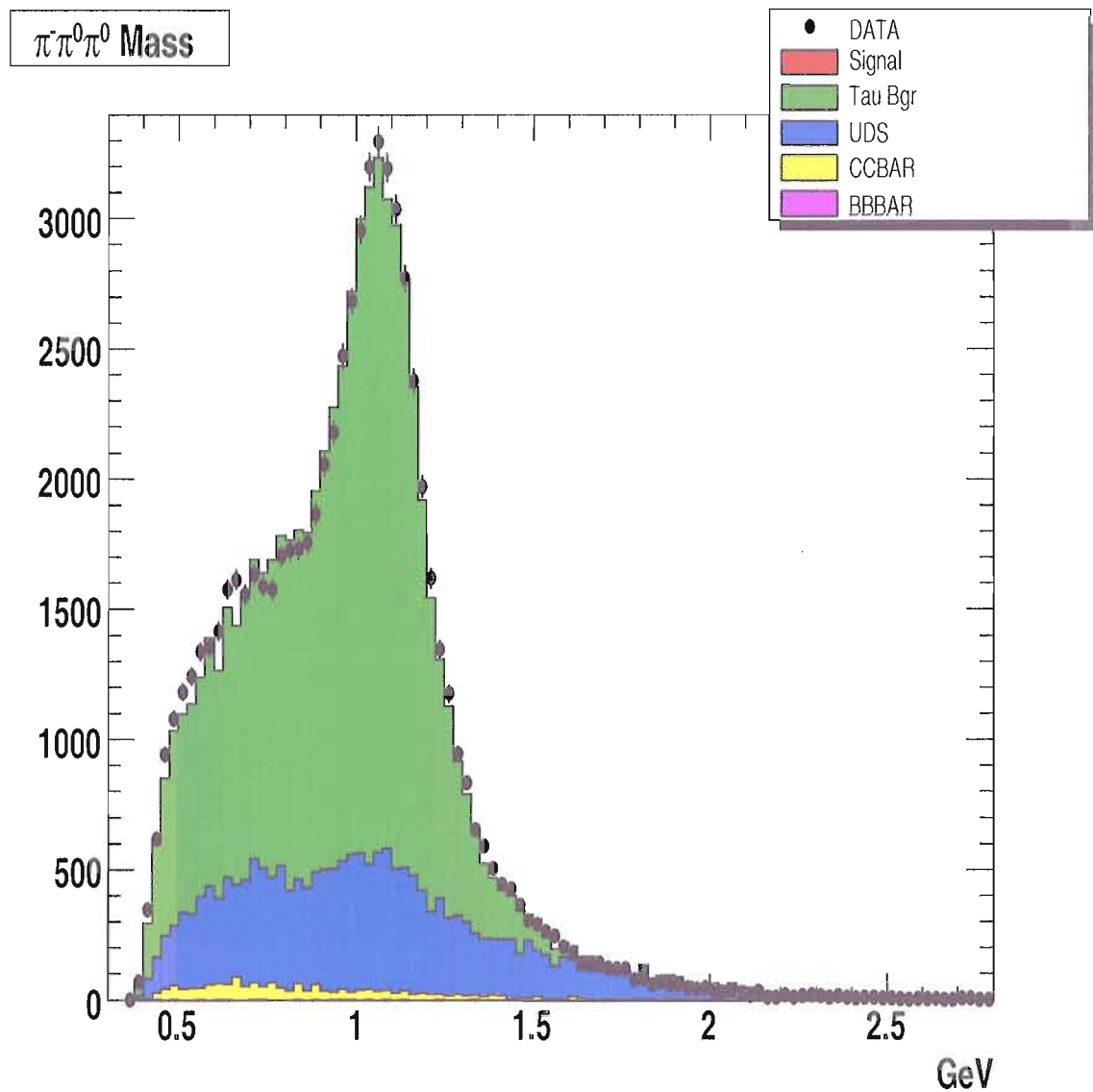


Fig. X.12: The invariant  $\pi^-\pi^0\pi^0$  mass, all MCs all normalized to Data Luminosity. We see that there is no significant difference between Data and MC in simulating  $\tau^- \rightarrow \pi^-\pi^0\pi^0\nu_\tau$

## 5 Other Systematic

### 5.1 Bin Size of $\pi^-\pi^0$ Invariant Mass

The Bin Size of  $\pi^-\pi^0$  invariant mass may change the extracted values. This analysis studies the uncertainty that comes from bin Size of  $\pi^-\pi^0$  invariant mass, by varying its size to 5, 10, 50 MeV. This analysis takes the biggest difference from default(25 MeV) values as the systematic uncertainty of bin size. This analysis assign  $0.3 \cdot 10^{-10}$  as the bin size systematic uncertainty of  $a_\mu^{\pi\pi}$ . The result of this study is in Table X.16.

### 5.2 Unfolding

The unfolding procedure may change the shape  $\pi^-\pi^0$  invariant mass spectrum, so that we need to understand the effect of unfolding. Unfolding procedure is discussed in Chapter VIII page 70. One way to assign unfolding systematic uncertainties conservatively is by comparing the extracted values with and without unfolding. This analysis extracts the results directly without unfolding and takes the difference between unfolding and without unfolding values as the unfolding systematic uncertainty. Without unfolding we can perform unbinned analysis and compare its results to default values. The result of this study is in Table X.17.

	Default	5 MeV Bin	10 MeV Bin	50 MeV Bin
$M \rho(\text{GeV})$	$0.7744 \pm 0.0002$	$0.7746(0.0002)$	$0.7744(0.0000)$	$0.7743(-0.0001)$
$\Gamma\rho(\text{GeV})$	$0.1499 \pm 0.0003$	$0.1496(-0.0003)$	$0.1497(-0.0002)$	$0.1502(0.0003)$
$M \rho'(\text{GeV})$	$1.2983 \pm 0.0024$	$1.2988(0.0005)$	$1.2985(0.0002)$	$1.2980(-0.0003)$
$\Gamma\rho'(\text{GeV})$	$0.5012 \pm 0.012$	$0.5003(-0.0009)$	$0.5008(-0.0004)$	$0.5017(0.0005)$
$M \rho''(\text{GeV})$	$1.6524 \pm 0.0068$	$1.6535(0.0011)$	$1.6529(0.0005)$	$1.6531(0.0007)$
$\Gamma\rho''(\text{GeV})$	$0.2453 \pm 0.0362$	$0.2523(-0.0020)$	$0.2528(-0.0015)$	$0.2564(0.0021)$
$\beta$	$0.088 \pm 0.012$	$0.090(0.002)$	$0.089(0.001)$	$0.086(-0.002)$
$\gamma$	$0.058 \pm 0.008$	$0.061(0.003)$	$0.060(0.002)$	$0.055(-0.003)$
$ \phi_\beta (\text{degree})$	$118.3 \pm 8.2$	$118.6(0.3)$	$118.5(0.2)$	$118.0(-0.3)$
$ \phi_\gamma (\text{degree})$	$58.9 \pm 8.2$	$59.1(0.2)$	$59.0(0.1)$	$58.7(-0.2)$
$a_\mu^{\pi\pi}(10^{-10})$	458.80	458.51	458.66	459.04
$\Delta a_\mu^{\pi\pi}(10^{-10})$		-0.29	-0.14	0.24

Tab. X.16: GS Fitting Parameters with 5, 10 and 50 MeV Bins. The number in parentheses are only statistical errors.

	Default	Without Unfolding	Unbinned and Without Unfolding
$M\rho(\text{GeV})$	$0.7744 \pm 0.0002$	$0.7740(-0.0004)$	$0.7747(0.0003)$
$\Gamma\rho(\text{GeV})$	$0.1499 \pm 0.0003$	$0.1501(0.0002)$	$0.1496(-0.0003)$
$M\rho'(\text{GeV})$	$1.2983 \pm 0.0024$	$1.2995(0.0012)$	$1.2991(0.0008)$
$\Gamma\rho'(\text{GeV})$	$0.5012 \pm 0.012$	$0.5008(-0.0004)$	$0.5004(-0.0010)$
$M\rho''(\text{GeV})$	$1.6524 \pm 0.0068$	$1.6497(-0.0027)$	$1.6540(0.0016)$
$\Gamma\rho''(\text{GeV})$	$0.2453 \pm 0.0362$	$0.2602(0.0149)$	$0.2519(-0.0034)$
$\beta$	$0.088 \pm 0.012$	$0.086(-0.002)$	$0.090(0.002)$
$\gamma$	$0.058 \pm 0.008$	$0.056(-0.002)$	$0.062(0.004)$
$ \phi_\beta (\text{degree})$	$118.3 \pm 8.2$	$118.6(0.3)$	$118.8(0.5)$
$ \phi_\gamma (\text{degree})$	$58.9 \pm 8.2$	$58.7(-0.2)$	$59.1(0.2)$
$a_\mu^{\pi\pi}(10^{-10})$	458.80	459.04	458.44
$\Delta a_\mu^{\pi\pi}(10^{-10})$		0.24	-0.36

Tab. X.17: Fitting parameters with and without unfolding. We also compare it with unbinned fitting. The number in parentheses are statistical errors.

### 5.3 Stability Over Runs Period

The stability over Runs period is very important. The Data and MonteCarlo consist of data from 5 RUNs period. All Data and MonteCarlo are classified into their Run periods, then we recalculate the Branching fraction of the  $\tau^- \rightarrow \pi^-\pi^0\nu_\tau$  for each different RUN using the information of efficiency, number of selected events and number of generated events. Run 1 has very low number of events and it contributes the biggest deviation from default values. After careful calculation, this analysis find that the variations between all RUNs are within their statistical uncertainties. The result of this study is in Table X.18.

In addition to stability of branching for different Runs, we also refit the invariant  $\pi^-\pi^0$  for 5 different Runs. using Gounaris-Sakurai function and the same procedure. At the end of fitting, the analyst extract the value of  $a_\mu^{\pi\pi}$ . Taking the biggest differences between default(all Runs) values and single Run values. Run 1 has the smallest number of events, so that the parameter values from Run 1 are slightly different from the default of all-Runs values.

The result of this study is in Table X.19.

RUN	$\text{Br}(\tau^- \rightarrow \pi^-\pi^0\nu_\tau)$	Begin	End
1	25.33%	Feb 2000	Oct 2000
2	25.42%	Feb 2001	Jun 2002
3	25.35%	Dec 2002	Jun 2003
4	25.42%	Sep 2003	Jul 2004
5	25.39%	May 2005	Apr 2006
TOTAL	25.40%	Feb 2000	Apr 2006

Tab. X.18: The Branching Fraction  $\tau^- \rightarrow \pi^-\pi^0\nu_\tau$  for 5 different Runs.

	ALL RUNS	Run 1	Run 2	Run 3	Run 4	Run 5
$M \rho(\text{GeV})$	$0.7744 \pm 0.0002$	$0.7743(-0.0001)$	$0.7743(-0.0001)$	$0.7745(0.0001)$	$0.7744(0.0000)$	$0.7745(0.0001)$
$\Gamma \rho(\text{GeV})$	$0.1499 \pm 0.0003$	$0.1497(-0.0002)$	$0.1500(0.0001)$	$0.1501(0.0002)$	$0.1498(-0.0001)$	$0.1499(0.0000)$
$M \rho'(\text{GeV})$	$1.2983 \pm 0.0024$	$1.2980(-0.0003)$	$1.2981(-0.0002)$	$1.2982(-0.0001)$	$1.2984(0.0001)$	$1.2984(0.0001)$
$\Gamma \rho'(\text{GeV})$	$0.5012 \pm 0.012$	$0.5008(-0.0004)$	$0.5009(-0.0003)$	$0.5013(0.0001)$	$0.5013(0.0001)$	$0.5012(0.0000)$
$M \rho''(\text{GeV})$	$1.6524 \pm 0.0068$	$1.6532(0.0008)$	$1.6529(0.0005)$	$1.6531(0.0007)$	$1.6522(-0.0002)$	$1.6521(-0.0003)$
$\Gamma \rho''(\text{GeV})$	$0.2453 \pm 0.0362$	$0.2562(0.0009)$	$0.2548(-0.0005)$	$0.2564(0.0011)$	$0.2452(-0.0001)$	$0.2454(0.0001)$
$\beta$	$0.088 \pm 0.012$	$0.084(-0.004)$	$0.085(-0.003)$	$0.086(-0.002)$	$0.089(0.001)$	$0.089(0.001)$
$\gamma$	$0.058 \pm 0.008$	$0.056(-0.002)$	$0.057(-0.001)$	$0.055(-0.003)$	$0.060(0.002)$	$0.058(0.000)$
$ \phi_\beta (\text{degree})$	$118.3 \pm 8.2$	$118.0(-0.3)$	$118.2(-0.1)$	$118.0(-0.3)$	$118.4(0.001)$	$118.4(0.001)$
$ \phi_\gamma (\text{degree})$	$58.9 \pm 8.2$	$59.3(0.4)$	$59.1(0.2)$	$58.7(-0.2)$	$58.8(-0.1)$	$58.9(0.0)$
$a_\mu^{\pi\pi}$	$458.80 \times 10^{-10}$	$458.69 \times 10^{-10}$	$458.88 \times 10^{-10}$	$458.89 \times 10^{-10}$	$458.75 \times 10^{-10}$	$458.84 \times 10^{-10}$
$\Delta a_\mu^{\pi\pi}$		$-0.11 \times 10^{-10}$	$0.08 \times 10^{-10}$	$0.09 \times 10^{-10}$	$-0.05 \times 10^{-10}$	$0.04 \times 10^{-10}$

Tab. X.19: Fitting parameters for 5 different runs. The number in parentheses are only statistical errors.

## 6 Comparison between GS and KS Fitting

Besides the default of fitting function, Gounaris-Sakurai, there is another fitting function, Kuhn-SantaMaria that has been used by many analysts to study spectral function of  $\tau^- \rightarrow \pi^-\pi^0\nu_\tau$ . We refit the spectrum using the same procedure, instead of using the default(GS), we fit using the Kuhn-SantaMaria fitting function. We take the difference between the results of two fitting as our systematic uncertainties. The results can be seen in Table X.20.

	Gounaris-Sakurai	Kuhn-SantaMaria
M $\rho$ (GeV)	$0.7744 \pm 0.0002$	$0.7740 \pm 0.0002$
$\Gamma\rho$ (GeV)	$0.1499 \pm 0.0003$	$0.1494 \pm 0.0003$
M $\rho'$ (GeV)	$1.2983 \pm 0.0024$	$1.2998 \pm 0.0026$
$\Gamma\rho'$ (GeV)	$0.5012 \pm 0.0120$	$0.5105 \pm 0.0132$
M $\rho''$ (GeV)	$1.6524 \pm 0.0068$	$1.6606 \pm 0.0070$
$\Gamma\rho''$ (GeV)	$0.2453 \pm 0.0362$	$0.2480 \pm 0.0356$
$\beta$	$0.088 \pm 0.012$	$0.090 \pm 0.015$
$\gamma$	$0.058 \pm 0.008$	$0.059 \pm 0.009$
$ \phi_\beta $ (degree)	$118.3 \pm 8.2$	$125.5 \pm 11.5$
$ \phi_\gamma $ (degree)	$58.9 \pm 8.2$	$63.4 \pm 7.5$
$a_\mu^{\pi\pi}(10^{-10})$	458.80	458.56
$\Delta a_\mu^{\pi\pi}(10^{-10})$		-0.24

Tab. X.20: The errors are only statistical and we find that the fitting parameters for both KS and GS models are consistent within the statistical errors.

## 7 Statistical Uncertainty

This analysis asseses the overall statistical uncertainty by generating a large number of G&S parameter sets, with the parameter determined randomly about the central values returned by our nominal fit, assuming Gaussian uncertainties. This analysis determines  $a_\mu^{\pi\pi}$  separately for each parameter set. The r.m.s. of the distribution of values was found to be  $0.4 \times 10^{-10}$ .

	$\Delta a_{\mu}^{\pi\pi}$ $10^{-10}$	$\Delta M_{\rho}$ (GeV)	$\Delta \Gamma_{\rho}$ (GeV)	$\Delta M_{\rho'}$ (GeV)	$\Delta \Gamma_{\rho'}$ (GeV)	$\Delta M_{\rho''}$ (GeV)	$\Delta \Gamma_{\rho''}$ (GeV)	$\Delta \beta$	$\Delta \gamma$	$\Delta  \phi_{\beta} $ (deg)	$\Delta  \phi_{\gamma} $ (deg)
$\tau^- \rightarrow e^- \nu_e \nu_{\tau}$	0.00	0.00001	0.0	0.0	0.0	0.0	0.0	0.0	0.0	0.0	0.0
$\tau^- \rightarrow \pi^- \nu_{\tau}$	0.01	0.00002	0.0	0.0	0.0	0.0	0.0	0.0	0.0	0.0	0.0
$\tau^- \rightarrow a_1 \rightarrow \pi^- \pi^0 \pi^0 \nu_{\tau}$	0.07	0.00004	0.0000	0.0001	0.0001	0.0002	0.0001	0.000	0.000	0.0	0.0
$\tau^- \rightarrow a_1 \rightarrow \pi^- \pi^0 \pi^0 \nu_{\tau} (mis - id)$	0.14	0.00009	0.001	0.0006	0.0003	0.0006	0.0002	0.000	0.000	0.1	0.0
$\tau^- \rightarrow K^- K^0 \pi^0 \nu_{\tau}$	0.02	0.00003	0.0	0.0	0.0	0.0	0.0	0.0	0.0	0.0	0.0
$\tau^- \rightarrow \pi^- K^0 \pi^0 \nu_{\tau}$	0.04	0.00004	0.0	0.0	0.0	0.0	0.0	0.0	0.0	0.0	0.0
$\tau^- \rightarrow K^{*-} \rightarrow K^- \pi^0 \nu_{\tau}$	0.16	0.00012	0.0001	0.0007	0.0004	0.0010	0.0003	0.001	0.001	0.1	0.1
uds bgr	0.23	0.00014	0.0001	0.0003	0.0002	0.0004	0.0005	0.001	0.001	0.2	0.1
trk eff	0.18	0.00012	0.0001	0.0002	0.0003	0.0003	0.0002	0.000	0.001	0.1	0.1
$\theta_{track}$ smearing	0.07	0.00004	0.0001	0.0001	0.0001	0.0002	0.0002	0.001	0.001	0.2	0.1
$P_{track}$ smearing	0.18	0.00019	0.0002	0.0003	0.0002	0.0004	0.0005	0.001	0.001	0.2	0.1
$E_{\gamma}$ smearing	0.46	0.00036	0.0008	0.0016	0.0050	0.0102	0.0039	0.002	0.002	0.7	0.6
$\theta_{\gamma}$ smearing	0.15	0.00016	0.0004	0.0008	0.0006	0.0060	0.0019	0.001	0.001	0.5	0.6
$\phi_{\gamma}$ smearing	0.08	0.00006	0.0001	0.0002	0.0003	0.0005	0.0005	0.001	0.001	0.3	0.5
$\pi^0$ efficiency	0.35	0.00003	0.0001	0.0002	0.0009	0.0009	0.0002	0.000	0.000	0.1	0.0
Model dependencies	0.24	0.00040	0.0005	0.0015	0.0093	0.0082	0.0027	0.002	0.001	7.2	4.5
Bin Size	0.29	0.00022	0.0003	0.0005	0.0009	0.0011	0.0020	0.002	0.003	0.3	0.2
Different Run	0.11	0.00008	0.0002	0.0003	0.0004	0.0008	0.0011	0.004	0.002	0.3	0.4
Total Systematic	0.83	0.00069	0.0013	0.0029	0.0110	0.0176	0.0061	0.005	0.005	7.3	4.7
Statistical	0.40	0.00020	0.0003	0.0024	0.0120	0.0068	0.0362	0.012	0.008	8.2	8.2
Total Uncertainties	0.92	0.00072	0.0013	0.0038	0.0163	0.0189	0.0367	0.013	0.009	11.0	9.5
PDG 2007		0.7755	0.1494	1.4650	0.4000	1.7200	0.2500				
$\Delta$ PDG 2007		0.0003	0.0010	0.0025	0.0060	0.0200	0.1000				

Tab. X.21: Summary of fitting parameters and their experimental uncertainties

	$\Delta a_{\mu}^{\pi\pi}$ $10^{-10}$	$\Delta M_{\rho}$ (GeV)	$\Delta \Gamma_{\rho}$ (GeV)	$\Delta M_{\rho'}$ (GeV)	$\Delta \Gamma_{\rho'}$ (GeV)	$\Delta M_{\rho''}$ (GeV)	$\Delta \Gamma_{\rho''}$ (GeV)	$\Delta \beta$	$\Delta \gamma$	$\Delta  \phi_{\beta} $ (deg)	$\Delta  \phi_{\gamma} $ (deg)
Background	0.32	0.00022	0.0002	0.0010	0.0005	0.0012	0.0006	0.001	0.001	0.2	0.1
Track Reconstruction	0.26	0.00023	0.0002	0.0004	0.0004	0.0005	0.0006	0.001	0.002	0.3	0.2
$\pi^0$ Reconstruction	0.60	0.00040	0.0009	0.0018	0.0051	0.0119	0.0044	0.002	0.002	0.9	1.0
Fitting Procedure	0.38	0.00046	0.0006	0.0016	0.0093	0.0083	0.0034	0.003	0.003	7.2	4.5
Statistical	0.40	0.00020	0.0003	0.0024	0.0120	0.0068	0.0362	0.012	0.008	8.2	8.2
Total Uncertainties	0.92	0.00072	0.0013	0.0038	0.0163	0.0189	0.0367	0.013	0.009	11.0	9.5

Tab. X.22: Final fitting parameters and their experimental uncertainties

## CHAPTER XI

### CONCLUSION

Using the BABAR Detector, we have studied the physics of hadronic  $\tau \rightarrow \pi^- \pi^0 \nu_\tau$  decays. Hadronic  $\tau$  decays provide one of the most powerful testing grounds for QCD and this situation results from a number of favorable conditions:

- $\tau$  leptons are copiously produced in pairs at  $e^+ e^-$  colliders, leading to simple event topologies with small number of backgrounds. The purity in this analysis about 95%, the percentage of backgrounds after all selection cuts is about 5%.
- The experimental study of  $\tau$  decays could be done with large data samples and this analysis used about 250 millions  $\tau$  pairs.

The  $\tau$  decay rates into hadrons are expressed through spectral functions of different final states. The spectral functions are the basic ingredients to the theoretical description of these decays, since they represent the probability to produce a given hadronic system from the vacuum, as a function of its invariant mass.

From the  $\tau^- \rightarrow \pi^- \pi^0 \nu_\tau$  decays in BABAR Detector, we can measure  $\rho$ ,  $\rho'$  and  $\rho''$  resonance parameters and extract the value of  $a_\mu^{\pi\pi}$ . The results of this analysis are comparable with other experiments and due to higher statistics the  $a_\mu^{\pi\pi}$  value has lower uncertainties compared to other experiments.

## 1 Theoretical Correction

SU(2) can be broken by some sources

- Electroweak radiative corrections to  $\tau$  decays are contained in the  $S_{EW}$  factor (see [79] and [80]), which is dominated by short-distance effects. It is expected to be weakly dependent on the specific hadronic final state, as verified for the  $\tau \rightarrow (\pi^-, K^-)\nu_\tau$  decays [81]. Detailed calculations have been performed for the  $\pi^-\pi^0$  channel (see [82]), which also confirm the relative smallness of the long-distance contributions. The total correction is  $S_{EW} = S_{EW}^{had}S_{EM}^{had}/S_{EM}^{lep}$ , where  $S_{EW}^{had}$  is the leading-log short-distance electroweak factor (which vanishes for leptons) and  $S_{EM}^{had,lep}$  are the nonleading electromagnetic corrections. The latter corrections have been calculated at the quark level [79], at the hadron level for the  $\pi^-\pi^0$  decay mode (see [82]), and for leptons [79],[80]. The total correction amounts to [83]  $S_{EW}^{incl} = 1.0198 \pm 0.0006$  for the inclusive hadron decay rate and  $S_{EW}^{\pi\pi^0} = (1.0232 \pm 0.0006)G_{EM}^{\pi\pi^0}(s)$  for the  $\pi\pi^0$  decay mode, where  $G_{EM}^{\pi\pi^0}(s)$  is an s-dependent long-distance radiative correction [82]. This factor has been included in the  $a_\mu^{\pi\pi}$  calculation given in Section 2 Chapter IX.
- *The pion mass splitting* breaks isospin symmetry in the spectral functions [44], [84] since  $\beta_-(s) \neq \beta_0(s)$ .
- Isospin symmetry is also broken in the pion form factor due to the  $\pi$  mass splitting [44],[82].
- A similar effect is expected from the  $\rho$  mass splitting. The theoretical expectation [49], gives a limit ( $< 0.7$  MeV), but this is only a rough estimate. Hence the question must be investigated experimentally, the best approach being the explicit comparison of  $\tau$  and  $e^+e^-$  in  $2\pi$  spectral functions, after correction for

the other isospin-breaking effects. No correction for  $\rho$  mass splitting is applied initially.

- Explicit electromagnetic decays introduce small differences between the widths of the charged and neutral  $\rho$ 's.
- Isospin violation in the strong amplitude through the mass difference between u and d quarks is expected to be negligible.
- When comparing  $\tau$  with  $e^+e^-$  data, an obvious and locally large correction must be applied to the  $\tau$  spectral function to introduce the effect of  $\rho - \omega$  mixing, only present in the neutral channel. This correction is computed using the parameters determined by the  $e^+e^-$  experiments in their form factor fits to the  $\pi^+\pi^-$  lineshape modeling  $\rho - \omega$  interference [8].

To incorporate the missing  $\rho - \omega$  interference in  $\tau$  data, we modify the GS function to include it, introducing the parameter  $\alpha$  (following the notation of Ref. [30],  $\alpha$  is 0 if there is no  $\omega$ ) to quantify the  $\omega$  admixture, analogous to the parameters  $\beta$  and  $\gamma$  which quantify the  $\rho'$  and  $\rho''$ . From the CLEO, we use  $\alpha = (1.71 \pm 0.06 \pm 0.20) \times 10^{-3}$ . Modifying our fit function in this way leads to an increase in  $a_\mu^{\pi\pi}$  by  $3.4 \times 10^{-10}$ .

The total correction from known SU(2)-violating effects which include all corrections above is predicted to be  $(-1.8 \pm 2.3) \times 10^{-10}$ , where the central values taken from [5] and we enlarge the error by interpolating the values in Table 5 of reference [83].

## 2 Summary

The result for  $a_\mu^{\pi\pi}$  integrated over the mass range  $\sqrt{s} = 0.50\text{-}1.8 \text{ GeV}/c^2$  after correction(see previous section) is:

$$\hat{a}_\mu^{\pi\pi}(0.50, 1.80) = 456.65 \pm 0.40(\text{stat}) \pm 0.83(\text{int sys}) \pm 2.61(\text{ext sys}) \pm 2.3_{SU(2)}. \quad (\text{XI.1})$$

- *stat.* is the statistical uncertainty that has been calculated previously in the special section of Statistical Uncertainty[see section 7]. It has lower value, due to the fact that we use bigger number of data compared to all previous experiments. It should be noted that the total uncertainty in this analysis is dominated by internal systematic error, so that adding more data samples will have no significant improvement to the precision of this analysis.
- *int.sys.* is the total internal systematic uncertainty that comes from this analysis and explained in Chapter X. The internal systematic uncertainty is dominated by neutral resolution and efficiency uncertainties.
- *ext.sys.* is the total external systematic uncertainty is are calculated from other experiments The sources of external systematic uncertainties are:

Tab. XI.1: External Parameters and their uncertainties

	Value	Error(%)	$\Delta a_\mu^{\pi\pi}(10^{-10})$	Source
$S_{EW}^{\pi\pi}/S_{EW}^e$	$1.0233 \pm 0.0006$	0.06	$\pm 0.32$	[83] [82]
$V_{ud}$	$0.97418 \pm 0.00027$	0.027	$\pm 0.15$	[2]
$B_e$	$(17.84 \pm 0.05)\%$	0.28	$\pm 1.52$	[2]
$B_{\pi\pi^0}$	$(25.50 \pm 0.10)\%$	0.39	$\pm 2.09$	
Total			$\pm 2.61$	

To calculate  $a_\mu^{\pi\pi}$ , we use the branching fraction of  $\tau^- \rightarrow \pi^-\pi^0\nu_\tau$  decays from PDG 2007 [2], which has very low uncertainty. This analysis only calculate the branching fraction for consistency check, due to its big systematic uncertainty(see Table X.18).

### 3 Comparison with Other Experiments

The results of this analysis are compared to the results from other major experiments.

#### 3.1 $M_\rho$

The measured  $M_\rho$  is  $0.7745 \pm 0.00072$  GeV, the total uncertainty includes systematic and statistical uncertainties. The central value closer to the result from  $e^+e^-$  experiment(CMD-2) than other  $\tau$  experiments(ALEPH and CLEO), except the the result from Belle(see Table XI.2).

#### 3.2 $\Gamma_\rho$

The measured  $\Gamma_\rho$  is  $0.1493 \pm 0.0013$  GeV, the result is consisent (within uncertainties) with other  $\tau$  experiments(Belle, ALEPH and CLEO) and not consistent with  $e^+e^-$ (CMD-2) experiment(see Table XI.2). One possible explanation is there is no  $\omega$  interference in  $\tau$  decay, especially in  $\rho$  mass peak.

#### 3.3 $M_{\rho'}$

For  $M_{\rho'}$ , the central value that we measured is  $1.2993 \pm 0.0038$  GeV much lower than other experiments, but it has lower uncertainty compared to other experiments

in the table(see Table XI.2). The discrepancy in central value maybe related to the correlation with other resonances( $\rho$  and  $\rho''$ ).

### 3.4 $\Gamma_{\rho'}$

For  $\Gamma_{\rho'}$ , the central value that we measured is  $0.4990 \pm 0.0163$  GeV consistent with Belle and CMD-2; and within  $2\sigma$  with CLEO and ALEPH(see Table XI.2). The central value has lower uncertainty compared to other experiments in the table.

### 3.5 $M_{\rho''}$

Measurement of  $M_{\rho''}$  is one of most significant results in this analysis, because our knowledge about  $M_{\rho''}$  was very limited, even in PDG 2007[2], the quoted value was only an educated guess(quoted  $1.720 \pm 0.020$  GeV, but it is written “OUR ESTIMATE”, based on observed range of data. Not from a formal statistical procedure). In fact, this analysis confirmed the existence  $\rho''$ . This analysis has seen that  $\rho''$  is peaking at  $1.6614 \pm 0.0189$  GeV and its value and precision comparable to the values from CMD-2 and Belle experiments(see Table XI.2).

Previous experiments, such as CLEO and ALEPH, couldn't measure  $M_{\rho''}$  due to limited number of events at high invariant mass, so that their values are limited statistically. Our analysis has much higher number of events so that we can measure it.

### 3.6 $\Gamma_{\rho''}$

Measurement of the width of  $\rho''$ (simplified as  $\Gamma_{\rho''}$  resonance is also one of most significant results in this analysis, because our knowledge about  $\Gamma_{\rho''}$  was very limited,

even in PDG 2007 [2], the quoted value was still an educated guess(quoted  $0.250 \pm 0.100$  GeV, but it is written “OUR ESTIMATE”, based on observed range of data. Not from a formal statistical procedure). This analysis has measured that  $\Gamma_{\rho''}$  is  $0.2433 \pm 0.0366$  GeV and its value and precision comparable to the values from CMD-2 and Belle experiments(see Table XI.2).

Our analysis has much higher number of events than previous experiments, so that we can measure it .

### 3.7 $\beta$

$\beta$  is the coefficient of  $\rho'$  in Gounaris-Sakurai function and the precision measurement of this value is very important to study the characterics of  $\rho'$ (see Table XI.2). We found its value is  $0.090 \pm 0.013$ .

### 3.8 $\phi_\beta$

$\phi_\beta$  is the phase of  $\rho'$  in Gounaris-Sakurai function and the precision measurement of this value is very important to study the characterics of  $\rho'$ , we found that  $\phi_\beta = 118.9 \pm 11.0$  deg(see Table XI.2).

### 3.9 $\gamma$

$\gamma$  is the coeficient of  $\rho''$  in Gounaris-Sakurai function and the precision measurement of this value is very important to study the characterics of  $\rho''$ (see Table XI.2). We found its value is  $0.060 \pm 0.009$ , about  $6\sigma$  significance.

### 3.10 $\phi_\gamma$

$\phi_\gamma$  is the phase of  $\rho''$  in Gounaris-Sakurai function and the precision measurement of this value is very important to study the characteristics of  $\rho''$ . We found that  $\phi_\gamma = 59.4 \pm 9.5$  deg, consistent with Belle( $44.2 \pm 17$ ) but ours has smaller uncertainty(see Table XI.2).

### 3.11 $\hat{a}_\mu^{\pi\pi}$

From Table XI.3 we can see that the value of  $\hat{a}_\mu^{\pi\pi}$  from this analysis is lower than the other  $\tau$  experiment results, but higher than the result from CMD-2( $e^+e^-$  experiments). Interestingly, the result of this analysis is statistically consistent with both  $\tau$  and  $e^+e^-$  experiments, so that it may solve one of the debated topics in High Energy Physics about discrepancy result of  $\tau$  and  $e^+e^-$  experiments.

This analysis may improve the precision of Standard Model prediction of muon g-2, because our result has lower uncertainty than all previous  $\hat{a}_\mu^{\pi\pi}$  measurement. In the light of precision measurement muon g-2 result from BNL,  $\hat{a}_\mu^{\pi\pi}$  that is derived from  $\tau$  not consistent with the result of BNL g-2 (previously, it was claimed that the result of BNL is consistent with the result derived from  $\tau$  experiment, but not  $e^+e^-$  experiments).

### 3.12 Comments on $\rho''$

In addition, in this analysis we confirm the existence of  $\rho''$ . We have measured its coupling and phase with more than  $5\sigma$ .  $\rho''$  was observed non significantly by ALEPH, CLEO and OPAL.

	BaBar	Belle	ALEPH( $\tau$ )	CLEO	CMD-2( $e^+e^-$ )
$M \rho(\text{GeV})$	$0.7745 \pm 0.0007$	$0.7735 \pm 0.0002$	$0.7755 \pm 0.0007$	$0.7753 \pm 0.0005$	$0.7733 \pm 0.0006$
$\Gamma \rho(\text{GeV})$	$0.1493 \pm 0.0013$	$0.1492 \pm 0.0004$	$0.1490 \pm 0.0012$	$0.1505 \pm 0.0011$	$0.1452 \pm 0.0013$
$M \rho'(\text{GeV})$	$1.2993 \pm 0.0038$	$1.4530 \pm 0.0070$	$1.3280 \pm 0.0150$	$1.365 \pm 0.007$	$1.3370 \pm 0.0350$
$\Gamma \rho'(\text{GeV})$	$0.4990 \pm 0.0163$	$0.4376 \pm 0.0199$	$0.468 \pm 0.0410$	$0.356 \pm 0.026$	$0.5690 \pm 0.0810$
$M \rho''(\text{GeV})$	$1.6614 \pm 0.0189$	$1.7300 \pm 0.0220$	$1.7130(\text{fixed})$	$1.700(\text{fixed})$	$1.7130 \pm 0.0150$
$\Gamma \rho''(\text{GeV})$	$0.2433 \pm 0.0367$	$0.1379 \pm 0.0500$	$0.2350(\text{fixed})$	$0.2350(\text{fixed})$	$0.2350(\text{fixed})$
$\beta$	$0.090 \pm 0.013$	$0.167 \pm 0.005$	$0.210 \pm 0.008$	$0.121 \pm 0.009$	$0.123 \pm 0.011$
$\gamma$	$0.060 \pm 0.009$	$0.031 \pm 0.011$	$0.023 \pm 0.008$	$0.032 \pm 0.009$	$0.048 \pm 0.008$
$ \phi_\beta (\text{degree})$	$118.9 \pm 11.0$	$210.3 \pm 6.3$	$153.0 \pm 7.0$		$139.4 \pm 6.5$
$ \phi_\gamma (\text{degree})$	$59.4 \pm 9.5$	$44.2 \pm 17$	$0(\text{fixed})$		$0(\text{fixed})$

Tab. XI.2: The results of fitting to the  $M_{\pi\pi^0}$  distribution using Gounaris-Sakurai function from some experiments

	$\hat{a}_\mu^{\pi\pi}(10^{-10})$
BaBar	$456.65 \pm 0.40(\text{stat}) \pm 0.83(\text{int sys}) \pm 2.61(\text{ext sys}) \pm 2.30_{SU(2)}$
Belle	$459.80 \pm 0.50(\text{stat}) \pm 1.00(\text{int sys}) \pm 3.00(\text{ext sys}) \pm 2.30_{SU(2)}$
ALEPH( $\tau$ )	$464.0 \pm 3.2 \pm 2.3_{SU(2)}$
CMD-2( $e^+e^-$ )	$450.2 \pm 4.9 \pm 1.6_{SU(2)}$

Tab. XI.3: The results of  $\hat{a}_\mu^{\pi\pi}$  from some experiments

## APPENDIX A

### PHOTON RESOLUTION PLOTS

#### 1 Energy Resolution Plots

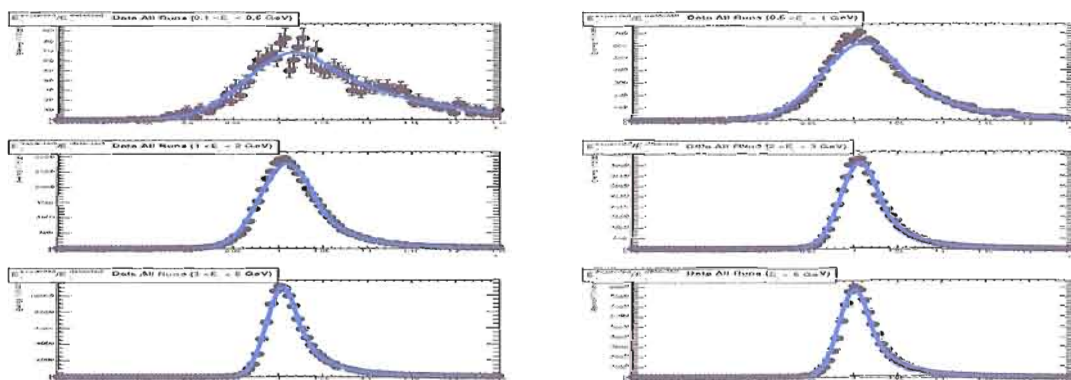


Fig. A.1: Energy Resolution Data All Runs.

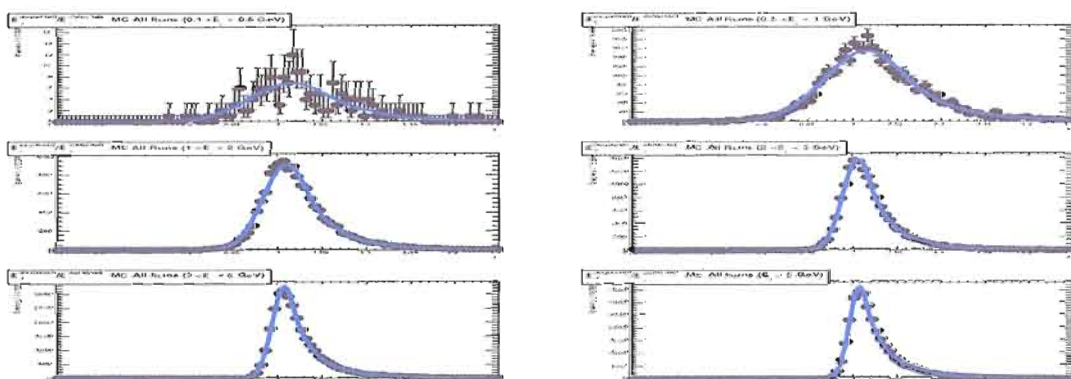


Fig. A.2: Energy Resolution MC All Runs.

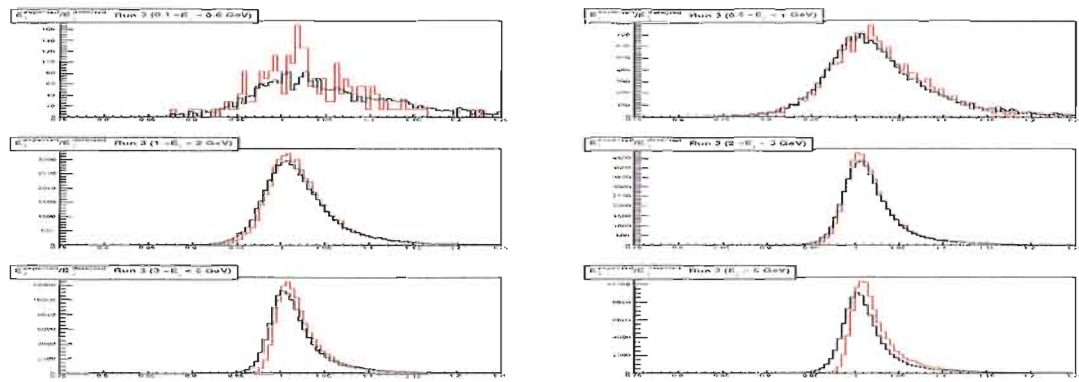


Fig. A.3: Energy Resolution Data(black line) and MC(red line) All Runs.

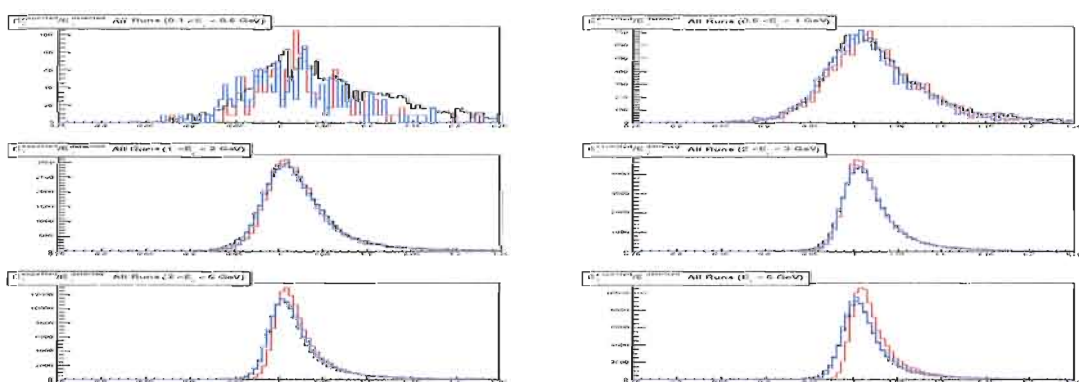


Fig. A.4: After Energy smearing: MC after smearing(blue line), initial MC(red line) and Data(black line) All Runs.

## 2 Neutral Theta( $\theta$ ) Resolution Plots

The ratio of expected and detected photon energy ( $\theta^{\text{expected}}/\theta^{\text{detected}}$ ) from  $e^+e^- \rightarrow \mu^+\mu^-\gamma$  samples

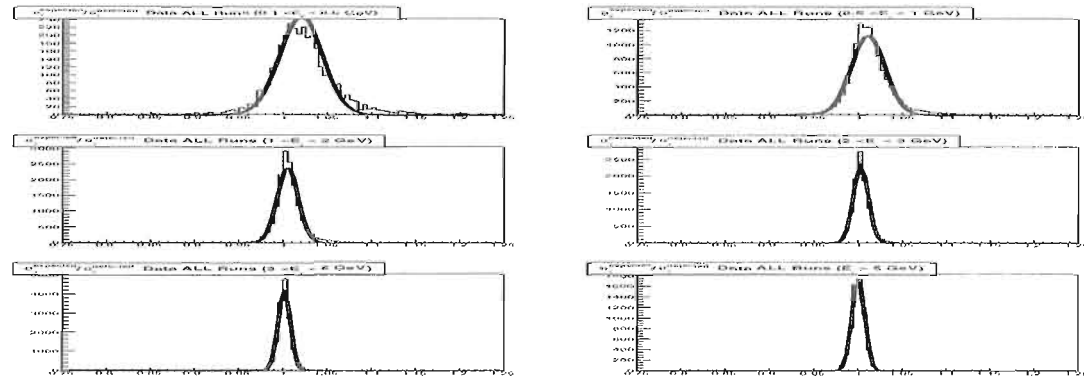


Fig. A.5: Theta Resolution Data All Runs.

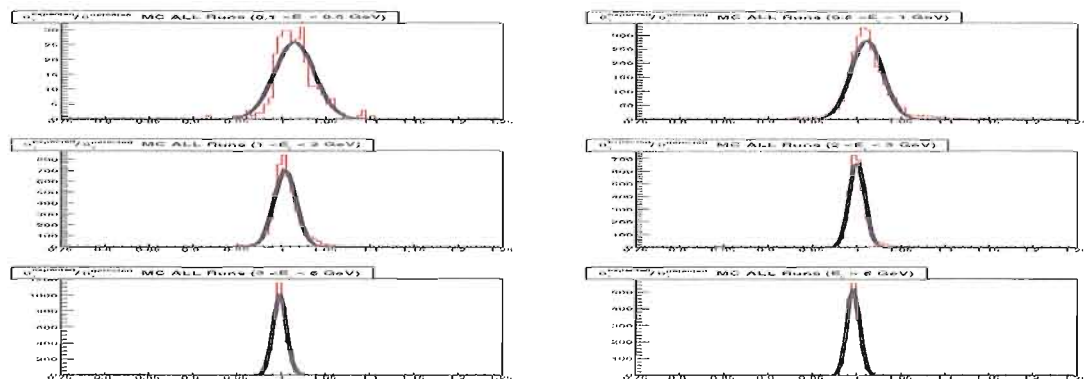


Fig. A.6: Theta Resolution MC All Runs.

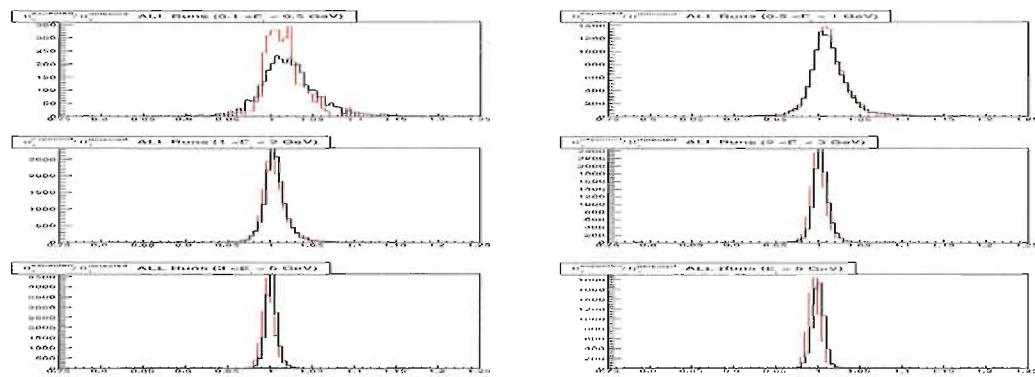


Fig. A.7:  $\Theta(\theta)$  Resolution Data(black line) and MC(red line) All Runs.

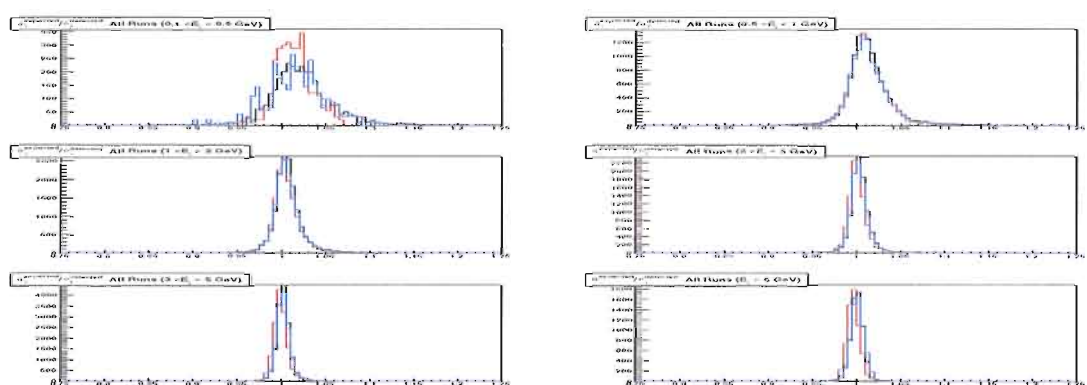


Fig. A.8: Neutral  $\Theta(\theta)$  smearing result. After  $\theta$  smearing: MC after smearing(blue line), initial MC(red line) and Data(black line) All Runs.

### 3 Neutral Phi( $\phi$ ) Resolution Plots

The ratio of expected and detected photon energy ( $\phi^{\text{expected}}/\phi^{\text{detected}}$ ) from  $e^+e^- \rightarrow \mu^+\mu^-\gamma$  samples

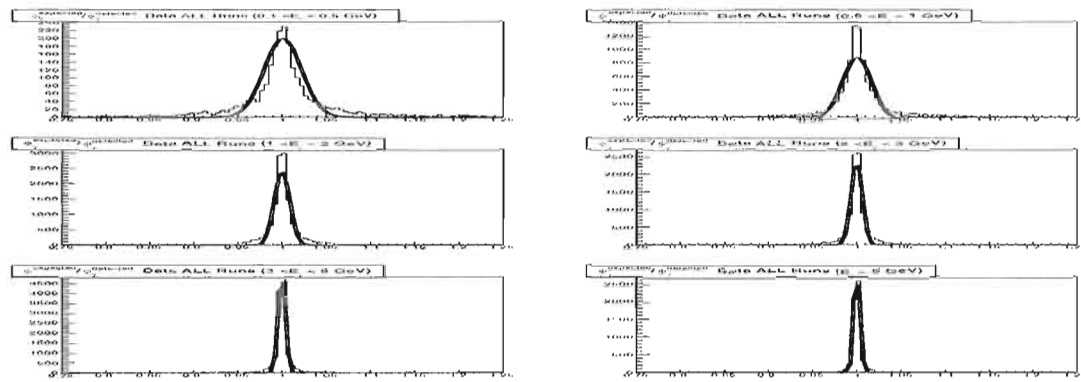


Fig. A.9: Phi Resolution Data All Runs.

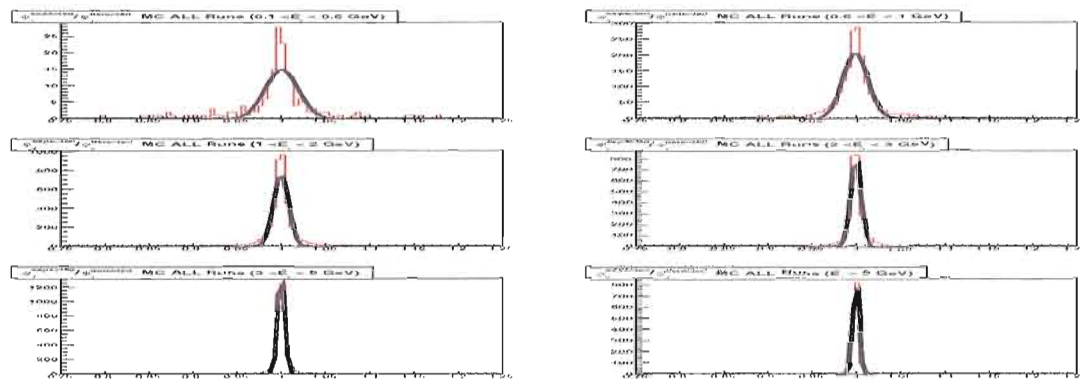


Fig. A.10: Phi Resolution MC All Runs.

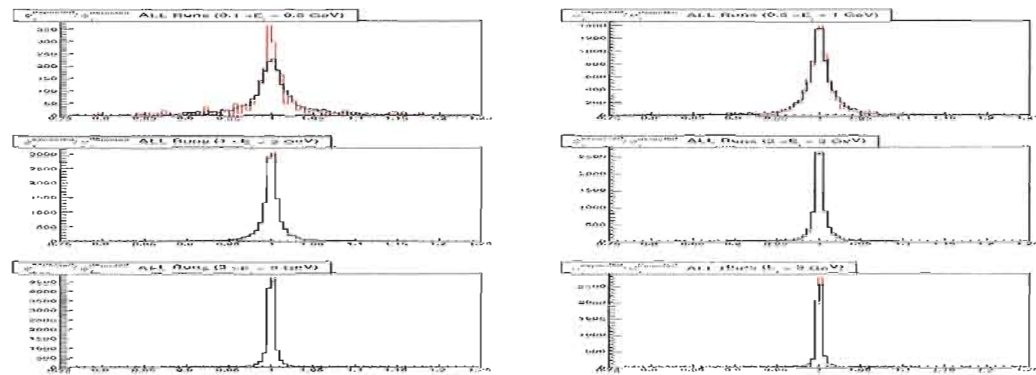


Fig. A.11:  $\Phi(\phi)$  Resolution Data(black line) and MC(red line) All Runs.

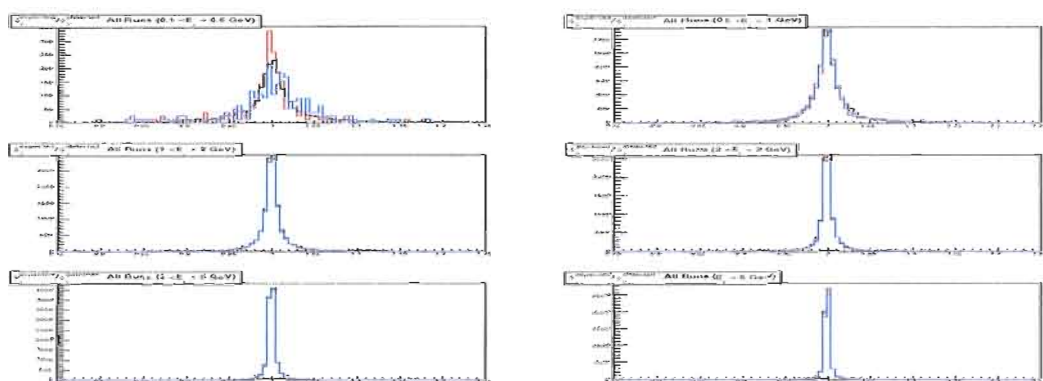


Fig. A.12: After  $\phi$  smearing: MC after smearing(blue line), initial MC(red line) and Data(black line) All Runs.

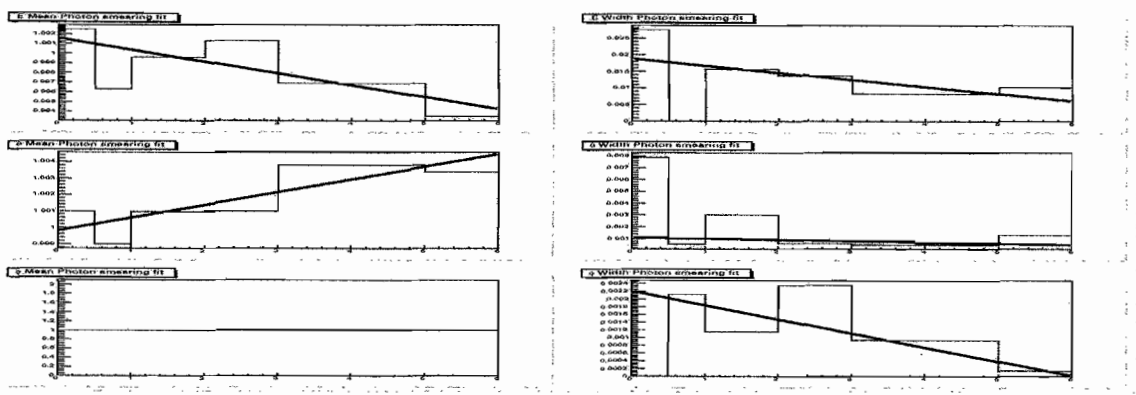


Fig. A.13: Linear fit ( $y = a + bx$ ) to scale and resolution (smearing) parameters.

	Data			
	Mean	Sigma	$\alpha$	n
$0.1 < E_\gamma < 0.5$ GeV	$1.01901 \pm 0.002604$	$0.054155 \pm 0.00179$	$-0.5637 \pm 0.04000$	$111.685 \pm 53.388$
$0.5 < E_\gamma < 1.0$ GeV	$1.01263 \pm 0.000472$	$0.047603 \pm 0.00006$	$-0.9775 \pm 0.03674$	$5.984 \pm 1.415$
$1.0 < E_\gamma < 2.0$ GeV	$1.01044 \pm 0.000204$	$0.030754 \pm 0.00016$	$-1.0711 \pm 0.01874$	$4.229 \pm 0.246$
$2.0 < E_\gamma < 3.0$ GeV	$1.00823 \pm 0.000178$	$0.022178 \pm 0.00013$	$-0.9999 \pm 0.01942$	$3.856 \pm 0.173$
$3.0 < E_\gamma < 5.0$ GeV	$1.00560 \pm 0.000080$	$0.016001 \pm 0.00000$	$-0.8680 \pm 0.00921$	$3.332 \pm 0.076$
$E_\gamma > 5.0$ GeV	$1.00216 \pm 0.000079$	$0.015556 \pm 0.00000$	$-0.8867 \pm 0.00829$	$3.454 \pm 0.075$

Tab. A.1: Energy Resolution Data Run 1-5

	MC			
	Mean	Sigma	$\alpha$	n
$0.1 < E_\gamma < 0.5 \text{ GeV}$	$1.01647 \pm 0.01062$	$0.046618 \pm 0.00778$	$-0.8738 \pm 0.35555$	$129.010 \pm 65.088$
$0.5 < E_\gamma < 1.0 \text{ GeV}$	$1.01635 \pm 0.00138$	$0.047603 \pm 0.00102$	$-1.0240 \pm 0.11152$	$11.676 \pm 10.969$
$1.0 < E_\gamma < 2.0 \text{ GeV}$	$1.01083 \pm 0.00036$	$0.026466 \pm 0.00027$	$-0.8529 \pm 0.02672$	$7.176 \pm 0.989$
$2.0 < E_\gamma < 3.0 \text{ GeV}$	$1.00694 \pm 0.00031$	$0.017367 \pm 0.00022$	$-0.7369 \pm 0.02389$	$5.203 \pm 0.412$
$3.0 < E_\gamma < 5.0 \text{ GeV}$	$1.00087 \pm 0.00014$	$0.013653 \pm 0.00010$	$-0.6567 \pm 0.01123$	$3.736 \pm 0.132$
$E_\gamma > 5.0 \text{ GeV}$	$1.00088 \pm 0.00020$	$0.011618 \pm 0.00013$	$-0.5497 \pm 0.01386$	$4.295 \pm 0.179$

Tab. A.2: Energy Resolution Run MC 1-5

	MC			
	Mean	Sigma	$\alpha$	n
$0.1 < E_\gamma < 0.5$ GeV	$1.01940 \pm 0.005701$	$0.0557008 \pm 0.000844$	$-0.887176 \pm 0.287465$	$104.9965 \pm 60.256$
$0.5 < E_\gamma < 1.0$ GeV	$1.01255 \pm 0.000984$	$0.0476891 \pm 0.000485$	$-1.000432 \pm 0.090988$	$5.3746 \pm 4.826$
$1.0 < E_\gamma < 2.0$ GeV	$1.01046 \pm 0.000389$	$0.0309906 \pm 0.000289$	$-0.970635 \pm 0.036589$	$5.6045 \pm 0.747$
$2.0 < E_\gamma < 3.0$ GeV	$1.00827 \pm 0.000258$	$0.0221550 \pm 0.000191$	$-0.920639 \pm 0.029759$	$4.3695 \pm 0.296$
$3.0 < E_\gamma < 5.0$ GeV	$1.00453 \pm 0.000150$	$0.0158453 \pm 0.000109$	$-0.886355 \pm 0.017002$	$3.6162 \pm 0.122$
$E_\gamma > 5.0$ GeV	$1.00147 \pm 0.000148$	$0.0149698 \pm 0.000103$	$-0.820265 \pm 0.014780$	$3.8359 \pm 0.152$

Tab. A.3: Energy Resolution Run MC 1-5 After Smearing

	<b>Mean Ratio</b>	$\sigma_{smearing}$
	$\frac{MeanData}{MeanMC}$	$\sqrt{\sigma_{Data}^2 - \sigma_{MC}^2}$
$0.1 < E_\gamma < 0.5$ GeV	1.0025	0.02756
$0.5 < E_\gamma < 1.0$ GeV	0.9963	0.0
$1.0 < E_\gamma < 2.0$ GeV	0.9996	0.01566
$2.0 < E_\gamma < 3.0$ GeV	1.0013	0.01379
$3.0 < E_\gamma < 5.0$ GeV	0.9969	0.00834
$E_\gamma > 5.0$ GeV	0.9935	0.01034

Tab. A.4: Energy Smearing

	Data		MC	
	Mean	Sigma	Mean	Sigma
$0.1 < E_\gamma < 0.5 \text{ GeV}$	$1.016 \pm 0.001$	$0.02404 \pm 0.00057$	$1.015 \pm 0.001$	$0.02271 \pm 0.00065$
$0.5 < E_\gamma < 1.0 \text{ GeV}$	$1.010 \pm 0.000$	$0.01761 \pm 0.00017$	$1.011 \pm 0.000$	$0.01682 \pm 0.00018$
$1.0 < E_\gamma < 2.0 \text{ GeV}$	$1.005 \pm 0.000$	$0.01160 \pm 0.00010$	$1.004 \pm 0.000$	$0.0112 \pm 0.00010$
$2.0 < E_\gamma < 3.0 \text{ GeV}$	$1.003 \pm 0.000$	$0.00827 \pm 0.00009$	$1.002 \pm 0.000$	$0.008248 \pm 0.00008$
$3.0 < E_\gamma < 5.0 \text{ GeV}$	$1.002 \pm 0.000$	$0.00661 \pm 0.00005$	$0.9982 \pm 0.0001$	$0.006588 \pm 0.000052$
$E_\gamma > 5.0 \text{ GeV}$	$1.000 \pm 0.000$	$0.00688 \pm 0.00007$	$0.9966 \pm 0.0001$	$0.006752 \pm 0.000068$

Tab. A.5: Theta( $\theta$ ) Resolution Run 1-5

	<b>Mean Ratio</b> $\pm$	$\sigma_{smearing}$
	$\frac{MeanData}{MeanMC} \pm$	$\sqrt{\sigma_{Data}^2 - \sigma_{MC}^2}$
$0.1 < E_\gamma < 0.5$ GeV	$1.00099 \pm$	0.007885
$0.5 < E_\gamma < 1.0$ GeV	$0.99901 \pm$	0.000521
$1.0 < E_\gamma < 2.0$ GeV	$1.00096 \pm$	0.003020
$2.0 < E_\gamma < 3.0$ GeV	$1.00099 \pm$	0.000589
$3.0 < E_\gamma < 5.0$ GeV	$1.00381 \pm$	0.000514
$E_\gamma > 5.0$ GeV	$1.00341 \pm$	0.001316

Tab. A.6: Theta( $\theta$ ) Smearing

	<b>Mean Ratio</b>	$\sigma_{smearing}$
$0.1 < E_\gamma < 0.5$ GeV	$1.016 \pm 0.0$	$0.02414 \pm 0.00057$
$0.5 < E_\gamma < 1.0$ GeV	$1.010 \pm 0.0$	$0.01742 \pm 0.00017$
$1.0 < E_\gamma < 2.0$ GeV	$1.005 \pm 0.0$	$0.01162 \pm 0.00010$
$2.0 < E_\gamma < 3.0$ GeV	$1.003 \pm 0.0$	$0.00837 \pm 0.000086$
$3.0 < E_\gamma < 5.0$ GeV	$1.002 \pm 0.0$	$0.00661 \pm 0.000053$
$E_\gamma > 5.0$ GeV	$1.00 \pm 0.0$	$0.00689 \pm 0.000074$

Tab. A.7: Theta( $\theta$ ) After Smearing

	Data		MC	
	Mean	Sigma	Mean	Sigma
$0.1 < E_\gamma < 0.5 \text{ GeV}$	$1.001 \pm 0.001$	$0.019 \pm 0.001$	$1.001 \pm 0.0$	$0.01898 \pm 0.00141$
$0.5 < E_\gamma < 1.0 \text{ GeV}$	$1.000 \pm 0.0$	$0.01514 \pm 0.00024$	$1.000 \pm 0.0$	$0.01499 \pm 0.00023$
$1.0 < E_\gamma < 2.0 \text{ GeV}$	$1.000 \pm 0.0$	$0.008395 \pm 0.000123$	$1.000 \pm 0.0$	$0.008315 \pm 0.000134$
$2.0 < E_\gamma < 3.0 \text{ GeV}$	$1.000 \pm 0.0$	$0.005991 \pm 0.000104$	$1.000 \pm 0.0$	$0.005505 \pm 0.000085$
$3.0 < E_\gamma < 5.0 \text{ GeV}$	$1.000 \pm 0.0$	$0.003407 \pm 0.000048$	$1.000 \pm 0.0$	$0.003275 \pm 0.000042$
$E_\gamma > 5.0 \text{ GeV}$	$1.000 \pm 0.0$	$0.002493 \pm 0.000045$	$1.000 \pm 0.0$	$0.002581 \pm 0.000041$

Tab. A.8:  $\Phi(\phi)$  Resolution Run 1-5

	<b>Mean Ratio</b>	$\sigma_{smearing}$
	$\frac{MeanData}{MeanMC}$	$\sqrt{\sigma_{Data}^2 - \sigma_{MC}^2}$
$0.1 < E_\gamma < 0.5$ GeV	1.	0.0000
$0.5 < E_\gamma < 1.0$ GeV	1.	0.002126
$1.0 < E_\gamma < 2.0$ GeV	1.	0.001156
$2.0 < E_\gamma < 3.0$ GeV	1.	0.002363
$3.0 < E_\gamma < 5.0$ GeV	1.	0.000939
$E_\gamma > 5.0$ GeV	1.	0.000141

Tab. A.9:  $\Phi(\phi)$  Smearing

	<b>Mean Ratio</b>	$\sigma_{smearing}$
$0.1 < E_\gamma < 0.5$ GeV	$1.000 \pm 0.0$	$0.0191 \pm 0.000647$
$0.5 < E_\gamma < 1.0$ GeV	$1.000 \pm 0.0$	$0.01504 \pm 0.000180$
$1.0 < E_\gamma < 2.0$ GeV	$1.000 \pm 0.0$	$0.00840 \pm 0.000132$
$2.0 < E_\gamma < 3.0$ GeV	$1.000 \pm 0.0$	$0.00598 \pm 0.000084$
$3.0 < E_\gamma < 5.0$ GeV	$1.000 \pm 0.0$	$0.00336 \pm 0.000042$
$E_\gamma > 5.0$ GeV	$1.000 \pm 0.0$	$0.00251 \pm 0.000040$

Tab. A.10:  $\Phi(\theta)$  After Smearing

$\gamma$	<b>a</b>	<b>b</b>
E Mean	$1.001583 \pm 0.005786$	$-0.001218 \pm 0.000167$
E Width	$0.018874 \pm 0.000850$	$-0.002125 \pm 0.000218$
$\theta$ Mean	$0.999819 \pm 0.057911$	$0.000781 \pm 0.000016$
$\theta$ Width	$0.001116 \pm 0.000200$	$-0.000103 \pm 0.000055$
$\phi$ Mean	$1.000 \pm 0.0$	$0.00 \pm 0.00$
$\phi$ Width	$0.002204 \pm 0.000235$	$-0.000363 \pm 0.000048$

Tab. A.11: Fit to photon scale and resolution parameters

## APPENDIX B

### GTVL

Parameter	Value
Minimum Transverse Momentum	0.1 GeV/c
Maximum Monemtum	10 GeV/c
Maximum distance of closest approach in $x - y$ plane	1.5 cm
Minimum distance of closest approach in z	-10 cm
Maximum distance of closest approach in z	10 cm
Minimum number of DCH hits	20

Tab. B.1: Good Track Candidate

## REFERENCES

- [1] M. L. Perl et al. Phys. Rev. Lett. **35** (1975) 1489.
- [2] S. Eidelman et al (Particle Data Group), Phys. Lett. B 592 1(2004).
- [3] Y. S. Tsai, Phys. Rev. D 4, 2821; 13, 1771(E) (1976).
- [4] R. Barate et al., (ALEPH Collaboration), Z. Phys. C76 (1997) 15.
- [5] S. Anderson et al. (CLEO Collaboration), Phys. Rev. D **61**, 112002 (2000).
- [6] Sven Menke et. al. (OPAL Collaboration), Eur. Phys. J. **C7**, 571.
- [7] M. Davier, A. Hocker, and Z. Zhang [arXiv:hep-ph/0507078v1].
- [8] CMD-2 Collaboration (R.R. Akhmetdin, *et. al.*, 2004, Phys. Lett. **B578**, 285.
- [9] DM1 Collaboration (A. Quenzer, *et. al.*, 1978, Phys. Lett. **B76**, 512.
- [10] DM1 Collaboration (D. Bisello, *et. al.*, 1989, Phys. Lett. **B220**, 321.
- [11] OLYA Collaboration (I.B. Vasserman, *et. al.*), 1979, Sov. J. Nucl. Phys. **30**, 519.
- [12] OLYA&CMD Collaboration (L.M. Barkov, *et. al.*), 1985, Nucl. Phys. **B256**, 365.
- [13] TOF Collaboration (I.B. Vasserman, *et. al.*), 1981, Sov. J. Nucl. Phys. **33**, 709.
- [14] Dirac, P.A.M., 1928, Proc. Roy. Soc. **A117**, 610.

- [15] Schwinger, J., 1948, Phys. Rev. **73**, 416.
- [16] Nagle, J., R. Julian, and J. Zacharias, 1947, Phys. Rev. **72**, 971.
- [17] Nagle, J., E. Nelson, and I. Rabi, 1947, Phys. Rev. **71**, 345.
- [18] Gabrielse, G., and J. Tan, 1994, “Cavity Quantum Electrodynamics”, Ed. P. Berman, Academic Press, San Diego, 267.
- [19] Van Dyck, R.S., P.B. Schwinberg, and H.G. Dehmelt, 1987, Phys. Rev. Lett. **59**, 26.
- [20] Czarnecki, A., and W. Marciano, 2001, Phys. Rev. **D64**, 013014.
- [21] R.M. Carey et al. (Muon (g-2) Collaboration), Phys. Rev. Lett. 82 (1999) 1632.
- [22] H.N. Brown et al. (Muon (g-2) Collaboration), Phys. Rev. D62, (2000) 091101.
- [23] H.N. Brown et al. (Muon (g-2) Collaboration), Phys. Rev. Lett. 86, (2001) 2227.
- [24] G. W. Bennett et al. (Muon (g-2) Collaboration), hep-exp/0208001 (Aug. 2002).
- [25] J. Bailey et al., Phys. Lett. B68 (1977) 191. F.J.M. Farley and E. Picasso, “The muon (g - 2) Experiment”, Advanced Series on Directions in High Energy Physics - Vol. 7 Quantum Electrodynamics, ed. T. Kinoshita, World Scientific 1990.
- [26] Czarnecki, A., and W.J. Marciano, 1999, Nucl. Phys. (Proc. Suppl.) **B76**, 245.
- [27] Hughes, V.W., and T. Kinoshita, 1999, Rev. Mod. Phys. **71**, S133.
- [28] Brodsky, S.J., and S. Menke, C. Merino, and J. Rathsman, 2002, Phys. Rev. **D67**, 055008.
- [29] M.N. Achasov *et. al.*(SND Collaboration), 2005, [hep-ex/0506076].
- [30] J. H. Kuhn and A. Santa Maria, Z. Phys. C 48, 445 (1990).
- [31] G. Gounaris and J. J. Sakurai, Phys. Rev. Lett. 21, 244 (1968).

- [32] F. James et al., MINUIT, CERN DD/D506, 1987.
- [33] W. Verkerke and D. Kirkby, arXiv:physics/0306116  
see also <http://roofit.sourceforge.net>.
- [34] Andreas Hoecker, Presentation in Moriond 2008.
- [35] K. Hagiwara, A.D. Martin, D. Nomura and T. Teubner, Phys. Lett. B. 649 (2007) 173.
- [36] M. Hayakawa, T. Kinoshita and A.I. Sanda, Phys. Rev. D54 (1996) 3137; M. Hayakawa, T. Kinoshita and A.I. Sanda, Phys. Rev. Lett. 75 (1995) 790.
- [37] J. Bijnens, E. Pallante and J. Prades, Nucl. Phys. B474 (1996) 379.
- [38] M. Knecht et al., Phys.Rev. D65 (2002) 073034.
- [39] M. Hayakawa and T. Kinoshita, hep-ph/0112102.
- [40] J. Bijnens, E. Pallante and J. Prades, Nucl.Phys. B626 (2002) 410.
- [41] C. Bouchiat and L. Michel, J. Phys. Radium 22 (1961) 121.
- [42] N. Cabibbo and R. Gatto, Phys. Rev. Lett. 4 (1960) 313; Phys. Rev. 124 (1961) 1577; L.M. Brown and F. Calogero, Phys. Rev. 120 (1960) 653.
- [43] S. Eidelman and F. Jegerlehner, Z. Phys. C67 (1995) 585.
- [44] R. Alemany, M. Davier and A. Hocker, Eur.Phys.J. C2 (1998) 123.
- [45] M. Davier and A. Hocker, 1998, Phys. Lett. **B435**, 427.
- [46] A. Aloisio *et. al.* (KLOE Collaboration), 2005, Phys. Lett. **B606**, 12.
- [47] ALEPH Collaboration(S. Schael, *et. al.*, 2005, Phys. Rept. **421**, 191.

- [48] Ghozzi, S., and F. Jegerlehner, 2004, Phys. Lett. **B**583, 222.
- [49] Bijnens, J., and P. Gosdzinsky, 1996, Phys. Lett. **B**388, 203.
- [50] D.E. Groom et al., Review of Particle Physics, Eur.Phys.J. C15, 1 (2000).
- [51] R.L. Garwin, L.M. Lederman and M. Weinrich, Phys. Rev. 105, 1415 (1957).
- [52] G. Charpak, F.J.M. Farley, R.L. Garwin, T. Muller, J.C. Sens and A. Zichichi, Nuovo Cimento 37, 1241 (1965).
- [53] For a general review of all three CERN experiments, see F.J.M. Farley and E. Picasso, in Quantum Electrodynamics, T. Kinoshita ed., (World Scientific, 1990).
- [54] J. Bailey, K. Borer, F. Combley, H. Drumm, C. Eck, F.J.M. Farley, J.H. Field, W. Flegel, P.M. Hattersley, F. Krienen, F. Lange, G. Lebe, E. McMillan, G. Petrucci, E. Picasso, O. Rnoffsson, W. von Rden, R.W. Williams and S. Wojcicki, Nucl. Phys. B150, 1 (1979)
- [55] A. Czarnecki and W.J. Marciano, Nucl. Phys. (Proc. Suppl.) B76, 245 (1999); Phys. Rev. D64 (2001).
- [56] S. Weinberg, The Quantum Theory of Fields, Vol 3, Cambridge University Press (1999); John R. Gribbin, The Search for Superstrings, Symmetry and the Theory of Everything, Little Brown & Co (2000)
- [57] G.C. Fox and S. Wolfram, Nucl. Phys. B149 (1979) 413.
- [58] S. Banarjee et al., BAD 760, “CM2 skims for  $e^+e^- \rightarrow \mu^+\mu^-$  and  $e^+e^- \rightarrow \tau^+\tau^-$  events (TAUQED2)” (2003).
- [59] S. Jadach, Comp. Phys. Comm. 130 (2000) 260.
- [60] S. Jadach and Z. Was, Comp. Phys. Comm. 85 (1995) 453.
- [61] Z. Was, Nucl. Phys. Proc. Suppl. 98 (2001) 96 [arXiv:hep-ph/0011305]
- [62] E. Berberio and Z. Was, Comp. Phys. Comm. 79 (1994) 291.
- [63] <http://www.slac.stanford.edu/BFROOT/www/doc/workbook/eventinfo/BtaCandInfo/CandLists.html>.

- [64] Olga Igonkina, BAD 722. "A Search for LFV Decays  $\tau \rightarrow lll$  ".
- [65] Olga Igonkina, BAD 938, " A Search for LFV Decays  $\tau \rightarrow lhh$  ".
- [66] Glen Cowan, "Statistical Data Analysis"
- [67] A. Hocker and V. Kartvelishvili, Nucl. Inst. Meth. A372, 469 (1996).
- [68] V. Blobel, "Unfolding Methods in high-energy physics experiments", DESY 84-118 (1984).
- [69] BABAR Collaboration, B. Aubert et. al., Study of  $B \rightarrow ul\bar{\nu}$  decays on the recoil of fully reconstructed b mesons and determination of  $|V_{ub}|$ , hep-ex/0408068.
- [70] <http://babar-hn.slac.stanford.edu:5090/cgi-bin/internal/cvsweb.cgi/RooUnfHistoSvd/>
- [71] G.E. Forsythe, M. A. Malcolm and C.B. Moller, Computer Methods for Mathematical Computations(Prentice-Hall, Englewood Cliffs, 1977).
- [72] C.E. Lawson and R.J. Hanson, Solving Least Square Problems (Prentice-Hall, Englewood Cliffs, 1974).
- [73] BAD 867 Tracking Efficiency for BABAR data sample
- [74] Mark Tiller Allen, M. T. Naisbit, Aaron Rodman, BAD 870, " $\pi^0$  Efficiency."
- [75] Michael Roney, Zinkoo Yun, BAD 1033.
- [76] David Payne, BAD 1110, "Photon Efficiency using  $\mu\mu\gamma$ ."
- [77] Aaron Rodman, *et.al.*, BAD 1639, "Smearing of MonteCarlo calorimeter simulation"
- [78] M. Roney et al., BAD 455, "Search for the Lepton Number Violating Decay  $\tau \rightarrow \mu\gamma$  "(2002);  
BABAR Collaboration, eConf. C0209101 (2002) TU12 [hep-ex/0212009].
- [79] Braaten, E., and C.S. Li, 1990, Phys. Rev. D42, 3888.

- [80] Marciano, W. and A. sirlin, 1998, Phys. Rev. Lett. **61**, 1815.
- [81] Decker, R., and M. Finkemeier, 1993, Phys. Rev. **D48**, 4203.
- [82] V.Cirigliano, G.Ecker and H.Neufeld, Phys. Lett. B 513, 361(2001);  
V.Cirigliano, G.Ecker and H.Neufeld, J. High Energy Phys, JHEP 08, 002(2002).
- [83] M.Davier, S.Eidelman, A. Hocker, and Z.Zhang, Eur. Phys. J. C 27, 497 (2003).
- [84] Czyz, H., and J.H. Kuhn, 2001, Eur. Phys. J. **C18**, 49